Title

Advanced Magnetic Resonance Vascular Imaging: Technical Development and Application

Author

Hu, Zhehao

Publication Date

2022

Peer reviewed|Thesis/dissertation

UNIVERSITY OF CALIFORNIA

Los Angeles

Advanced Magnetic Resonance Vascular Imaging:

Technical Development and Application

A dissertation submitted in partial satisfaction

of the requirements for the degree Doctor of Philosophy

in Bioengineering

by

Zhehao Hu

2022

ABSTRACT OF THE DISSERTATION

Advanced Magnetic Resonance Vascular Imaging:

Technical Development and Application

by

Zhehao Hu

Doctor of Philosophy in Bioengineering

University of California, Los Angeles, 2022

Professor Zhaoyang Fan, Co-Chair

Professor Debiao Li, Co-Chair

Vascular imaging plays a crucial role in the assessment of a variety of vascular diseases. In the past few decades, efforts have been made to establish various imaging modalities for the evaluation of vasculatures. For example, CT, PET, ultrasound, and MR, have all been shown to have the capability to visualize or quantify different vasculatures. MR vascular imaging, compared to other imaging modalities, has several unique advantages, and has evolved as an ever-attractive choice both in research and clinical studies.

Based on the scale of the target vasculature, MR vascular imaging can be further classified into two subcategories: MR macrovascular imaging and MR microvascular imaging. Macrovascular imaging is developed to assess diseases of, for example, the aorta, the coronary, the sizable arteries in the brain, and etc. Classically, macrovascular imaging can be categorized into bright-blood and dark-blood techniques. As a bright-blood technique, MR angiography has evolved as an important tool in the evaluation of macro vessels. Well dark-blood imaging, also called vessel wall imaging, has shown great potentials because of its ability to directly visualize pathological changes within the vessel wall. In contrast, MR microvascular imaging concentrates upon “micro” blood vessels, including small arteries, arterioles, and capillaries, with some biomarkers quantified to assess vessel changes at the microscopic level. Permeability and perfusion are two widely adopted biomarkers in this scenario that can be generated by dynamic contrast-enhanced MR, which is DCE-MR and dynamic susceptibility contrast-enhanced MR, which is DSC-MR, respectively. In recent years, with the advancements in imaging technologies, both MR macrovascular imaging and microvascular imaging have been applied to real clinical workflows to help with diagnosis and prognosis. For example, MR macrovascular imaging, especially MRA, is nearly always adopted as an adjunct in stroke diagnosis and etiology evaluation, while MR microvascular imaging has been shown to provide insights into many different aspects of brain tumors, like surgical planning and treatment response assessment. However, the vascular imaging techniques adopted in current paradigm for both applications are suboptimal and have several limitations.

The primary goal of the work in the dissertation is to address the limitations by developing advanced MR macroscopic and microscopic vascular imaging techniques that can assist in stroke diagnosis and etiology evaluation and brain cancer evaluation, respectively. Specifically, for stroke etiology evaluation, a comprehensive two-station stroke etiology evaluation technique covering both the head-neck vasculature and the heart was developed. Our goal is to develop a technique that can be easily incorporated into clinical workup, and hopefully improves the diagnostics and patient outcomes. The technical development was divided into two specific aims, where Aim 1 is to develop a novel motion-compensated, data-driven accelerated 3D MR vessel wall imaging for the evaluation of the head-neck vessels, and Aim 2 is to develop a novel ECG- and navigator-free multi-dimensional assessment of cardiovascular system technique for the evaluation of the thoracic aorta and the cardiac structures. As for brain cancer evaluation, we developed a novel dynamic imaging for cerebrovascular evaluation technique based on MR multitasking framework for simultaneous 3D permeability and leakage-insensitive perfusion quantification based on single-dose of contrast injection. Feasibility of each developed technique is evaluated on both healthy subjects and patients.

The dissertation of Zhehao Hu is approved.

Anthony G. Christodoulou

David S. Liebeskind

Holden H. Wu

Debiao Li, Committee Co-Chair

Zhaoyang Fan, Committee Co-Chair

University of California, Los Angeles

2022

Dedicated to the ones I love:

My parents: Lingxia Zhang & Xuebin Hu

My girlfriend: Qiaoyi Wu

TABLE OF CONTENTS

LIST OF ACRONYMS

Physics

T — Tesla

m — meter

mm — millimeter

s — second

ms — millisecond

min — minute

Hz — hertz

CT — computerized tomography

Statistics

CI — confidence interval

ICC — intra-class correlation coefficient

P — statistical significance coefficient

R — regression coefficient

Mathematics

CC — cross correlation

FT — Fourier transform

SVD — singular value decomposition

LRT — low-rank tensor

Medicine

BB — bright-blood

BBB — blood-brain barrier

CA — contrast agent

CCS — causative classification of stroke

CR — contrast ratio

CT — computed tomography

DB — dark-blood

ECG — echocardiography

GB — gray-blood

GM — gray matter

ICA — internal carotid artery

LA — left atria

LV — left ventricle

LVEF — left ventricular ejection fraction

MCA — middle cerebral artery

RA — right atria

RV — right ventricle

TEE — transesophageal echocardiography

TTE — transthoracic echocardiography

VA — vertebral artery

WA — wall area

WM — white matter

Magnetic Resonance Imaging

2D/3D — two-dimension/three-dimension

AF — acceleration factor

AIF — arterial input function

CBV — cerebral blood volume

CBF — cerebral blood flow

CNR — contrast-to-noise ratio

CS — compressed sensing

DCE-MR — dynamic contrast-enhanced MR

DSC-MR — dynamic susceptibility contrast-enhanced MR

EPI — echo planar imaging

FLASH — fast low angle shot

FOV — field-of-view

IR-SE — inversion-recovery spin-echo

IR-TSE — inversion-recovery turbo spin-echo

K^{trans} — transfer constant

ME-GRE — multi-echo gradient-echo

MR — magnetic resonance

PI — parallel imaging

RF — radiofrequency

ROI — region-of-interests

SG — self-gating

SNR — signal-to-noise ratio

SR — saturation recovery

SSFP — steady-state free precession

T2-IR — T2-prepared inversion recovery

TE — echo time

TR — repetition time

TSE — turbo spin-echo

v_e — fractional extravascular-extracellular volume

vNav — volumetric navigator

v_p — fractional plasma volume

VWI — vessel wall imaging

Deep learning

CNN — convolutional neural network

Conv 3 × 3 — convolution with 3 × 3 kernel

DC — data consistency

iMR — iterative multi-scale refinement

MAE — mean absolute error

PSNR — peak signal-to-noise ratio

ReLU — rectified linear unit

SSIM — structural similarity index

Techniques

CAMWARE — cascaded multi-scale wavelet with iterative refinement network

GRAPPA — generalized autocalibrating partial parallel acquisition

MT-DICE — MR multitasking-based dynamic imaging for cerebrovascular evaluation

MT-MACS — MR multitasking-based multidimensional assessment of cardiovascular system

SPACE — sampling perfection with application-optimized contrasts using different flip angle evolution

LIST OF FIGURES

LIST OF TABLES

ACKNOWLEDGEMENT

Foremost, I would like to extend my deepest gratitude to my advisor Dr. Zhaoyang Fan. It is truly lucky for me to join his research lab and have his continuous guidance and support throughout my PhD career. He has provided me with endless research resources including sufficient MR scanner access and insightful instructions on my work. His patience, motivation, enthusiasm, and immense knowledge truly help me a lot in all the time of research and writing of this thesis. I could not have imagined having a better advisor and mentor for my PhD study.

I would like to express my appreciation to Dr. Debiao Li, Dr. Anthony Christodoulou and Dr. Yibin Xie. During my first few years at Biomedical Imaging Research Institute, Cedars-Sinai Medical Center, they have provided me with big picture of the field of medical imaging and detailed instructions on my research work.

In addition, I would like to thank the rest of my doctoral committee, Dr. Holden Wu, Dr. David Liebeskind, and previous committee member, Dr. Peng Hu. They have guided me starting my PhD qualifying exam, offering encouragement and constructive advice. Their technical and clinical expertise and generous personality have a great influence on me as well as my research work.

Special thanks to Dr. Xiaoming Bi, and Dr. Fei Han, who are our onsite Siemens scientists. They have guided me step into the process of sequence programming and offered me with numerous help during my practice. I truly appreciate their generous sharing of their knowledge and experience in sequence development.

I would like to specially thank my fellow graduate students and dearest friends at Biomedical Imaging Research Institute, Cedars-Sinai Medical Center: Dr. Jaime Shaw,

Dr. Zixin Deng, Dr. Zhengwei Zhou, Dr. Hsu-Lei Lee, Dr. Xianglun Mao, Dr. Sen Ma, Dr. Nan Wang. Dr. Xingmin Guan, Dr. Yuhua Chen, Dr. Eric Johnson, Pei Han, Xinheng Zhang, Tianle Cao, Chaowei Wu, Shihan Qiu, and Zihao Chen, and at Keck School of Medicine: Dr. Daeun Kim, Dr. Jiayu Xiao, Junzhou Chen, Yang Chen, Siddarth Ganesh, and Dharanya Vanchinathan. Their conversation and collaboration made for a wonderful environment.

Finally, I would like to thank my parents: Lingxia Zhang and Xuebin Hu, who have been unconditionally loving me and supporting me throughout my life, and my girlfriend: Qiaoyi Wu, the half of me who has made me whole.

VITA

Education:

- **M.S.**, Department of Bioengineering, University of California, Los Angeles (2018)
- **B.S.**, Department of Optical Science, Zhejiang University, China (2017)

Journal Publications:

- **Hu Z**, Christodoulou AG, Wang N, Shaw JL, Song SS, Maya MM, Ishimori ML, Forbess LJ, Xiao J, Bi X, Han F, Li D, Fan Z. Magnetic resonance multitasking for multidimensional assessment of cardiovascular system: development and feasibility study on the thoracic aorta. *Magnetic Resonance in Medicine* 2020; 84.5:2376-2388.
- **Hu Z**, van der Kouwe A, Han F, Xiao J, Chen J, Han H, Bi X, Li D, Fan Z. Motion-compensated 3D turbo spin-echo for more robust MR intracranial vessel wall imaging. *Magnetic Resonance in Medicine* 2021; 86.2:637-647.
- **Hu Z**, Xiao J, Lerner A, Kim PE, Poblete RA, Fan Z. CAMWARE: CAscaded Multi-scale WAvelet with iterative Refinement reconstruction neural network for accelerated 3D intracranial MR vessel wall imaging. *American Journal of Neuroradiology*; under review.
- **Hu Z**, Christodoulou AG, Wang N, Xie Y, Maya MM, Shiroishi MS, Yang W, Zada G, Chang EL, Li D, Fan Z. MR multitasking-based dynamic imaging for cerebrovascular evaluation (MT-DICE): simultaneous quantification of permeability and leakage-insensitive perfusion by dynamic T1/T2* mapping. *Magnetic Resonance in Medicine*; under review.
- **Hu Z**, Xiao J, Mao X, Xie Y, Kwan AC, Song SS, Wilcox AG, Li D, Christodoulou AG, Fan Z. MR Multitasking based Multi-dimensional Assessment of Cardiovascular System (MT-MACS) with Extended Spatial Coverage and Water-Fat Separation. In preparation.
- Mao X, Lee HL, **Hu Z**, Cao T, Han F, Ma S, Serry FM, Fan Z, Xie Y, Li D, Christodoulou AG. Simultaneous multi-slice cardiac MR multitasking for motion-resolved, non-ECG, free-breathing T1-T2 mapping. *Frontiers in Cardiovascular Imaging*; 267.
- Chang P, Xiao J, **Hu Z**, Kwan AC, Fan Z. Imaging of left chamber intracardiac thrombus: clinical needs, current diagnostic imaging modalities, and emerging cardiac magnetic resonance techniques. *Therapeutic Advances in Cardiovascular Disease*; under review.

- Han P, Chen J, Xiao J, Han F, **Hu Z**, Yang W, Ling DC, Li D, Christodoulou AG, Fan Z. Single projection driven real-time (SPIDER) multi-contrast MR imaging using a pre-learned spatial subspace. *Physics in Medicine and Biology*; under review.

Selected Conference Presentations

- **Early-Career Awards oral presentation** at 23rd Annual Meeting of SCMR (2020) for the abstract:

  Hu Z, Christodoulou A, Wang N, Song S, Maya M, Ishimori M, Forbess L, Xiao J, Bi X, Han F, Li D, Fan Z. Development of an MR multitasking-based multi-dimensional assessment of cardiovascular system technique: feasibility on the thoracic aorta.

- **Oral presentations** at 28th Annual Meeting of ISMRM (2020) for the abstracts:

  Hu Z, Han F, Van Der Kouwe A, Bi X, Sun B, Xiao J, Chen J, Song S, Maya M, Li D, Fan Z. Motioncompensated 3D TSE for more robust intracranial MR vessel wall imaging.

  Hu Z, Christodoulou A, Wang N, Song S, Maya M, Ishimori M, Forbess L, Xiao J, Bi X, Han F, Li D, Fan Z. MR multitasking-based multi-dimensional assessment of cardiovascular system (MT-MACS): feasibility on the thoracic aorta.

- **Oral presentation** at 29th Annual Meeting of ISMRM (2021) for the abstracts:

  Hu Z, Christodoulou A, Wang N, Xie Y, Li D, Fan Z. MR Multitasking-based dynamic imaging for cerebrovascular evaluation (MT-DICE): further development and feasibility study on brain cancer.

  Hu Z, Xiao J, Mao X, Xie Y, Kwan A, Song S, Wilcox A, Li D, Christodoulou A, Fan Z. MR multitasking-based multi-dimensional assessment of cardiovascular system (MT-MACS) with extended spatial coverage and water-fat separation.

- **Early-Career Investigator Symposium oral presentation** at 64th Annual Meeting of AAPM (2021) for the abstract:

  Hu Z, Christodoulou A, Wang N, Xie Y, Maya M, Shiroishi M, Yang W, Li D, Fan Z. MR multitasking-based dynamic imaging for cerebrovascular evaluation (MT-DICE): development and feasibility study on brain cancer.

- **Oral presentations** at 30th Annual Meeting of ISMRM (2022) for the abstract:

  Hu Z, Lerner A, Poblete RA, Fan Z. CAMWARE: cascaded multi-level wavelet refine neural network for accelerated whole-brain MR vessel wall imaging.

CHAPTER 1

Introduction

1.1 MR VASCULAR IMAGING

Vascular imaging encompasses a wide variety of pathology and plays a critical role in the assessment of varied manifestations of vascular disease[1]. In the past decade, efforts have been made to establish various methodologies for the evaluation of vasculature, including magnetic resonance (MR) imaging, computed tomography (CT), positron emission tomography, ultrasonography, and optical coherence tomography[2]. MR, due to its non-invasive nature, superior soft-tissue contrast resolution and lack of ionizing radiation exposure, has evolved as an ever-attractive choice[3]. Based on the scale of the target vasculature, MR vascular imaging can be further classified into two subcategories: macroscopic vascular imaging and microscopic vascular imaging[4]. Macroscopic vascular imaging, as the name suggests, assesses diseases of any “macro” blood vessels, including the aorta, the coronary, and the sizable arteries in the brain and the limbs. Classically, macroscopic vascular imaging techniques can be categorized into bright-blood and dark-blood techniques[3]. As a bright-blood technique, MR angiography, which can be achieved by exploiting either contrast-enhanced[5,6] or non-contrast (i.e., time-of-flight and steady-state free precession)[7–9] technologies, has advanced to an indispensable tool in the evaluation of macro vessels in the routine clinical practice. Dark-blood macroscopic vascular imaging, also called vessel wall imaging (VWI), has seen an

exponential increase in popularity and clinical applicability in recent years[10,11], due to its ability to directly probe pathological changes within the vessel wall. In contrast, microscopic vascular imaging has concentrated upon “micro” blood vessels, including small arteries, arterioles, venules, and capillaries, with permeability and/or perfusion quantification used to assess vessel changes at the microscopic level[4]. Dynamic contrast-enhanced MR (DCE-MR)[12] and dynamic susceptibility contrast-enhanced (DSC-MR)[13] are two widely used methods for permeability and perfusion assessment, respectively. By administrating a paramagnetic contrast agent (CA) and rapidly acquiring sequential images during the passage of CA through a given microvascular environment, DCE-MR can quantify vascular permeability-related properties, such as fractional plasma volume ($\mathrm{v_p}$), transfer constant ($\mathrm{K^{trans}}$), and fractional extravascular-extracellular volume ($\mathrm{v_e}$), and DSC-MR can quantify hemodynamic perfusion-related properties, such as cerebral blood volume (CBV), and cerebral blood flow (CBF). In recent years, with advancements in imaging and reconstruction technologies, both MR macroscopic vascular imaging and microscopic vascular imaging have been included in clinical workflows for a variety of diseases. For example, MR macroscopic vascular imaging, especially MR angiography, is nearly always adopted as an adjunct in stroke etiology evaluation workup[14], while MR microscopic vascular imaging enables non-invasive evaluation of brain tumors, providing insights into their diagnosis, progression, and treatment response[15]. However, some major technical challenges of current MR macroscopic and microscopic vascular imaging techniques hinder the further exploiting of them in stroke etiology evaluation and brain cancer evaluation, respectively. Thus, the development of novel MR vascular imaging

techniques to overcome the limitations and enhance their values in real clinical evaluation workflows of different diseases is of great significance.

1.2 MR MACROSCOPIC VASCULAR IMAGING IN STROKE ETIOLOGY EVALUATION

1.2.1 Overview of ischemic strokes

Stroke is a leading cause of death and disability worldwide. The majority of strokes are ischemic strokes. Each year in the United States, approximately 795,000 people experience a stroke of which 87% are ischemic in origin[16]. Ischemic strokes can result from a variety of causes[17] and several diagnostic algorithms have been developed to categorize ischemic strokes according to the etiology[18]. Causative Classification of Stroke (CCS) system classifies stroke patients in clinical trials into 4 mechanism categories: strokes related to (a) large-vessel diseases, (b) lacunar strokes, (c) cardioembolic strokes and (d) cryptogenic strokes, which are symptomatic cerebral infarcts for which no probable cause is defined after diagnostic evaluation[19]. Rapid and accurate identification of the corresponding stroke etiology would allow for a prompt delivery of appropriate treatment and thus a better patient outcome[20,21].

1.2.2 Current stroke etiology evaluation workup

In contemporary practice, the routine evaluation of the patient with ischemic stroke includes several components[22], as demonstrated in Figure 1.1. The topographic features of the stroke (i.e., infarct location and multiplicity) are assessed by brain MR (typically by

diffusion sequences), or brain CT when brain MR is not available. The head, neck, and thoracic vessels are assessed by CT or MR angiography, which have been demonstrated to have similar sensitivity and specificity. Echocardiography is used to assess the existence of thrombi in the cardiac structure. Transthoracic echocardiography (TTE), which is better at ventricular imaging, is utilized first in patients with coronary artery disease, congestive heart failure, or other ventricular disease that is evident from history or electrocardiogram (ECG). Transesophageal echocardiography (TEE), which is better at atrial and aortic-arch imaging, is favored in patients with non-lacunar infarct and no indication of ventricular disease and as an additional test in patients with unrevealing TTE results. Cardiac dysrhythmias are initially assessed by 12-lead ECG and inpatient cardiac telemetry or 24-hour Holter monitor, and hematologic disorders are screened through red-cell and platelet counts.

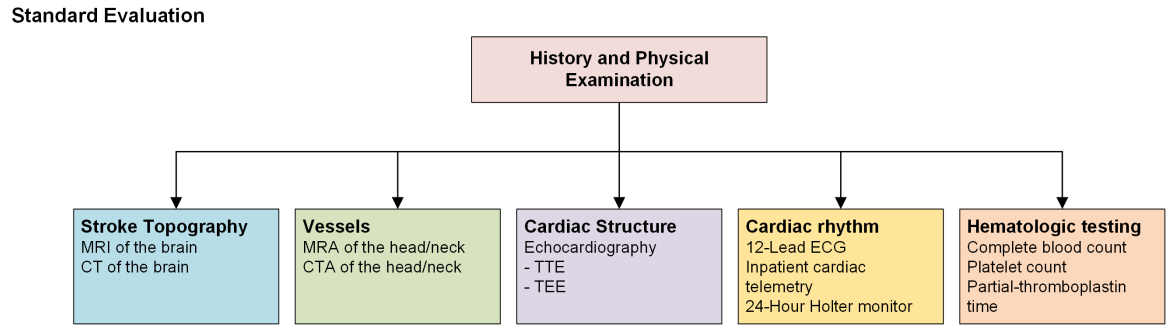

Figure 1.1 Routine stroke etiology evaluation workup in current clinical practice. Redrawn after Saver (2016)

1.2.3 Technical challenges and potential solutions with advanced MR macrovascular imaging

As shown in Figure 1.1, medical imaging is a major component in routine stroke etiologic evaluations; yet, current paradigm is suboptimal, which potentially accounts for 15 to 40%

of all ischemic strokes diagnosed with cryptogenic after the standard etiology workup[23]. First, detection of vessel-related pathologies relies solely on the degree of vascular narrowing measured by lumen-based imaging modalities. However, since most vascular pathology commences within the vessel walls, these modalities may have decreased sensitivity in detecting early vascular changes[24]. For example, intracranial atherosclerotic changes begin with deposition of an intimal “fatty streak”, which causes inflammation and intimal thickening followed by luminal stenosis[25]. Therefore, caliber changes are secondary and may reflect late stages. In this sense, it would be preferrable to add MR VWI, a dark-blood technique for MR macroscopic vascular imaging, to the existing standard etiology evaluation. Second, diagnosis of certain etiologies is conducted by utilizing suboptimal and invasive imaging procedures. Specifically, echocardiography is the current gold-standard for examining the thoracic aorta and the cardiac structure[26]. Nonetheless, this imaging modality is inherently suboptimal due to inadequate acoustic windows and highly operator dependent, not to mention the invasiveness of TEE. Given the unique advantages of MR, introducing MR macrovascular imaging (i.e., VWI and MR angiography) to help detect thrombi in the thoracic aorta or the cardiac chambers would be the future trends.

1.3 MR MICROSCOPIC VASCULAR IMAGING IN BRAIN CANCER EVALUATION

1.3.1 Overview of brain cancers

Brain and other central nervous system cancers are among the most fatal cancers and account for substantial morbidity and mortality[27]. Approximately 67,900 new brain tumors are diagnosed each year in the United States (21 per 100,000 people), of which 44,910 are malignant[28]. Despite considerable breakthroughs in various diagnostic and therapeutic techniques in recent years, the prognosis of malignant tumors remains dismal. Tumor-associated neovascularization is a typical tumor characteristic that indicates multiple biological behaviors, including tumor progression and resistance to therapy[29]. Hence, visualization of tumor microscopic vasculatures is of great importance for improved diagnosis, treatment planning, and post-therapy assessment of brain tumors[30].

1.3.2 Current brain cancer evaluation protocol

As the mainstay of modern neuroimaging, MR is the standard-of-care imaging modality for brain cancer evaluation. Table 1.1 outlines the minimal consensus recommendations for routine brain cancer imaging with MR on 3-T[31].

Table 1.1 Current consensus recommendations for a standardized brain cancer MR imaging protocol on 3-T

	T1w Pre	FLAIR	DWI		T2w	T1w Post
Sequence	IR-GRE	TSE	EPI		TSE	IR-GRE
Plane	Sagittal/axial	Axial	Axial		Axial	Sagittal/axial
Mode	3D	2D	2D		2D	3D
TR	2100 ms	> 6000 ms	> 5000 ms		> 2500 ms	2100 ms
TE	Min	100 - 140 ms	Min		80 - 120 ms	Min
TI	1100 ms	2500 ms	–	CA Injection	–	1100 ms
Flip angle	10° - 15°	90°/≥ 160°	90°/180°		90°/≥ 160°	10° - 15°
FOV	256 mm	240 mm	240 mm		240 mm	256 mm
Phase	256	≥ 256	128		≥ 256	256
Frequency	256	≥ 256	128		≥ 256	256
Thickness	1 mm	3 mm	3 mm		3 mm	1 mm
PI	Up to 2×	Up to 2×	Up to 2×		Up to 2×	Up to 2×
Scan time	5 - 8 min	4 - 5 min	3 - 5 min		3 - 5 min	5 - 8 min

Abbreviations: T1w Pre – pre-contrast T1-weighted imaging; FLAIR – fluid-attenuated inversion recovery; DWI – diffusion-weighted imaging; T2w – T2-weighted imaging; T1w Post – post-contrast T1-weighted imaging; IR-GRE – inversion-recovery gradient-recalled echo; TSE – turbo spin-echo; EPI – echo-planar imaging; TR – repetition time; TE – echo time; TI – inversion time; FOV – field-of-view; PI – parallel imaging

In the past decade, numbers of clinical trials have demonstrated that in addition to the conventional morphological imaging sequences listed in Table 1.1, MR microscopic vascular imaging techniques such as DCE-MR and DSC-MR are indispensable to the neurosurgeon and can make contributions to various applications, including tumor grading[32–34], surgical planning[35], and treatment response assessment[36,37]. Hence, in most cases, either DCE-MR or DSC-MR has been added to the recommended protocol prior to acquisition of post-contrast images[38–40]. Some guidelines even recommend inserting 2 separate DSC-MR sequences to address the CA leakage issue due to blood-brain barrier

(BBB) breakdown[41]. Specifically, following standard pre-contrast sequences, low-flip angle (30°) DSC-MR imaging without contrast agent preload using a single bolus CA injection is performed. Subsequently post-contrast images are obtained, and a second DSC-MR imaging is conducted using an intermediate flip angle (60°) and otherwise identical acquisition parameters as the first DSC-MR acquisition.

While both permeability and perfusion parameters are often cited for assessing microvascular environment of brain tumors, previous studies have demonstrated that they may provide different but complementary information[34]. For instance, at visual analysis, DCE-MR imaging usually shows superior sensitivity for identification of the viable tumor portion, and DSC-MR usually demonstrates superior specificity for diagnosing radiation necrosis[42]. Therefore, the comprehensive analysis of perfusion and permeability metrics may form a more complete basis for tumor evaluation than with either one alone and thus improve diagnostic and prognostic performance[42,43]. To achieve this, specifically, during the brain tumor evaluation session, DCE-MR imaging is performed with a single-dose of CA injection following the pre-contrast protocol. After a 5 – 8-minute interval, the DSC-MR sequence is acquired followed by post-contrast scans.

1.3.3 Technical challenges and potential solutions with advanced MR microvascular imaging

As mentioned above, to achieve simultaneous permeability and perfusion analysis, the typical way is to acquire both DCE-MR and DSC-MR sequences separately within one imaging session[44]. However, this requires multiple doses of CA injections, which leads to a big concern throughout the entire radiology community – the gadolinium deposition in

body tissues. The safety of gadolinium-based CA has recently been brought to public attention due to the findings that gadolinium can deposit in the brain and other body parts in patient with normal renal function[45–47]. Although the long-term clinical effects of gadolinium deposition remain unclear, the benefits and hazards of using gadolinium-based CA in clinical activities can be controversial. According to previous studies, gadolinium accumulation is dose-dependent, with more deposition seen in patients who received a higher cumulative dosage[46], implying that a lower dose may lessen the potential risks induced by gadolinium deposition. Hence, given the recent restrictions implemented by the Food and Drug Administration on the use of CA[48,49], it would be preferable to develop novel microscopic vascular imaging techniques with lower gadolinium injection that can provide permeability and perfusion information simultaneous without losing the diagnosis power.

1.4 OBJECTIVE

According to the discussions in previous sections, based on the current states of MR macroscopic and microscopic vascular imaging in specific clinical applications, the broad, long-term goal of the project in this dissertation is two-fold. First, we aim to develop a novel 2-station MR macroscopic vascular imaging strategy which could serve as a complement for current standard evaluation for stroke etiology to better leverage the inherent advantages of MR imaging and to enhance the clinical values of MR vascular imaging in stroke etiology evaluation (Aim 1 and Aim 2). Second, we aim to develop an optimized MR microscopic vascular imaging framework that can achieve simultaneous

permeability and perfusion quantification with a single dose of CA injection to improve the overall workflow for brain cancer evaluation (Aim 3).

1.4.1 Aim 1: To develop a novel motion-compensated, data-driven accelerated 3D MR VWI for the evaluation of the head-neck arteries

In Aim 1, we present the first component of our novel 2-station MR macrovascular imaging strategy that focuses on the head-neck vasculature. Specifically, a dark-blood VWI technique is proposed, which enables direct visualization of the pathologic changes within the vessel wall structures. The technique is implemented based on 3D variable-flip-angle turbo spin-echo (TSE) sequence, the basic physics of which are provided in Chapter 2. Our technical development is comprised of two subprojects. First, because of the submillimeter spatial resolutions and 3D encoding strategy, VWI is inherently susceptible to patient motion. In Chapter 3, we first investigate the effect of localized movement on 3D MR VWI and develop a novel motion-compensation approach combining volumetric navigator (vNav) and self-gating (SG) to simultaneously compensate for bulk and localized movements. The proposed vNav-SG technique is validated on 15 healthy subjects and 3 ischemic stroke patients with overall image quality and vessel wall sharpness adopted as evaluation metrics. Another drawback of conventional VWI is the relatively long scan time, which may affect patient experiences and potentially exacerbate the motion problem. In Chapter 4, a deep learning-based image reconstruction framework, cascaded multi-scale wavelet with iterative refinement network (CAMWARE), is presented for accelerated MR VWI. Evaluated on 6 ischemic stroke patients clinically diagnosed of intracranial atherosclerosis, CAMWARE is compared with conventional reconstruction methods and a state-of-the-art deep learning-based model (i.e., variational

network). Vessel wall sharpness and atherosclerotic plaque delineation are measured to assess the application-specific performance of CAMWARE.

1.4.2 Aim 2: To develop a novel MR multitasking-based multidimensional assessment of cardiovascular system (MT-MACS) technique for the evaluation of the thoracic aorta and the cardiac chambers

In Aim 2, another component of the 2-station MR macrovascular imaging strategy is developed which produces multidimensional assessment of cardiovascular system with ECG-free and respiratory navigator-free data acquisition. Specifically, within a clinically feasibility scan time, the proposed MT-MACS technique offers multiple image contrasts and phase-resolved image series for comprehensive evaluation. The technical development is based on MR multitasking framework, the general introduction of its image model and reconstruction pipeline are described in Chapter 2. In Chapter 5, the developed MT-MACS technique with a basic Cartesian sampling trajectory is first applied to thoracic aortas for proof of concept. In Chapter 6, we further extend the spatial coverage of MT-MACS to cover the entire heart as well as the thoracic arteries and switch the sampling trajectory from Cartesian to advanced tiny-golden-angle radial sampling to resolve more complex cardiac motion. Nine healthy subjects are recruited for the feasibility study. Both qualitative (i.e., overall image quality score) and quantitative (i.e., myocardial wall thickness of the 4 cardiac chambers and left ventricular ejection fraction) analyses are performed.

1.4.3 Aim 3: To develop a novel MR multitasking-based dynamic imaging for cerebrovascular evaluation (MT-DICE) technique for simultaneous permeability and leakage-insensitive perfusion quantification

In Chapter 7, another microscopic vascular imaging application of MR multitasking framework named dynamic imaging of cerebrovascular evaluation (MT-DICE) technique is presented to achieve comprehensive evaluation of microvascular environments. Specifically, permeability and leakage-insensitive perfusion metrics are provided simultaneous based on dynamic T1/T2* mapping with a single-dose CA injection. The feasibility of MT-DICE is tested on both healthy subjects and brain cancer patients. Specifically, 8 healthy subjects and 4 patients with known brain cancers are recruited for the study in which a 7.6-min MT-DICE scan is acquired. T1/T2* measurements of MT-DICE are compared against corresponding reference methods on all healthy subjects. Permeability and leakage-insensitive perfusion parameters are derived in 3 repeat healthy subjects for intersession repeatability analysis.

CHAPTER 2

Background

2.1 BASIC THEORY OF VESSEL WALL IMAGING SEQUENCES

MR imaging owns the potential to achieve high-spatial-resolution imaging with versatile image contrasts. In many vascular applications, it is preferrable to suppress the blood signal in order to visualize the surrounding vessel wall structure with high conspicuity and characterize pathologic changes within the vessel wall. This is so-called vessel wall imaging (VWI). 3D variable-flip-angle turbo spin-echo (TSE) sequence is currently the method of choice for MR VWI. To provide a better overview of this type of sequence, in this section, basic spin-echo sequence is introduced first from a mathematical point of view. The benefits of turbo spin-echo sequences with a variable-flip-angle echo train over conventional turbo spin-echo sequences is then discussed. Lastly, mechanisms of how variable-flip-angle TSE sequences achieve dark-blood contrast are briefly gone through.

2.1.1 Two-pulse spin-echo sequence

For a spin-echo sequence, at least two pulses, including one excitation pulse and one refocusing pulse, are needed to form a spin echo. Specifically, an α_1 excitation pulse rotates the longitudinal magnetization for the voxel to the transverse plane, and an α_2 refocusing pulse refocuses a large number of dephased isochromats and generates an echo when the isochromats reach a new phase coherence. From a more mathematical

point of view, for generality, the two-pulse spin-echo sequence can be formulated as follows:

$$\alpha_{1,y} - \tau - \alpha_{2,y} \tag{2.1}$$

where we assume both the excitation pulse and refocusing pulse are applied along the y direction in the rotating frame of reference. Defining the initial magnetization at equilibrium as $(M_x, M_y, M_z)^T = (M_x^0, M_y^0, M_z^0)^T = (0,0,M_0)^T$, after applying the $\alpha_{1,y}$ pulse, we have:

$$\begin{bmatrix} M_x \\ M_y \\ M_z \end{bmatrix} \xrightarrow{\alpha_{1,y}} \begin{bmatrix} M_x \cos\alpha_{1,y} - M_z \sin\alpha_{1,y} \\ M_y \\ M_x \sin\alpha_{1,y} + M_z \cos\alpha_{1,y} \end{bmatrix} = \begin{bmatrix} -M_0 \sin\alpha_{1,y} \\ 0 \\ M_0 \cos\alpha_{1,y} \end{bmatrix} \tag{2.2}$$

According to the Bloch equation, after the τ interval between the excitation and refocusing pulses, the magnetization components take the following set of values:

$$\begin{bmatrix} M_x \\ M_y \\ M_z \end{bmatrix} \xrightarrow{\tau} \begin{bmatrix} \left(M_x \cos\omega\tau + M_y \sin\omega\tau\right) e^{-\tau/\mathrm{T2}} \\ \left(-M_x \sin\omega\tau + M_y \cos\omega\tau\right) e^{-\tau/\mathrm{T2}} \\ M_0\left(1 - e^{-\tau/\mathrm{T1}}\right) + M_z e^{-\tau/\mathrm{T1}} \end{bmatrix} = \begin{bmatrix} -M_0 \sin\alpha_{1,y} \cos\omega\tau e^{-\tau/\mathrm{T2}} \\ M_0 \sin\alpha_{1,y} \sin\omega\tau e^{-\tau/\mathrm{T2}} \\ M_0[1 - (1 - \cos\alpha_{1,y}) e^{-\tau/\mathrm{T1}}] \end{bmatrix} \tag{2.3}$$

where ω denotes the precession frequency of a representative isochromat. Similarly, the transverse magnetization immediately after the second $\alpha_{2,y}$ refocusing pulse can be written as:

$$\begin{aligned} M_{xy} = {} & M_0 \sin\alpha_{1,y} \left(\sin^2 \frac{\alpha_{2,y}}{2} e^{-i\omega t} - \cos^2 \frac{\alpha_{2,y}}{2} e^{i\omega t}\right) e^{-\tau/\mathrm{T2}} \\ & - M_0[1 - (1 - \cos\alpha_{1,y}) e^{-\tau/\mathrm{T1}}] \sin\alpha_{2,y} \end{aligned} \tag{2.4}$$

Hence, considering the free precession about the z direction, the spin-echo signal can be expressed as:

$$S(t) = \sin\alpha_{1,y} \sin^2 \frac{\alpha_{2,y}}{2} \int \rho(\omega) e^{-\tau/\mathrm{T2}(\omega)} e^{-i\omega(t - \mathrm{T_E})} d\omega \tag{2.5}$$

where $T_E = 2\tau$ represents the echo time. When $\alpha_{1,y} = 90°$ and $\alpha_{2,y} = 180°$, this signal equation reaches its maximum value, as illustrated in Figure 2.1.

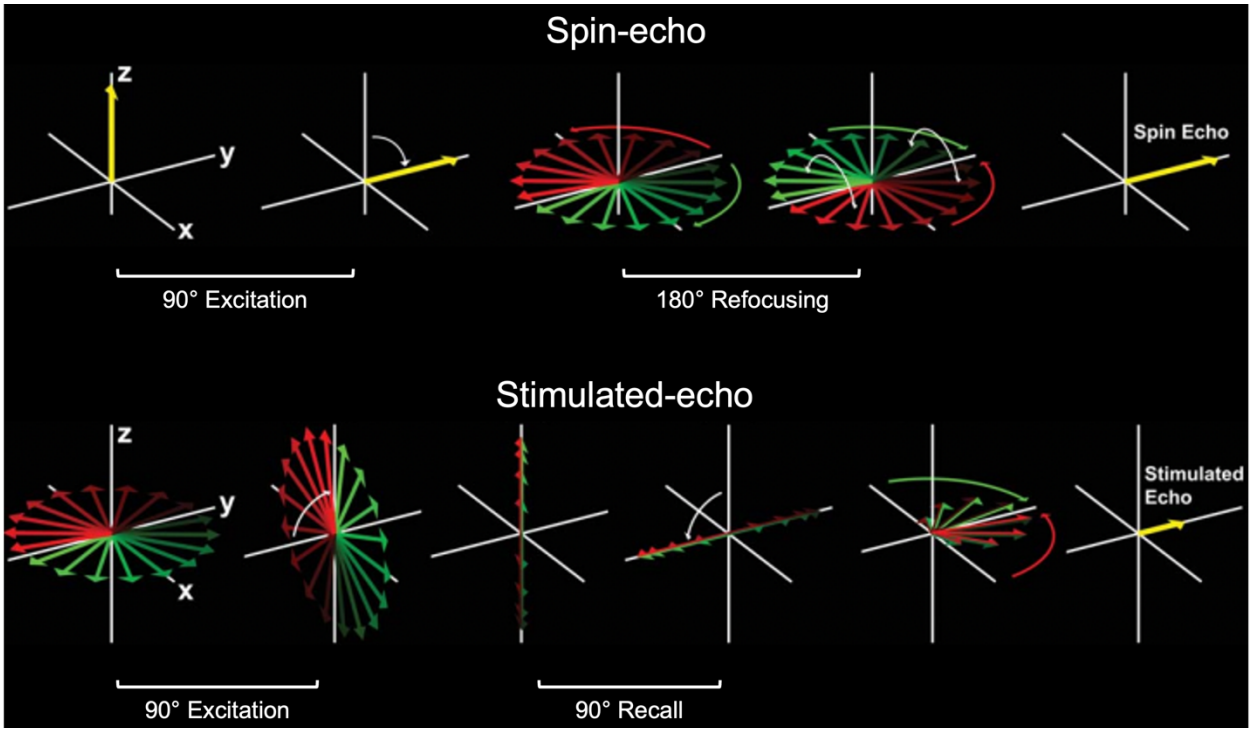

Figure 2.1 Illustration of the formation of spin-echo and stimulated-echo. Redrawn after Mugler (2014)

2.1.2 Variable-flip-angle TSE sequence

Conceptually, TSE sequence is a simple extension of the basic two-pulse spin-echo sequence to increase the acquisition efficiency. It is designed to generate multiple spin echoes, each of which is individually phase- or frequency-encoded to cover k-space, following each excitation pulse. The typical TSE sequence adopts relatively large flip angles for the refocusing pulses, generally equal to or at least near 180°. According to the pervious section, the echo signal reaches its maximum value when a 180° refocusing pulse is applied, which means all the transverse magnetization generated by the excitation pulse is refocused. Yet, in this scenario, the duration of echo train is typically

less than the T2 values of primary interest for short TE_{eff}, such as in our vessel wall imaging application. Longer echo train durations tend to result in degraded image contrast and artifacts such as blurring[50–52].

In recent years, variable-flip-angle TSE sequences have been introduced to achieve desirable signal behavior and lengthen the echo train length to further increase the acquisition efficiency[53]. The key idea is to include the stimulated-echo contribution (Figure 2.1) to the evolution of the echo train signal. During the storage period for the stimulated echo, the magnetization, which later forms the echo, decays according to the T1 relaxation time of the tissue, and T1 values are generally much longer than T2 values. Specifically, the initial portion of the variable-flip-angle adopts lower flip angle refocusing pulses and stores a large fraction of the magnetization along the z direction. Then, as the echo train proceeds, the stored magnetization is gradually converted to transverse plane, permitting relatively high signal amplitudes to be maintained for the entire echo train duration and therefore allowing for extended useable duration of the acquisition.

2.1.3 Dark-blood contrast of variable-flip-angle TSE sequence

TSE sequences, especially variable-flip-angle TSE sequences, exhibit excellent dark-blood contrast because of its high sensitivity to flow and motion. In general, there are two separate and additive flow-related mechanisms that contribute to the blood suppression, as illustrated in Figure 2.2[54]. One relates to the through-plane flow (Figure 2.2A), which leads to the flowing blood not experiencing either the excitation pulse or refocusing pulse, and therefore not creating an echo. Figure 2.2B demonstrates another mechanism relates to the flow-related dephasing of transverse magnetization caused by the heterogeneous accumulation of phase for flowing spins within a single voxel. This is particularly the case

in variable-flip-angle TSE sequences, where additional flow-related signal loss is caused by the phase differences between different echo pathways, including spin-echo and stimulate-echo, which lead to an echo formation with lower magnitude.

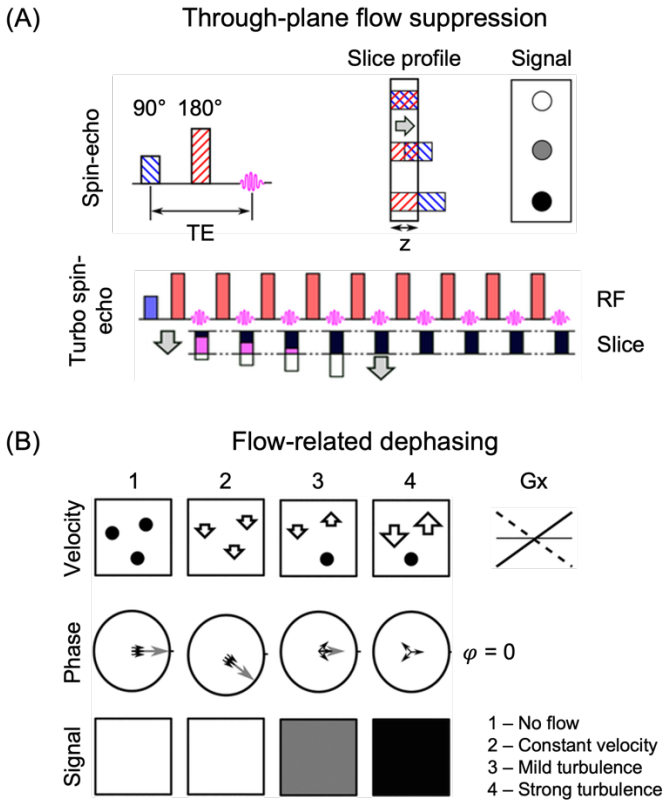

Figure 2.2 Two separate and additive flow-related mechanisms that contribute to blood suppression for the variable-flip-angle TSE sequence. Redrawn after Henningsson (2022)

2.2 MR MULTITASKING FRAMEWORK

2.2.1 Image model

MR multitasking[55] represents the multi-dimensional images as a multi-dimensional array (or tensor). To reconstruct MR images, the standard way is to fill in the tensor structure at the Nyquist sampling rate; however, this will suffer from the “curse of dimensionality”,

where the scan time grows exponentially with the number of dynamics. Instead, because of the strong correlation between images, MR multitasking framework models this tensor as a low-rank tensor (LRT) and can be decomposed to the product of several factor matrices. Therefore, by leveraging the spatial-temporal correlation, the task for recovering the tensor can now be switched to recover the factor matrices and thus achieve a vastly accelerated scan[56–58]. Specifically, images in Multitasking framework are represented as a multidimensional function $I(\mathbf{r}, t_1, t_2, \cdots, t_N)$ of spatial location $\mathbf{r} = [x\ y\ z]^T$ and N time dimensions $t_1, t_2, \ldots, t_N$. Each time dimension corresponds to a specific "task" to be resolved. The image function can be formulated as a $(N+1)$-way tensor $\mathcal{I}$ consisting of elements $\mathcal{I}_{jkm\cdots q} = I(\mathbf{r}_j, t_{1,k}, t_{2,m}, \cdots, t_{N,q})$ with voxel location $\{\mathbf{r}_j\}_{j=1}^{J}$ and each time dimension from $\{t_{1,k}\}_{k=1}^{K}$ to $\{t_{N,q}\}_{q=1}^{Q}$. The high image correlation along different time dimensions and across the spatial and time dimensions renders $\mathcal{I}$ to be an LRT and can be decomposed into the product of a core tensor $\mathcal{C}$ and $N+1$ factor matrices:

$$\mathcal{I} = \mathcal{C} \times_1 \mathbf{U}_{\mathbf{r}} \times_2 \mathbf{U}_{t_1} \times_3 \mathbf{U}_{t_2} \times_4 \cdots \times_{(N+1)} \mathbf{U}_{t_N} \tag{2.6}$$

where the operator $\times_i$ denotes the ith mode product, the factor matrix $\mathbf{U}_{\mathbf{r}} \in \mathbb{C}^{J \times L}$ contains L spatial basis functions, each of which comprises J voxels, each factor matrix $\mathbf{U}_{t_i}$ contains L_i basis function for ith time dimension, and the core tensor $\mathcal{G} \in \mathbb{C}^{L \times L_1 \times \cdots \times L_N}$ is the coefficient dominating the interaction between factor matrices.

2.2.2 Sampling strategies and image reconstruction

To recover the core tensor and multiple factor matrices, our approach is to collect two interleaved sets of data as illustrated in Figure 2.3. First of all, the imaging data $\mathbf{d}$ is

collected by random sampling with extensive k-space coverage to determine the spatial factor matrix $\mathbf{U_r}$ by iteratively solving the following optimized problem:

$$\widehat{\mathbf{U}}_\mathbf{r} = \arg\min_{\mathbf{U_r}} \|\mathbf{d} - \Omega(\mathbf{FSU_r\Phi})\|_2^2 + R(\mathbf{U_r}) \tag{2.7}$$

where $\mathbf{d}$ denotes the collected imaging data, Ω is the sampling operator corresponding to the sampled k-space locations, $\mathbf{F}$ applies Fourier transform, $\mathbf{S}$ contains sensitivity information that applies multi-channel encoding, $\mathbf{\Phi}$ contains the temporal basis functions, the recovery of which will be discussed later, and $R(\cdot)$ represents the spatial regularization function.

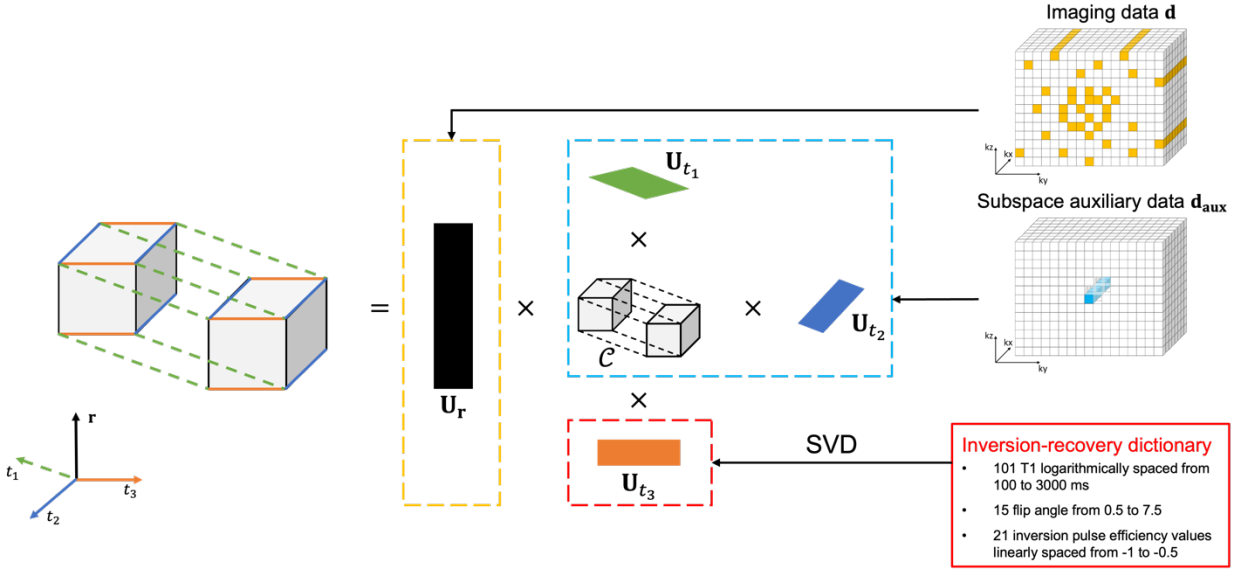

Figure 2.3 Illustration of sampling strategies and image reconstruction steps of MR multitasking framework

The temporal factor matrices, which are included in $\mathbf{\Phi}$, are recovered through another subset of data, called subspace auxiliary data $\mathbf{d_{aux}}$, which is collected frequently enough at the center of the k-space. This subset of data does not need to contain tons of spatial information, but a wealth of temporal information is enough to resolve temporal changes along each time dimension. Depending on the application, the

temporal basis functions for some time dimensions can optionally be pre-determined even before any data are collected. Consider the example that we are going to recover the factor matrix $\mathbf{U}_{t_N}$ along inversion-recovery relaxation time dimension. Because T1 relaxation is physically governed by the well-known Bloch equations, a training dictionary of physically feasible signal curves can be readily generated ahead of time to reduce computation. Basically, the temporal basis functions along the inversion-recovery dimension are predefined from a T1 recovery dictionary of signals with different T1, B1 and inversion efficiency values. The inversion-recovery basis functions are then estimated from the singular value decomposition (SVD) of this dictionary. The remaining factor matrices other temporal dimensions as well as the core tensor are recovered from the subspace auxiliary data. In practice, due to the limited scan time, the measured subspace auxiliary data $\mathbf{d_{aux}}$ covers some combinations of physiological and physical dynamics experienced during the scan, but typically not all combinations. Therefore, the acquired training data tensor is incomplete and can be recovered by the following equation:

$$\widehat{\mathcal{D}}_{\text{aux}} = \arg\min_{\mathcal{D}_{\text{aux}}} \|\mathbf{d_{aux}} - \Omega(\mathcal{D}_{aux})\|_2^2 + \lambda \sum_i \left\|\mathbf{D}_{\mathbf{aux},(i)}\right\|_* + R(\mathcal{D}_{\text{aux}}) \tag{2.8}$$

where Ω is the sampling operator corresponding to the sampled k-space locations, and $R(\cdot)$ is a temporal regularization functional.

CHAPTER 3

Motion-compensated 3D MR Intracranial Vessel Wall Imaging: Development and Validation of a More Robust 3D Turbo Spin-echo Sequence

3.1 INTRODUCTION

Ischemic strokes arise from various intracranial vessel wall abnormalities, including atherosclerosis, vasculitis and Moyamoya syndrome[59]. Accurate identification of these pathologies may help elucidate stroke etiology and allow for a prompt delivery of appropriate treatment and thus favorable patient outcomes[20]. As introduced in Section 1.2.3, the current evaluations of stroke patients rely exclusively on assessments of the degree of luminal stenosis using lumenography-based imaging methods, which are however inadequate for differentiating diverse intracranial pathologic processes of the vessel wall[60,61].

MR VWI is a non-invasive modality that can directly visualize the structure and characterize pathologic changes within the vessel wall[11]. 3D variable-flip-angle TSE is currently the method of choice for intracranial VWI[62–64]. However, the relatively long scan time along with sub-millimeter spatial resolution renders this technique inherently susceptible to motion. The 3D acquisition fashion of MR imaging further exacerbates this challenge[65]. Resultant blurring or ghosting artifacts may lead to image quality degradation

and inaccurate qualitative and quantitative wall lesion assessment, or even completely unusable exams[66–68].

Motion artifacts typically observed in intracranial VWI may be caused by either head bulk motion or localized movement of internal anatomic structures. Head bulk motion, such as nodding and head rotation, implies changes in the patient's head position inside the MR scanner[69]. Internal localized movement includes sudden involuntary movements, such as coughing and yawning, and semi-regular movements, such as swallowing[70]. Although foam cushions are commonly used to minimize bulk motion, a subtle movement of the head position may still be critical given the fine vessel wall structure (0.5 ± 0.1 mm) as well as the demanding spatial resolution[71–73]. However, unlike the well-known image quality deterioration caused by head bulk motion, the effect of localized movement on intracranial VWI has been underexplored.

A motion-compensated strategy that can well mitigate motion effects caused by both head bulk motion and internal localized motion is highly desirable for 3D intracranial VWI. MR navigators are the traditional means of tracking head positions during brain imaging[74]. Tisdall et al. developed an echo planar imaging (EPI) based vNav approach to periodically collect low resolution volumetric images of the head and prospectively realign the imaging coordinates[75]. The effectiveness of this motion tracking technique in improving the imaging performance of subjects with head bulk motion has been demonstrated in conventional brain imaging[75]. However, localized motion is not resolved by vNav. A SG motion compensation strategy, which uses a one-dimensional projection of the imaging volume to detect the object's motion, was previously developed to reduce

swallowing-related motion artifacts in carotid VWI[65]. This could be a promising approach to mitigate localized movement effects on intracranial VWI.

In this chapter, the aim is two-fold. First, we investigated the effect of internal localized movement on intracranial VWI quality and demonstrated the effectiveness of the SG motion gating scheme in mitigating resultant motion artifacts in healthy subjects. Second, we developed a motion-robust intracranial VWI technique by incorporating a combined vNav-SG strategy into 3D variable-flip-angle TSE (aka. sampling perfection with application-optimized contrasts using different flip angle evolution [SPACE]). Demonstrated in healthy subjects and stroke patients, the developed vNav-SG SPACE sequence proved to be more robust for intracranial VWI than the conventional SPACE sequence when motion occurred.

3.2 METHODS

3.2.1 Motion compensation strategy and sequence design

The motion compensation strategy is built on the T1-weighted SPACE sequence in which each repetition time (TR) consists of a long train of variable-flip-angle nonselective refocusing radiofrequency (RF) pulses and a gap for magnetization restoration[53]. The schematic of the vNav-SG SPACE sequence is illustrated in Figure 3.1.

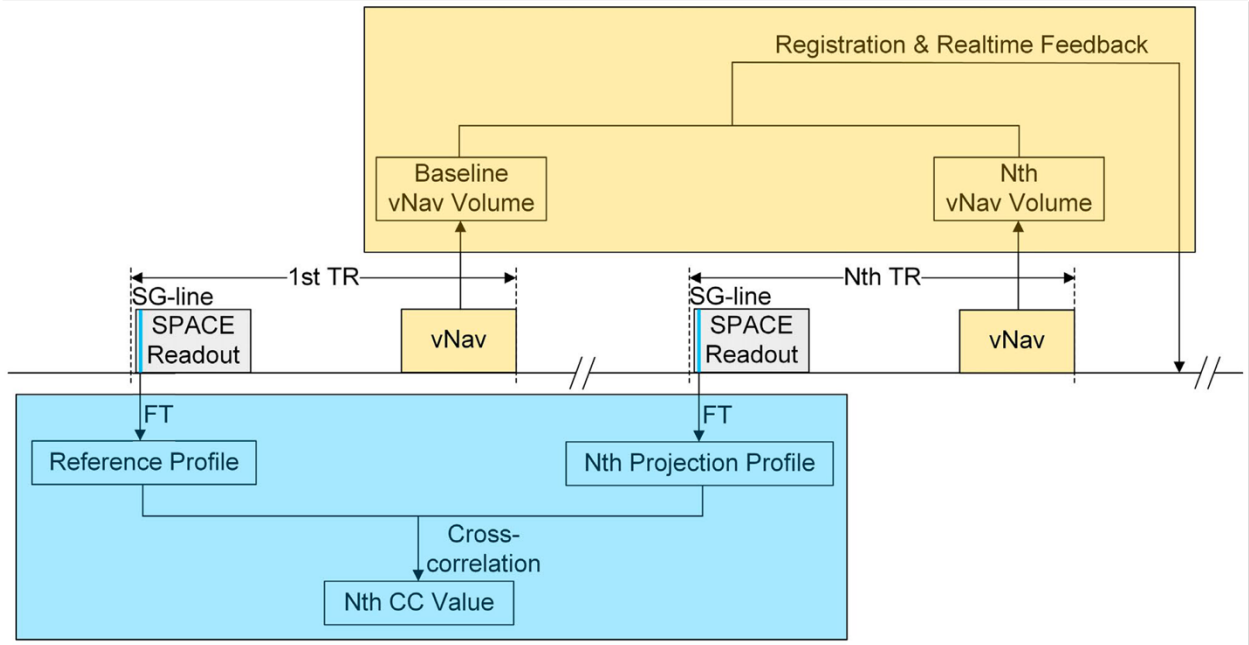

Figure 3.1 vNav-SG SPACE sequence diagram. For each TR, an SG line is first acquired from the first echo of the SPACE readout and is used to derive the projection profile of the entire imaging volume by Fourier transform (FT). The projection profiles acquired in later TRs are cross-correlated (CC) to the reference projection collected at the beginning of the scan, which is automatically reestablished when head position changes or signal drift occurs. All CC values are prioritized, and the most motion-affected TRs are reacquired at the end of the scan. The vNavs are implemented as a 3D-EPI module, consisting of acquisition, registration and communication, and are inserted at the end of each TR. The subsequent vNavs acquired in later TRs are registered back to the first navigator to realign the imaging coordinates

vNav is implemented as a 3D EPI module with 8-mm resolution and 256-mm field-of-view (FOV) in all three directions[75]. We insert one such 3D navigator at the end of each TR to ensure that motion estimation is as close as possible to its following SPACE readout train. Each of subsequent vNav acquired in a later TR is registered back to the navigator acquired at the first TR to realign the imaging coordinates. Registration of the volumetric navigators is performed based on the optimized Prospective Acquisition Correction (PACE) algorithm[69]. Low flip angle (2º) excitation is adopted in EPI to minimize the effect of the vNav on the final image contrast. The entire vNav module consumes approximately

355 ms, including data acquisition, image registration and communication, thus easily fitting the gap within each TR.

The SG method used to compensate for localized movement is a projection-based motion gating strategy[76]. A center k-space line along the superior-inferior direction, denoted as SG line, is acquired from the first echo of each SPACE echo train. The projection of the entire imaging volume is then derived by the Fourier transform of the SG line. The projection profiles acquired in subsequent TRs are cross-correlated (CC) to the reference projection originally collected at the beginning. Based on their CC values, which is an inverse surrogate for the severity of motion contamination, all acquired TRs are prioritized and the most motion-affected TRs are reacquired at the end of the scan. The number of allowed reacquisitions can be set through the user-interface. In addition, considering the potential signal drift, reference projection profiles will automatically update using a previous method[65].

3.2.2 In vivo study

The in vivo study was approved by the local institutional review board, and all subjects provided written informed consent before participation. All scans were performed on a 3-T MR system (MAGNETOM Skyra; Siemens Healthcare, Erlangen, Germany) equipped with a 20-channel head-neck coil. The coil element that is close to nasal and oral cavities was used to derive SG signals. A sagittally-oriented imaging volume was prescribed to cover the head and part of the neck[63]. Three spatial pre-saturation bands were applied to suppress the signals from the out-of-volume nose and ears.

Study I: To investigate the degradation effect of localized movement on intracranial VWI and the effectiveness of SG in artifact reduction

Eight healthy volunteers (4 males and 4 females, age range 23-59 years) were recruited in this study. All subjects underwent two vessel wall scans using the developed vNav-SG SPACE technique with the following imaging conditions:

1. Subject asked to remain still; imaging without vNav or SG (denoted as “No Motion”); and

2. Subject asked to conduct pre-designed localized movement; imaging with SG only (“W/ MOCO”).

Motion instructions were given over the intercom system at five preset stages. Specifically, subjects were asked to cough twice at the 50th, 150th, 250th, 350th, 450th TR of the scan. During the rest of the imaging period, subjects were asked to hold their head and neck still. In addition to the online-reconstructed images from the “W/ MOCO” scan, its raw data was also used to reconstruct motion-contaminated images (denoted as “W/O MOCO”) by retrospectively retrieving the data acquired in motion-corrupted TRs.

A previously used 8-min-long sequence setup for intracranial VWI was used[77], including FOV = 170 × 170 × 136 mm^3; matrix size = 320 × 320 × 256 with 6.7% slice oversampling; spatial resolution = 0.53 mm isotropic without interpolation; TR/TE = 900/16 ms; 6/8 partial Fourier in the partition-encoding direction; parallel imaging (GRAPPA) acceleration rate = 2 in the phase-encoding direction; echo-train-length = 52; number of reacquisitions = 30; 8.1-min acquisition time (a total of 542 TRs) without motion or vNav-SG.

Study II: To demonstrate the robustness of vNav-SG SPACE for intracranial VWI in the presence of both head bulk motion and localized movement

Seven healthy volunteers (3 males and 4 females, age range 29-48 years) and three ischemic stroke patients (2 males and 1 female, age range 58-75 years) were recruited. A 0.3-sec test shot was first run to allow changes of the navigator protocol for each specific subject, including the FOV dimensions and location. The protocol was saved and used as the basis for the vNav modules in our proposed sequence. Following the test shot, all healthy subjects underwent the “directed-motion” study using vNav-SG SPACE. Specifically, the study involved five separate scans with the following different imaging conditions:

1. Subject asked to remain still; imaging without vNav or SG (denoted as “W/O MO, W/O vNav-SG”);

2. Subject asked to conduct motion; imaging without vNav or SG (“W/ MO, W/O vNav-SG”);

3. Subject asked to conduct motion; imaging with vNav only (“W/ MO, W/ vNav”);

4. Subject asked to conduct motion; imaging with SG only (“W/ MO, W/ SG”); and

5. Subject asked to conduct motion; imaging with vNav and SG (“W/ MO, W/ vNav-SG”).

Motion instructions were given through the intercom system at eight preset stages. Subjects were asked to cough twice at four (100th, 170th, 230th and 300th TR) of the eight stages and change their head positions at the other four stages (130th, 200th, 270th and 330th TR). When changing head positions, subjects were asked to rotate their heads for less than 8º towards one of 4 directions (left, right, up and down), keep the position for 10 sec, and then return to the original position. During the rest of the imaging period, subjects were asked to hold their head and neck still.

An expedited SPACE imaging parameter setting was used to reduce the total study time, including FOV = 155 × 155 × 144 mm^3; matrix size = 256 × 256 × 224 with 7.1% slice oversampling; spatial resolution = 0.6 mm isotropic without interpolation; TR/TE = 900/16 ms; 6/8 partial Fourier in the partition-encoding direction; parallel imaging (GRAPPA) acceleration rate = 2 in the phase-encoding direction; echo-train-length = 52; number of reacquisitions = 30; 6-min acquisition time (a total of 400 TRs) without motion or vNav-SG.

Three ischemic stroke patients underwent two consecutive SPACE scans, with and without vNav-SG, respectively, in a random order. The comparison was conducted after contrast injection and towards the end of the brain MRI/MRA examination when intra-scan motion often occurs because of patient intolerance. The same sequence setup as in *Study I* was used.

3.2.3 Image analysis

All 3D image sets were loaded to a workstation (LEONARDO; Siemens Healthcare, Erlangen, Germany) for processing and viewing. For *Study I*, vessel wall sharpness was measured at the inner and outer boundaries of four major vessel segments including middle cerebral arteries (MCA), internal carotid arteries (ICA), basilar arteries (BA) and vertebral arteries (VA). For this purpose, three contiguous 2D cross-sectional slices of 0.53-mm thickness were reconstructed with multiplanar reformation for each vessel segment. Sharpness was measured from three evenly distributed locations in each slice, with the first location selected at the most blurred position of the vessel wall boundary. The sharpness of each segment was then estimated by averaging across the nine selected locations. Measurement of vessel wall sharpness was based on a previously

developed method[65,78], using an in-lab MATLAB (R2018a, MathWorks, Natick, MA) program.

For *Study II* in healthy volunteers, all 35 image sets (5 imaging conditions × 7 subjects) were randomized and shown to a blinded neuroradiologist with 6 years' experience in intracranial VWI. The overall image quality for each image set was graded based on a five-point scale: 0-poor, 1-fair, 2-moderate, 3-good, 4-excellent. Vessel wall sharpness was measured, using the aforementioned methods, at the inner and outer boundaries of 2 major intracranial vessel segments (BA and MCA). For the patient study, the 3D SPACE images with and without vNav-SG underwent diagnostic evaluation by the same neuroradiologist, blinded to patient and sequence information.

All image sets from *Study II* were selected to assess the inter-reader reliability. An MR physicist with 3 years' experience in MR VWI re-graded the overall image quality scores and conducted sharpness measurement at the same vessel segments independently, following the same criteria and methods.

3.2.4 Statistical analysis

Statistical analyses were performed using SPSS (version 24; IBM, Armonk, NY). To compare vessel wall sharpness under different imaging conditions, a paired two-tailed Student's t-test was used for *Study I*. For *Study II*, inter-reader reliabilities of image quality scores and vessel wall sharpness were assessed by weighted Cohen's kappa (κ) and intraclass correlation coefficients (ICC), respectively. A paired two-tailed Wilcoxon signed-rank test was used for the comparison of image quality scores between the "With motion, with vNav-SG" scan and each of the other imaging conditions, and a paired two-

tailed Student's t-test was used for the comparison of vessel wall sharpness. A *P* value < 0.05 was considered to indicate statistical significance.

3.3 RESULTS

The vNav-SG SPACE imaging was performed successfully on all 15 healthy subjects and 3 ischemic stroke patients. For the scans with the SG functionality on, the number of motion-contaminated TRs detected by SG was greater than 30; thus, the number of actually reacquired TRs was 30.

3.3.1 Study I

In general, the internal localized movement caused by coughing resulted in noticeable blurring and noise at the vessels close to the nasal and oral cavities. These artifacts were well suppressed by reacquiring motion corrupted k-space lines detected by SG signals (Figure 3.2A – 3.2F). Representative time-courses of projection profiles and CC values were retrospectively derived and are shown in Figure 3.2G and 3.2H, respectively. The projection profile during coughing deviated substantially in magnitude, leading to drops in CC values.

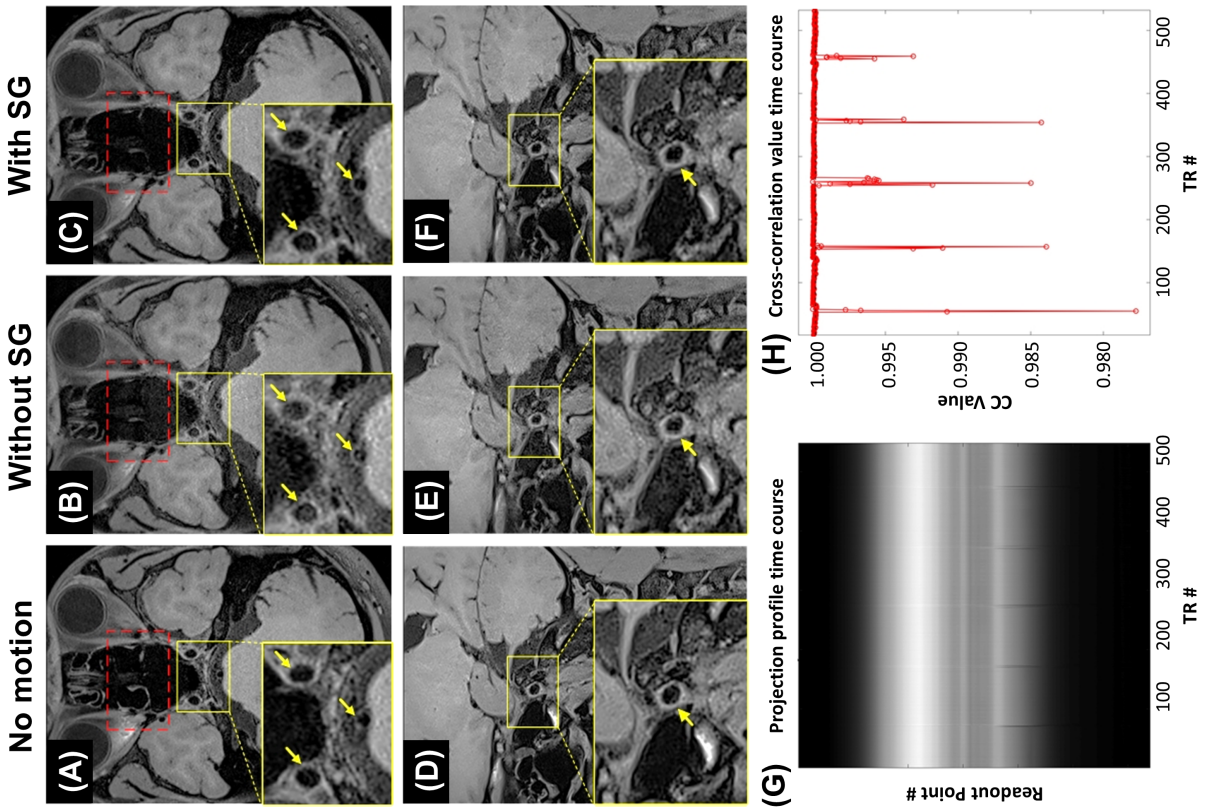

Figure 3.2 A-F, Representative images demonstrating the effect of localized motion, caused by coughing, on intracranial vessel wall imaging, and the effectiveness of the SG motion-gating technique in mitigating motion artifacts in a representative healthy control. Coughing introduced noise (red dotted box) and substantially obscured vessel wall boundaries (yellow arrows), particularly at the internal carotid artery and basilar artery (A-C) and middle cerebral artery (D-F). The proposed SG technique dramatically mitigated artifacts and provided comparable vessel- wall delineation quality to the scan without motion ("No motion"). G,H, Retrospectively derived representative time courses of projection profiles (G) and CC values (H). In contrast to the projection profiles devoid of motion, motion- contaminated projection profiles deviated substantially in magnitude and were always detected by the SG signal

Localized movements significantly reduced vessel wall sharpness at either the outer or inner vessel wall boundary compared with that obtained in "With SG" scans, as shown in Table 3.1 (BA outer: 0.68 ± 0.27 vs. 0.86 ± 0.17, P = 0.037; VA outer: 0.43 ±

0.29 vs. 0.93 ± 0.29, P = 0.003; VA inner: 0.37 ± 0.23 vs. 0.99 ± 0.32, P = 0.001; ICA outer: 1.35 ± 0.24 vs. 1.61 ± 0.19, P = 0.034; ICA inner: 0.86 ± 0.30 vs. 1.34 ± 0.20, P < 0.001). The sharpness of wall boundaries was preserved by exploiting SG when imaging subjects with localized motion, comparable to that obtained in the "No motion" group except for the MCA outer (0.77 ± 0.30 vs. 0.97 ± 0.24, P = 0.047) and ICA inner (1.34 ± 0.20 vs. 1.66 ± 0.15, P = 0.029) boundary.

Table 3.1 Vessel wall sharpness measurement results at the outer and inner boundary of four major intracranial vessel segments, including middle cerebral arteries (MCA), basilar arteries (BA), vertebral arteries (VA) and internal carotid arteries (ICA), within the imaging conditions in *Study I*.

Imaging Conditions	**Vessel Segments**	**Sharpness of Wall Boundary (mm^{-1})**			
		Outer Boundary	*P* value	Inner Boundary	*P* value
No motion	MCA	0.97 ± 0.24	**0.047**	0.78 ± 0.14	0.362
	BA	1.03 ± 0.28	0.160	0.68 ± 0.25	0.689
	VA	1.02 ± 0.34	0.147	1.20 ± 0.30	0.275
	ICA	1.89 ± 0.26	0.058	1.66 ± 0.15	**0.029**
With SG	MCA	0.77 ± 0.30	NA	0.70 ± 0.22	NA
	BA	0.86 ± 0.17	NA	0.66 ± 0.15	NA
	VA	0.93 ± 0.29	NA	0.99 ± 0.32	NA
	ICA	1.61 ± 0.19	NA	1.34 ± 0.20	NA
Without SG	MCA	0.65 ± 0.37	0.243	0.62 ± 0.31	0.435
	BA	0.68 ± 0.27	**0.037**	0.60 ± 0.31	0.385
	VA	0.43 ± 0.29	**0.003**	0.37 ± 0.23	**0.001**
	ICA	1.35 ± 0.24	**0.034**	0.86 ± 0.30	**< 0.001**

3.3.2 Study II

Compared with regular SPACE imaging in the absence of motion (Figure 3.3A), motion artifacts led to severe blurring of vessel wall boundaries, impaired wall continuity and reduced wall-tissue contrast (Figure 3.3B), which were suppressed by either vNav (Figure 3.3C) or SG (Figure 3.3D). Note that, compared to vNav-only, the addition of the SG approach to vNav further improves delineation of the small vessels close to nasal and oral cavities (arrowheads in Figure 3.3C and 3.3E). Overall image quality was restored by the combined vNav-SG strategy in the presence of motion (Figure 3.3E).

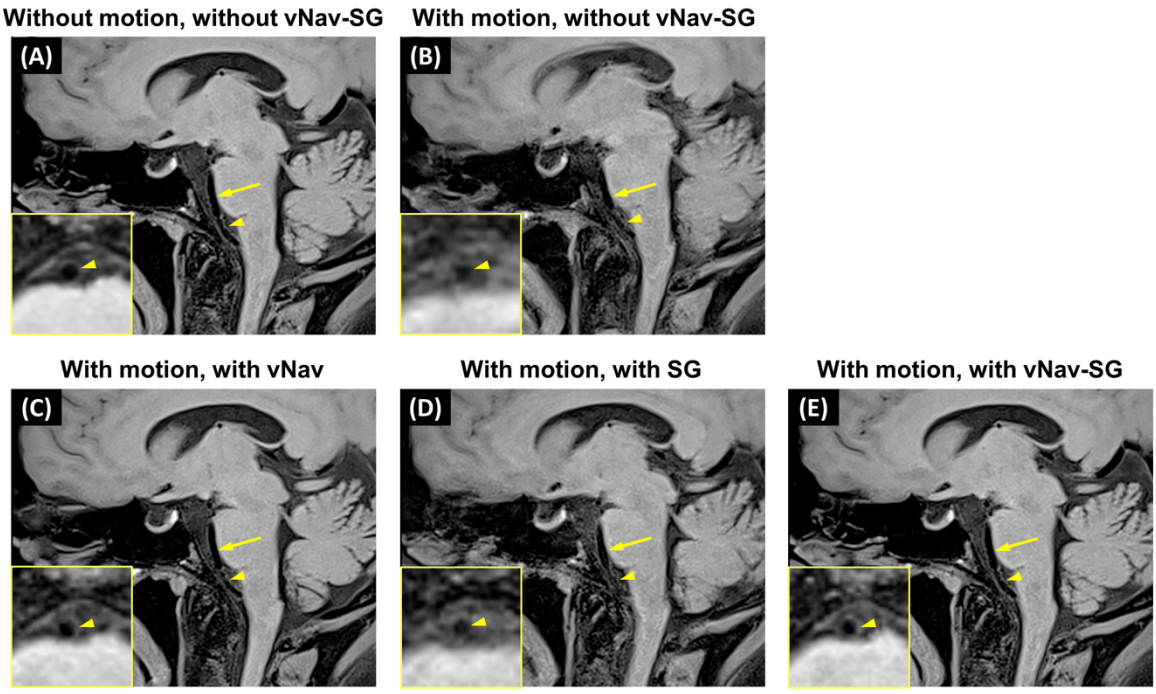

Figure 3.3 Imaging results of the five imaging conditions in 1 representative healthy subject in *Study II*. Compared with conventional SPACE imaging without subject motion (A), combined bulk head motion and internal localized movement severely degraded image quality as well as vessel wall delineation (yellow arrows and arrowheads) (B). C,D, Motion artifacts were suppressed if either vNavs or the SG approach was used, respectively. Compared with vNav-only, the addition of the SG strategy further improves delineation of the small vessel close to nasal and oral cavities

(yellow arrowheads). E, Overall image quality was significantly improved by adopting a combined vNav- SG technique

Inter-reader agreement was excellent for overall image quality analysis (Cohen's κ = 0.883, 95% CI 0.802 – 0.963). Inter-reader agreements for both outer and inner boundary at BA and MCA were all moderate to high (BA outer: ICC 0.768, 95% CI 0.570 – 0.921; BA inner: ICC 0.744, 95% CI 0.658 – 0.833; MCA outer: ICC 0.875, 95% CI 0.607 – 0.961; MCA inner: ICC 0.805, 95% CI 0.547 – 0.903).

Because of the moderate to high inter-reader agreement, the following analyses were based on the evaluation of the more experienced neuroradiologist. The motion compensation effects of vNav-SG were qualitatively validated by image quality scores (Table 3.2). Specifically, the average image quality score for "With motion, with vNav-SG" scans was significantly higher than that obtained in "With motion, without vNav-SG" scans (P = 0.026), and comparable to that obtained in "Without motion, without vNav-SG" scans (P = 0.317). Similar scores were acquired in "With motion, with vNav", "With motion, with SG" and "With motion, with vNav-SG" scans (P = 0.317 and P = 0.059, respectively), among which "With motion, with vNav-SG" provided the highest score.

Table 3.2 Image quality scores (5-point scale: 0-poor, 1-fair, 2-moderate, 3-good, 4-excellent) of the imaging conditions in *Study II* given by the experienced neuroradiologist.

	Condition 1	**Condition 2**	**Condition 3**	**Condition 4**	**Condition 5**
Subject 1	4	3	4	4	4
Subject 2	4	1	3	3	4
Subject 3	4	1	4	1	4
Subject 4	4	2	3	3	3
Subject 5	4	0	4	3	4
Subject 6	4	4	4	4	4
Subject 7	4	1	4	3	4
Mean ± Std	4.00 ± 0.00	1.71 ± 1.38	3.71 ± 0.49	3.00 ± 1.00	3.86 ± 0.38
***P* value**	0.317	**0.026**	0.317	0.059	NA

Condition 1 – without motion without vNav-SG; Condition 2 – with motion without vNav-SG; Condition 3 – with motion with vNav; Condition 4 – with motion with SG; Condition 5 – with motion with vNav-SG

Vessel wall sharpness deteriorated significantly when imaging subjects with motion but without any motion compensation strategy, as compared with that obtained in "With motion, with vNav-SG" scans (BA outer: 0.73 ± 0.24 vs. 0.94 ± 0.24, $P = 0.033$; BA inner: 0.49 ± 0.08 vs. 0.59 ± 0.20, $P = 0.026$; MCA outer: 0.85 ± 0.17 vs. 1.19 ± 0.84, $P = 0.027$; MCA inner: 0.48 ± 0.11 vs. 0.57 ± 0.14, $P < 0.001$) (Figure 3.4). The measurements in "With motion, with vNav-SG" scans were higher, although not significantly, than those in other motion correction scans with either vNav or SG, and were the closest to those obtained in "Without motion, without vNav-SG" scans (BA outer: 0.94 ± 0.24 vs. 0.96 ± 0.31, $P = 0.815$; BA inner: 0.59 ± 0.20 vs. 0.62 ± 0.22, $P = 0.481$; MCA outer: 1.19 ± 0.84 vs. 1.33 ± 0.56, $P = 0.367$; MCA inner: 0.57 ± 0.14 vs. 0.65 ± 0.27, $P = 0.275$).

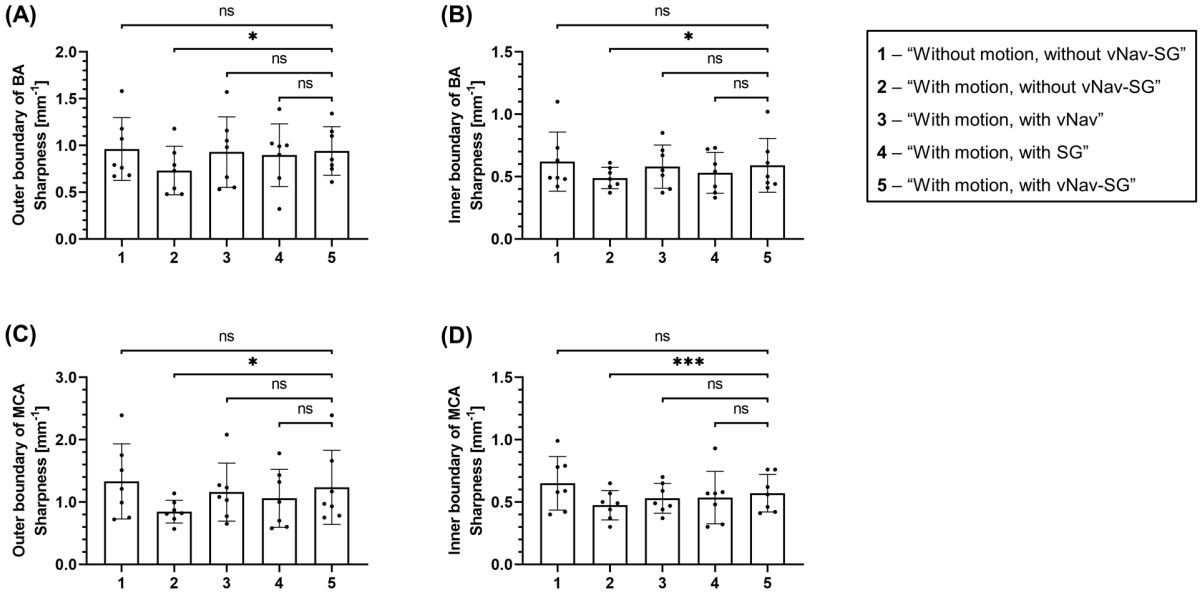

Figure 3.4 Bar graphs showing the mean values and standard deviations of the outer and inner vessel wall boundary of the basilar artery (BA) (A,B) and middle cerebral artery (MCA) (C,D), respectively, with regard to the five imaging conditions. The sharpness measurement results obtained from the "With motion, with vNav-SG" scan were compared to those obtained from the other four imaging conditions. The *P* values were calculated based on a paired two-tailed Student's t-test and are marked on the top of each bar graph. Comparable vessel wall sharpness results were obtained in the "Without motion, without vNav- SG" group and those scans with either the vNav or SG approach or both. Adoption of the proposed vNav-SG strategy ("With motion, with vNav-SG") led to the best vessel wall sharpness compared to the other two scenarios ("With motion, with vNav" and "With motion, with SG"). The significant difference between "With motion, without vNav-SG" and "With motion, with vNav-SG" scans illustrate the effectiveness of vNav-SG approach in mitigating motion artifacts when imaging subjects with motion. Abbreviation: ns, not significant

Figure 3.5 shows the imaging results from a representative patient with ischemic stroke (Figure 3.5A) caused by intra-aneurysmal thrombosis at the left MCA (arrow on Figure 3.5B). A mild stenosis caused by atherosclerotic plaque was found in the left VA (arrowhead on Figure 3.5B). During the intracranial VWI session, the patient could not hold his head and neck still for the entire 8 min. Therefore, the conventional SPACE

images suffered from severe motion artifacts, i.e. blurry aneurysm (Figure 3.5C) and nondiagnostic vessel wall boundary (Figure 3.5D). By contrast, the proposed vNav-SG technique dramatically improved image quality and the lesions were much better depicted. Notice that in Figure 3.5E, the aneurysm was better delineated, and wall thickening as well as contrast enhancement were detected in Figure 3.5F.

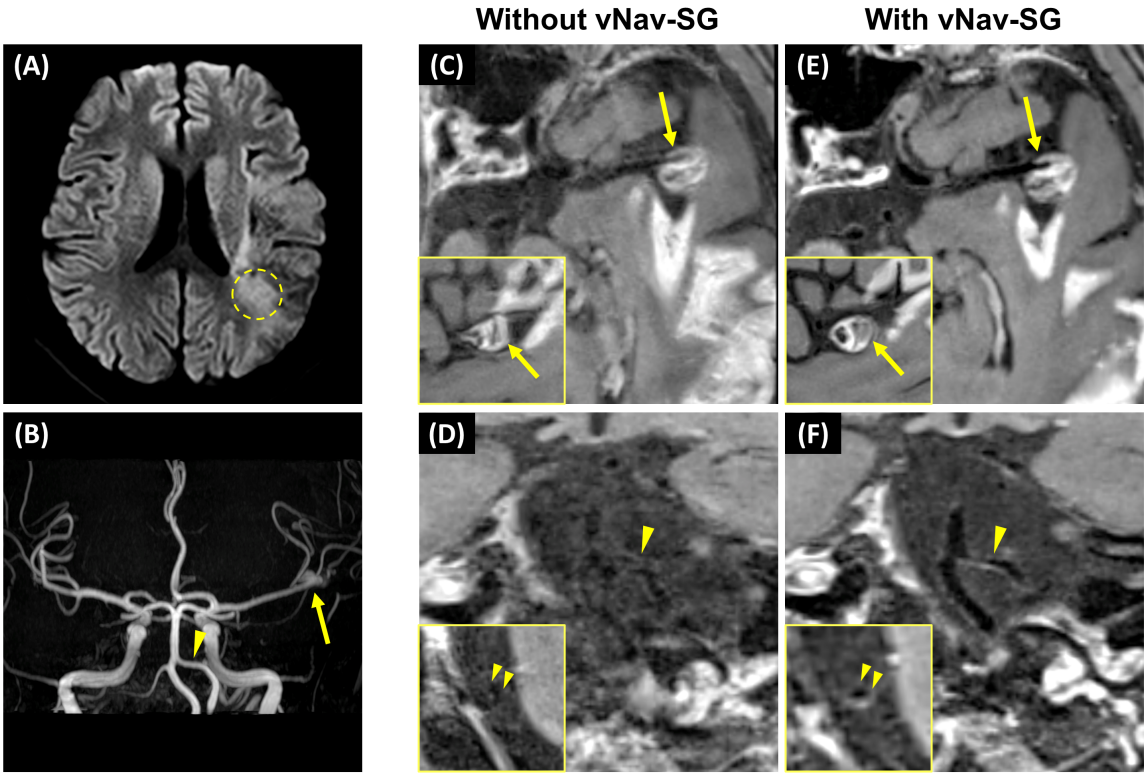

Figure 3.5 A, In a 62-year-old male patient with ischemic stroke caused by intra-aneurysmal thrombosis, an infarct marked out by the dashed circle was detected on the DWI image during clinical evaluation. B, On time-of-flight MR angiography, an aneurysm (arrow) and atherosclerotic plaque (arrowhead) were detected on left MCA M1 segment and left vertebral artery (VA) V4 segment, respectively. During the evaluation of intracranial vessel wall imaging, the patient had difficulty holding his head and neck still for the entire 8 minutes. C,D, Therefore, 3D multiplanar reconstructions of postcontrast vessel wall imaging and the cross-sectional view of the left MCA M1 segment and the left VA V4 segment showed that the images were corrupted by severe

intrascan motion. E, With the proposed vNav-SG strategy, the aneurysm was better delineated, and the wall thickening as well as contrast enhancement were detected

3.4 DISCUSSION

To our knowledge, this is the first report of technical development work addressing motion coinciding with MR intracranial VWI. Motion is a common reason for image corruption in neuroanatomical MR imaging. Intracranial 3D VWI is particularly susceptible due to the required high spatial resolutions and relatively long scan times. In a recent healthy volunteer study, motion artifacts were observed in 17.6% of imaging subjects[67]. A population-based study reported a failure rate of 9.9% due to motion-related poor image quality[68]. Therefore, although underexplored to date, motion susceptibility could critically undermine VWI's clinical translation.

In intracranial VWI, motion artifacts may arise from either bulk head motion or localized movement of internal anatomic structures[74]. Compensation for bulk motion in brain imaging has been investigated extensively through either hardware-based[79,80] or software-based approaches[81–83]. Hardware-based techniques (i.e., camera systems) are compatible with a broad range of sequences and track rigid motions precisely. However, these approaches have been restricted to compensation for rigid bulk motion. Software-based approaches are more cost-effective as they require only the standard MR system. The vNav approach fits easily in the SPACE readouts and has proved successful in brain imaging[75]. However, like hardware-based approaches, it has the drawback that the effects of internal localized movements on image quality in intracranial VWI are not considered. Given the fact that some intracranial vessel segments are located close to

the nasal sinuses and oral cavity, the localized motions, caused by swallowing and coughing, may affect the quality of intracranial VWI to some extent. Software approaches have previously been shown to be effective in compensating for these motion sources in extracranial VWI[65,84]. We therefore sought to perform a systematic investigation of motion effects and propose a technique capable of simultaneously addressing bulk head motion and localized motion.

We first demonstrated that localized movement can significantly impair vessel wall delineation. The SG technique, when specifically targeted to the nasal sinus and oral cavity, demonstrated promise in detecting motion and significantly mitigating image degradation. By combining vNav and SG strategies, we then demonstrated that each component of this combined strategy contributes to restored image quality. Compared with regular SPACE imaging, the proposed vNav-SG SPACE technique provided acceptable overall image quality and vessel wall sharpness in the presence of subject motion.

The developed vNav-SG technique integrated previously published vNav and SG approaches with several technical modifications. First, instead of utilizing the signal from the k-space center point[84], the SG signal in our method came from the center k-space line that was in turn transformed to a projection of the whole 3D volume, which is intuitively more sensitive to translation or distortion. Second, the motion-contaminated TRs detected by SG were reacquired at the end of the scan instead of being reacquired immediately[65]. All TRs were ordered in a priority queue based on their CC values. Once all TRs had been executed, the sequence began reacquiring TRs according to their priority. The number of reacquisitions was pre-defined by the operator at the scanner console,

ensuring a fixed total scan time despite potentially compromised image quality in the case of excessive patient movement. Third, in this work, intra-TR motion was monitored by the SG lines, and this replaced the reacquisition by “motion score” used in the original vNav approach[75]. Moreover, previous methods compensate for either localized or bulk head motion only, whereas our method allows for simultaneous compensation of bulk and localized movements, which is the major innovation and contribution.

There are some limitations in this work. First, the instructed motion at certain preset intervals is not guaranteed to be identical across all conditions and subjects. Such inconsistency could have biased the comparison of images between different imaging conditions. Second, the reacquisition scheme entails a time penalty, and consequently a trade-off between scan efficiency and overall image quality. A shorter reacquisition period may lead to more motion-contaminated data being retained and contributing to the online reconstruction, thus degrading the final image quality.

3.5 CONCLUSION

We have shown that localized movement can induce substantial artifacts in intracranial VWI, and mitigation with the SG approach is feasible. Moreover, the combined vNav-SG strategy has demonstrated the potential to effectively mitigate motion artifacts caused by both bulk head motion and localized movement in healthy subjects and patients. Therefore, the developed vNav-SG SPACE sequence may substantially improve the robustness of intracranial VWI in clinical settings and ensure accurate assessment of vessel wall pathologies. The work presented in this chapter was published in “Hu, Z., et al. (2021). *Magnetic Resonance in Medicine*, 86(2), 637-647.”

CHAPTER 4

Accelerated 3D MR Intracranial Vessel Wall Imaging: Development and Validation of a Cascaded Multi-scale Wavelet with Iterative Refinement Reconstruction Network

4.1 INTRODUCTION

MR VWI is a non-invasive, “looking-beyond-the-lumen” imaging modality that can directly visualize and characterize arterial wall lesions involved in various intracranial vasculopathies[11,85]. 3D variable-flip-angle TSE has become the most popular acquisition method for intracranial MR VWI[86]. However, the requirements for large spatial coverage and high spatial resolution necessitate a prohibitively long acquisition time (i.e., 6-12 min) per scan. When both pre- and post-contrast scans are needed, for example in atherosclerotic plaque imaging, an MR VWI protocol can take at least 15 minutes[87]. This lengthy protocol may elicit some practical issues, such as low throughput, poor patient tolerance, motion-induced image quality degradation, and even complete scan failure.

Strategies have been proposed to speed up MR VWI[62,63,88,89]. In general, acceleration is achieved by reconstructing images from sub-Nyquist k-space sampling leveraging either physical properties of multi-coil acquisition, sparsity of MR images, or a mixture of both. For example, parallel imaging (PI) takes advantage of multi-coil spatial sensitivities to reduce time-consuming phase-encoding steps for fast MR imaging[90–92].

Unlike PI, compressed sensing (CS) exploits image sparsity as prior knowledge to reconstruct MR images[93]. With the recent advances in computational power, there have been great interests in applying deep learning methods, in particular convolutional neural networks (CNN), to reduce acquisition time in a wide variety of MR applications[94–98]. CNN-based approaches can outperform PI or CS in terms of reconstruction quality and speed[99,100]. However, there are few studies applying CNN to intracranial MR VWI. Eun et al. recently proposed UNet-based neural networks to enhance the overall image quality of proton density-weighted intracranial vessel wall images reconstructed by CS algorithms[101]. Zhou et al. developed a CNN-based point spread function enhancement approach to retrospectively improve the quality of accelerated T1-weighted MR VWI[102]. Nonetheless, both methods were image domain-based, and thus ignored the prior information of the acquired data in k-space.

In this chapter, we develope a deep learning-based reconstruction framework named CAscaded Multi-scale WAvelet with iterative REfinement network (CAMWARE) for accelerated intracranial MR VWI. CAMWARE is implemented in a cascading fashion, alternating between CNN modules that remove artifacts in the image domain and data consistency (DC) modules that enforce data fidelity in k-space. Furthermore, to achieve more accurate wall delineation with sharper boundaries, we incorporate discrete wavelet transform to preserve high-frequency details and iterative multi-scale refinement (iMR) blocks to exploit multi-scale features effectively. Validated on ischemic stroke patients with intracranial atherosclerosis, CAMWARE can achieve 0.55-mm-resolution whole-brain 3D MR VWI, either pre- or post-contrast, within 4 minutes while providing image

quality and plaque delineation comparable to those available from a 2× PI scan (i.e., 12 min in this work).

4.2 METHODS

4.2.1 CAMWARE architecture

Overall cascading design

Similar to the deep cascaded network developed by Schlemper et al.[98], the proposed CAMWARE consists of two identical subnetworks implemented in a cascade fashion, where the first subnetwork translates a zero-filling image to an artifact-free image and the second further boosts up accuracy of the previous reconstruction[103] (Figure 4.1A). Each subnetwork has two modules: a multi-scale wavelet CNN module with iterative refinement and a DC module. Both subnetworks' forward and backward propagations are well-defined, resulting in one large network that can be trained in an end-to-end manner[98].

Multi-scale wavelet CNN module with iterative refinement

A 2D UNet structure is adopted as the backbone network architecture of the proposed CNN module (Figure 4.1B). Conventional UNet employs downsampling and upsampling operations by directly altering spatial resolution of feature maps to enlarge receptive field[104]. At present, the most commonly used downsampling and upsampling methods are pooling and deconvolution, respectively, yet at the cost of high-frequency information loss. This is especially detrimental when restoring submillimeter-dimension vessel wall structures. In contrast, CAMWARE replaces pooling and deconvolution with discrete wavelet transform and corresponding inverse wavelet transform for downsampling and

upsampling operations, respectively[105]. Specifically, at each spatial scale, the four subband images (i.e., LL, LH, HL, and HH) generated by discrete wavelet transform are concatenated and fed into a convolutional block, which consists of three convolutional layers (convolution with 3 × 3 kernels [Conv 3 × 3] + rectified linear unit [ReLU]). Correspondingly, each scale subband images are reconstructed by completely mirrored operations via inverse wavelet transform. In addition, iMR blocks are introduced to achieve more accurate wall delineation with sharper boundaries. The proposed iMR block comprises of three units as shown in Figure 4.1C[106]. First, the input adaptive convolution unit consists of two convolutional layers (Conv 3 × 3 + ReLU) for input adaptation to generate feature maps of the same feature dimension. Second, the multi-scale fusion unit fuses all path inputs into low-level feature maps by upsampling the smaller feature maps. Last, the output adaptive convolution unit is another two convolution layers that perform non-linear operations prior to final prediction. A 1 × 1 convolution is applied on the last scale to generate the fused outputs.

Data consistency module

CAMWARE inserts a DC module after each of the aforementioned CNN module to enforce data fidelity (Figure 4.1D). First, predictions of the previous CNN module are taken as inputs and Fourier transformed to yield k-space information. The data consistency operation updates the k-space with the original acquisition value if the specific location is sampled; otherwise, the predicted value will be used. The updated k-space signals are back-transformed to the image domain, which are then fed into the next module or output as final predictions.

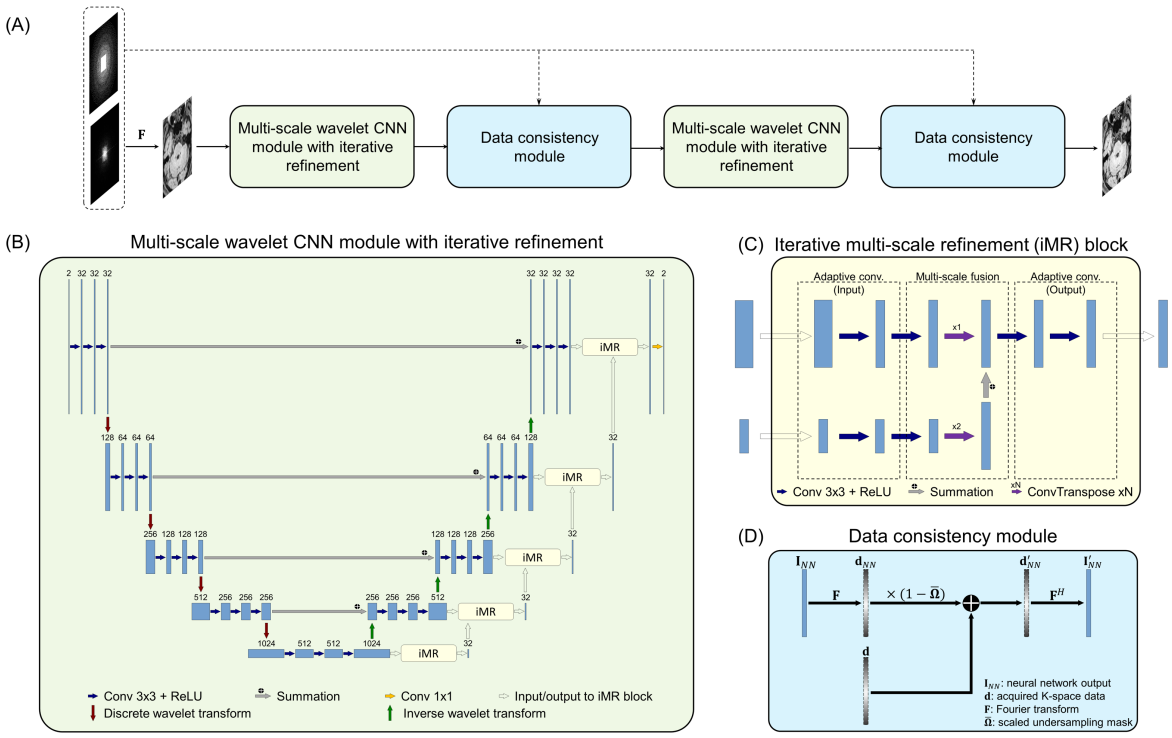

Figure 4.1 Illustration of the proposed neural network architecture. (A) Overall cascading design. Two identical subnetworks, each consists of a convolutional neural network (CNN) module and a data consistency (DC) module, are cascaded in a sequentially manner to form a large network. 2D transverse undersampled k-space data and variable density Poisson-disk undersampling mask are taken as inputs. (B-C) Multi-scale wavelet CNN module with iterative refinement. A 2D U-Net architecture is taken as the backbone with pooling and deconvolution replaced by discrete wavelet transform and inverse wavelet transform for downsampling and upsampling, respectively. Iterative multi-scale refinement (iMR) blocks, which comprises of an input adaptive convolution unit, a multi-scale fusion unit and an output adaptive convolutional unit, are introduced at different scales before generating the final prediction. The number of channels for each convolutional layer is annotated on top. (D) DC module. The DC module updates the k-space with the originally acquired value if the specific location is sampled prospectively

4.2.2 Study population and data acquisition

Forty-three subjects, including 13 healthy volunteers (aged 23-58 years, 7 females) and 30 patients (aged 34-76 years, 17 females) with ischemic strokes and clinical diagnosis

of intracranial atherosclerosis were recruited with approval of the local institutional review board. All subjects underwent a pre-contrast whole-brain MR VWI scan, and 26 of the 30 patients underwent an additional post-contrast scan, using a 3-T clinical MR system (MAGNETOM Skyra; Siemens Healthcare, Erlangen, Germany) equipped with a standard 20-channel head-neck coil. A previously developed whole-brain MR VWI sequence parameter setting was used with the following adaptations[63,77]. The FOV was enlarged to 248 × 230 × 132 mm^3 (matrix size: 448 × 414 × 224, resolution: 0.55-mm isotropic) to reduce wrap-around artifacts. PI in phase-encoding direction with a GRAPPA acceleration factor of 2 was used, resulting in a scan time of 12 minutes. Detailed imaging parameters are summarized in Table 4.1.

Table 4.1 List of sequence parameters

Imaging parameters	
Field-of-view [mm^3]	248 × 230 × 132
Acquisition dimension	3D
Matrix size	448 × 414 × 224
Spatial resolution [mm^3]	0.55 isotropic
Bandwidth [Hz/pixel]	446
TR [ms]	900
TE [ms]	15
Number of slices	224
Slice oversampling	7.1 %
Echo train length	52
Parallel imaging	GRAPPA 2× along phase encoding direction
Scan duration	12:10 min

4.2.3 Experiments

All acquired MR datasets were reconstructed offline with matrix size zero-filled to 512 × 512 × 256 to generate complex-valued images (referred to as “target 2× PI” hereafter). The image intensities were normalized, per subject, to have a maximum magnitude of 1. Extreme superior and inferior slices with low SNR were excluded for further processing, resulting in 350 transverse slices available for each dataset. In addition, data augmentation including random rotation of [-10°, 10°] and horizontal flip by 50% of chance was applied on a per-slice basis to counter overfitting. A vendor-implemented variable density Poisson-disc undersampling mask (autocalibration signal lines: 30) was applied to the k-space regenerated by Fourier transforming the target 2× PI images to simulate

undersampled k-space data. The acceleration factor of the undersampling mask was empirically selected to be 6.5 according to Figure 4.2, equivalent to those obtained by a 4-minute prospective acquisition.

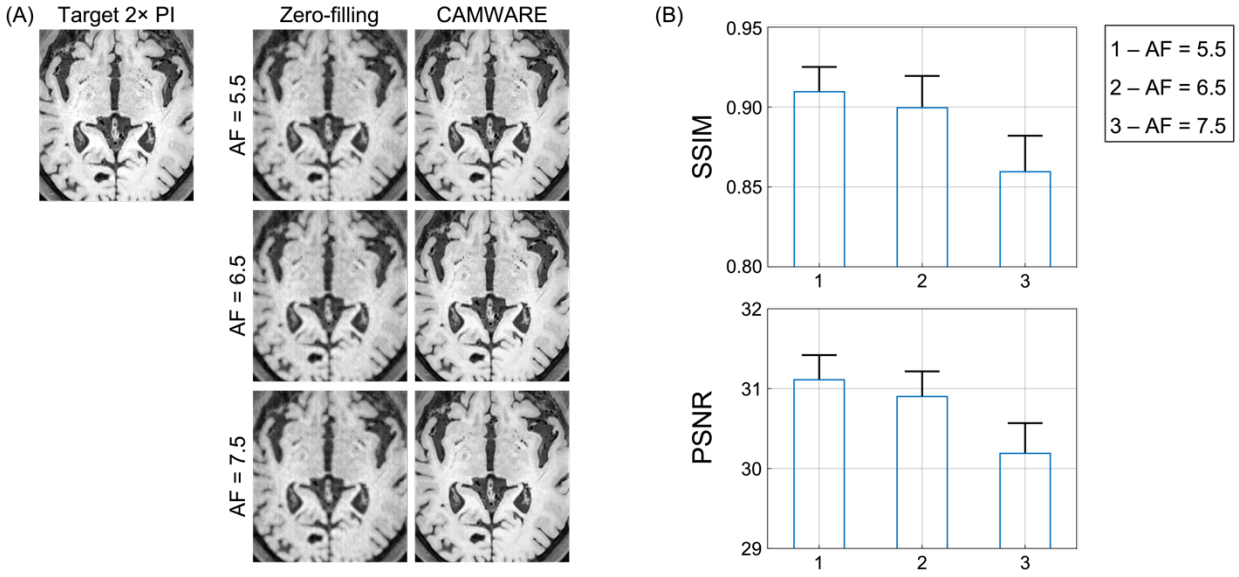

Figure 4.2 Results demonstrating effects of different acceleration factors (AF) on CAMWARE outputs. (A) CAMWARE predictions of a representative slice and corresponding zero-filling images at multiple AFs (5.5, 6.5, and 7.5). The same slice acquired by 2× PI is also provided to serve as the reference. (B) Structural similarity index (SSIM) and peak signal-to-noise ratio (PSNR) metrics between the CAMWARE predictions and corresponding target 2× PI at different AFs. As demonstrated by SSIM and PSNR values, CAMWARE can achieve mean SSIM equals to 0.90 and mean PSNR around 31 at AF = 6.5. When further increase to AF = 7.5, both SSIM and PSNR values drop drastically compared to AF = 5.5 and 6.5, and some fine structures are missing on the output image. Therefore, we decided to adopt AF = 6.5 for intracranial MR VWI, which is equivalent to a 4-minute prospective acquisition

We randomly selected 6 patient datasets, including 4 pre-contrast and 2 post-contrast datasets, from a total of 69 datasets for network performance evaluation (referred to as “testing set” hereafter, 2100 slices). The remaining 63 datasets were split into 57 datasets for training (19950 slices) and 6 for validation (2100 slices). CAMWARE takes the 2D transverse undersampled k-space data and the undersampling mask as inputs,

and outputs the images with the image quality comparable to that obtained by a 12-min 2× PI scan. The real and imaginary parts of the complex values were concatenated as 2 separate channels within the proposed CNN modules.

During the neural network training process, network weights were initialized using He initialization[107]. The loss function was a combination of structural similarity index (SSIM) loss and mean absolute error (MAE) loss:

$$L_{total} = \lambda_{\mathrm{SSIM}} L_{\mathrm{SSIM}} + \lambda_{\mathrm{MAE}} L_{\mathrm{MAE}} \quad (4.1)$$

where the weighting parameters λ_{SSIM} and λ_{MAE} were empirically selected as λ_{SSIM} = λ_{MAE} = 0.5 to achieve a good balance between the perceptual quality and element-wise accuracy of the predicted images. ADAM optimizer was adopted to minimize the loss function displayed in Equation 4.1 with a fixed learning rate of 0.0001[108]. The network was trained for 100 epochs with a minibatch size of 4. The network was implemented using the Keras package running Tensorflow computing backend[109] and was trained from scratch on a 64-bit Ubuntu Linux system equipped with Nvidia Geforce RTX 3090 graphic cards.

4.2.4 Performance evaluation

All following performance evaluations were conducted on the testing set.

Comparison to other reconstruction methods

The performance of CAMWARE was compared to several reconstruction methods for accelerated MR imaging: (a) zero-filling reconstruction; (b) CS reconstruction; (c) the state-of-the-art deep neural network-based reconstruction (i.e., variational network). The CS reconstruction was implemented using the projection onto convex sets algorithm, which reconstructed images iteratively by repeating soft-thresholding in the wavelet-

transform domain and data consistency in k-space until stopping criteria were met[110]. The variational network was adapted based on a Tensorflow implementation shared by the original developers[95]. Reconstruction performance of each method was evaluated by SSIM and peak signal-to-noise ratio (PSNR).

Quality of vessel wall delineation

Quality of vessel wall delineation, which is specific to the MR VWI application, was evaluated with a commonly used quantitative metric – vessel wall sharpness. Comparison of vessel wall sharpness was performed between the CAMWARE predictions and the corresponding 2× PI. Specifically, sharpness was measured at the inner and outer boundaries of two major intracranial vessel segments, including middle cerebral artery and basilar artery. For each vessel segment, three contiguous 2D cross-sectional slices of 0.55-mm thickness were reformatted. Sharpness was measured at three evenly distributed locations in each slice, with the first chosen at the most blurred position of the vessel wall boundary. The sharpness of each segment was then estimated by averaging across the nine selected locations. All measurements were performed based on a previously developed method[111] using an in-lab MATLAB (R2021a; MathWorks, Natick, MA) program.

Quality of atherosclerotic plaque delineation

As a preliminary assessment of clinical performance, the quality of atherosclerotic plaque delineation was evaluated and compared between the CAMWARE predictions and 2× PI. In addition, considering the proposed CNN module takes the zero-filling images transformed from the undersampled k-space as inputs, we also compared the CAMWARE predictions with zero-filling images to show the improvements on plaque

delineations attributed to CAMWARE. Specifically, plaques (characterized as vessel wall thickening) were first identified on the target images by a neuroradiologist with 7 years of experience in intracranial MR VWI. For qualitative evaluation, the three image sets were randomized and graded by the blinded neuroradiologist for the delineation quality of plaques based on a 4-point scale: 0-poor, 1-fair, 2-good, 3-excellent. For quantitative evaluation, plaque-wall contrast ratio (CR), defined as the signal intensity ratio between the brightest region within the plaque and the reference normal vessel wall, was calculated for each plaque.

4.2.5 Statistical analysis

Statistical analyses were performed using GraphPad Prism (version 8.0.2; GraphPad Software, San Diego, CA). Differences among reconstruction methods were evaluated using paired two-tailed Student's t-tests. ICCs and Bland-Altman plots were used to assess the sharpness measurement agreement between CAMWARE predictions and the target 2× PI. Paired two-tailed Wilcoxon signed-rank tests were used for the comparisons of plaque delineation scores and plaque-wall CRs between CAMWARE predictions and counterparts. A *P*-value < 0.05 was considered to indicate statistical significance.

4.3 RESULTS

The total time for CAMWARE training was about 28 hours. The average time for reconstructing a 3D intracranial MR VWI set with the trained network was ~5.25 seconds.

4.3.1 Ablation studies

To demonstrate every incorporated element of CAMWARE contributes to improving image quality and reconstruction accuracy in MR VWI, ablation studies were first performed. Specifically, in addition to CAMWARE, several neural networks were trained from scratch using the same setup described in Section 4.2.3, including: (a) UNet, (b) UNet with iMR blocks (iMR-UNet), (c) multi-scale wavelet UNet with iMR blocks (iMR-MWUNet); (d) multi-scale wavelet UNet with iMR blocks and a DC module (iMR-MWUNet + DC). The UNet architecture was adapted from a Keras-based implementation (https://github.com/sohiniroych/Unet-using-TF2), and MWCNN was implemented based on the source codes provided by the original developers (https://github.com/lpj-github-io/MWCNNv2). Quantitative metrics, including SSIM and PSNR, were calculated for each slice between the prediction of each neural network and the corresponding target 2× PI image for performance evaluation.

Figure 4.3 shows representative transverse vessel wall images reconstructed by different neural networks in the ablation studies. Corresponding error maps at the same scale are also provided to help compare reconstruction performances qualitatively. Starting from vanilla UNet, in order from left to right, one element was added to the model (in this case the order of addition is iMR blocks, multi-scale wavelet transform, the DC module and the cascading structure), resulting in gradually improved image quality and reconstruction accuracy. CAMWARE, taking advantage of all these elements, achieved the best reconstruction results comparable to the target 2× PI.

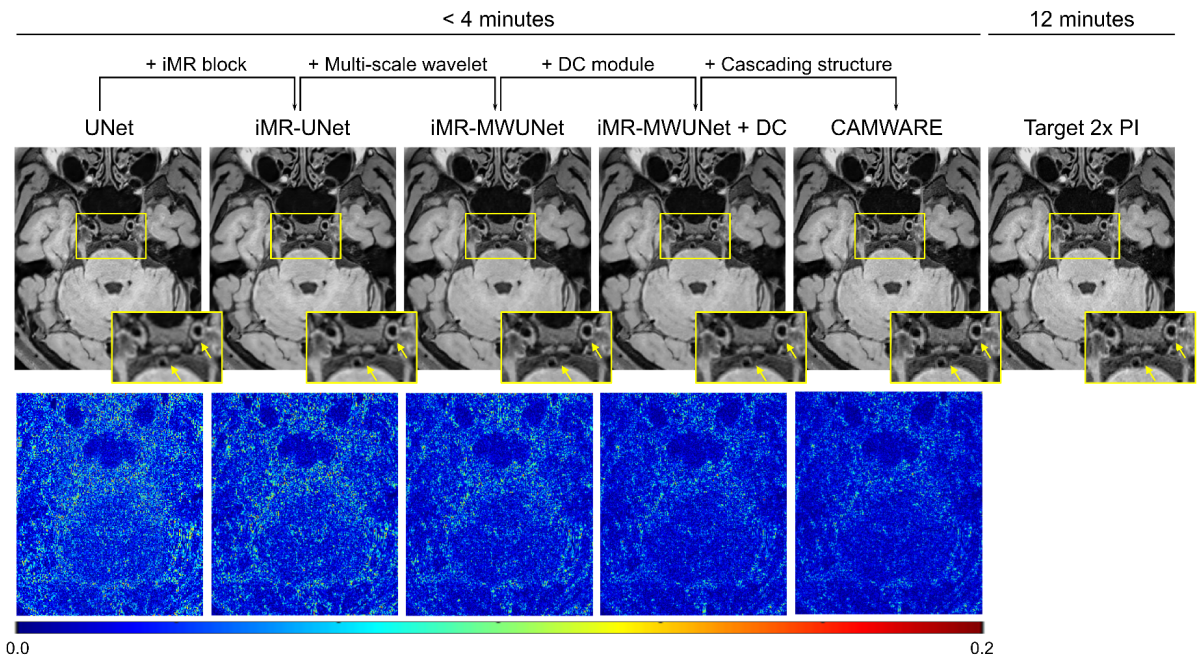

Figure 4.3 Comparison of representative intracranial MR VWI images in the transverse orientation reconstructed by different neural networks (< 4 min) in the ablation studies as well as the target 2× PI (12 min) (top row). Starting from vanilla UNet, step-by-step additions to the model are shown on top. Corresponding error maps at the same scale are also provided (bottom row). Cross-sectional views of the basilar artery and internal carotid arteries are zoomed-in (pointed out by the yellow arrows) for detailed demonstration. Overall, CAMWARE, taking advantage of all added elements, yields a more accurate reconstruction comparable to the target 2x PI

4.3.2 Comparison to other reconstruction methods

Figure 4.4 shows representative MR VWI images generated by different reconstruction methods. Corresponding error maps against the target 2× PI are also provided to help compare reconstruction performances qualitatively. Deep neural network-based methods yielded more natural images and sharper structure delineation than zero-filling and CS reconstructions, with CAMWARE outperforming variational network as indicated by the error maps.

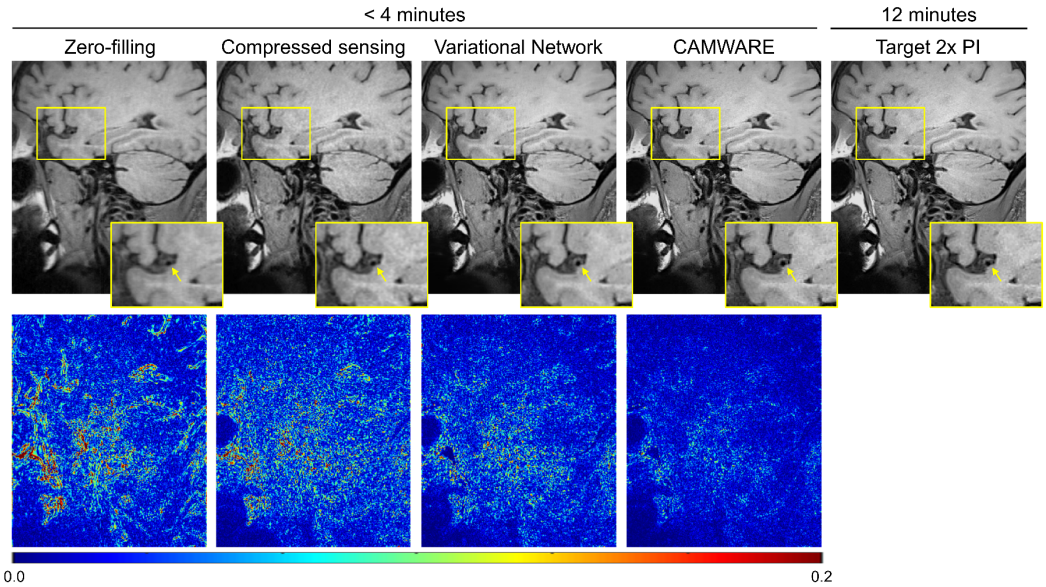

Figure 4.4 Comparison of representative intracranial MR VWI images in the sagittal orientation generated by different reconstruction methods, including zero-filling reconstruction, compressed sensing reconstruction and variational network (< 4 min), and the target 2× PI (12 min) (top row), as well as corresponding error maps (bottom row). Cross-sectional views of the middle cerebral artery are zoomed-in (pointed out by the yellow arrows) for detailed demonstration. Although implemented based on a 2D network backbone, the capability of CAMWARE in reconstructing high-quality MR VWI images are preserved when reformatting the image sets into sagittal slices

Furthermore, even though the training and evaluation processes were performed on individual transverse slices, the capability of CAMWARE in producing high-quality images was preserved when reformatting the reconstructed image sets into sagittal slices. Figure 4.5 illustrates the SSIM and PSNR between images reconstructed by different methods and the corresponding target 2× PI. CAMWARE achieved SSIM and PSNR of 0.91 ± 0.02 and 31.89 ± 2.53, respectively, which were significantly higher than other reconstruction methods ($P < 0.001$).

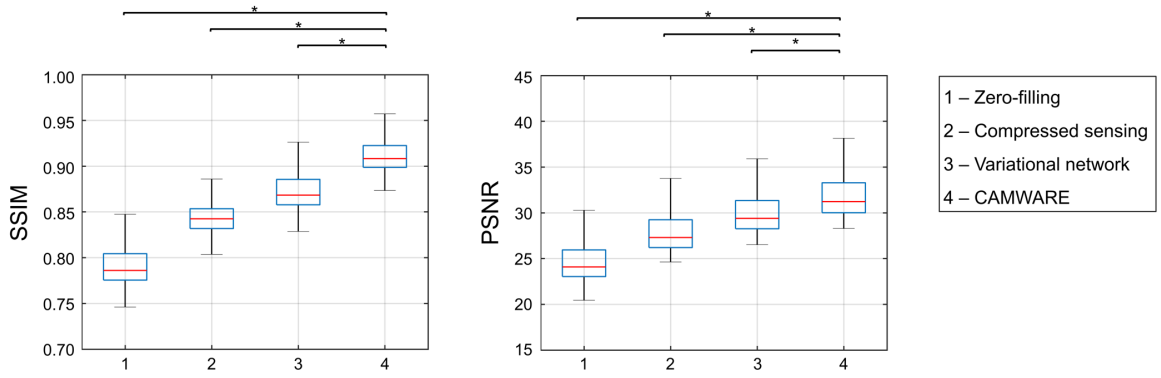

Figure 4.5 Box plots showing the comparisons of quantitative metrics, including structural similarity index (SSIM) and peak signal-to-noise ratio (PSNR), among the proposed CAMWARE and other reconstruction methods from 6 randomly selected ischemic stroke patients for network evaluation. The SSIM and PSNR values achieved by CAMWARE are significantly higher than other reconstruction methods

4.3.3 Quality of vessel wall delineation

Excellent agreement in sharpness measurements was observed between the CAMWARE predictions and the corresponding target 2× PI. The ICCs of vessel wall sharpness were 0.94 and 0.80 at inner and outer boundaries of middle cerebral artery, respectively, and 0.98 and 0.94 at inner and outer boundaries of basilar artery, respectively. Figure 4.6 shows the Bland-Altman plots for sharpness measurements at inner and outer boundaries of middle cerebral and basilar arteries, respectively. The mean differences were less than ±5.5% with limits of agreement all within ±20% after taking the mean differences into account.

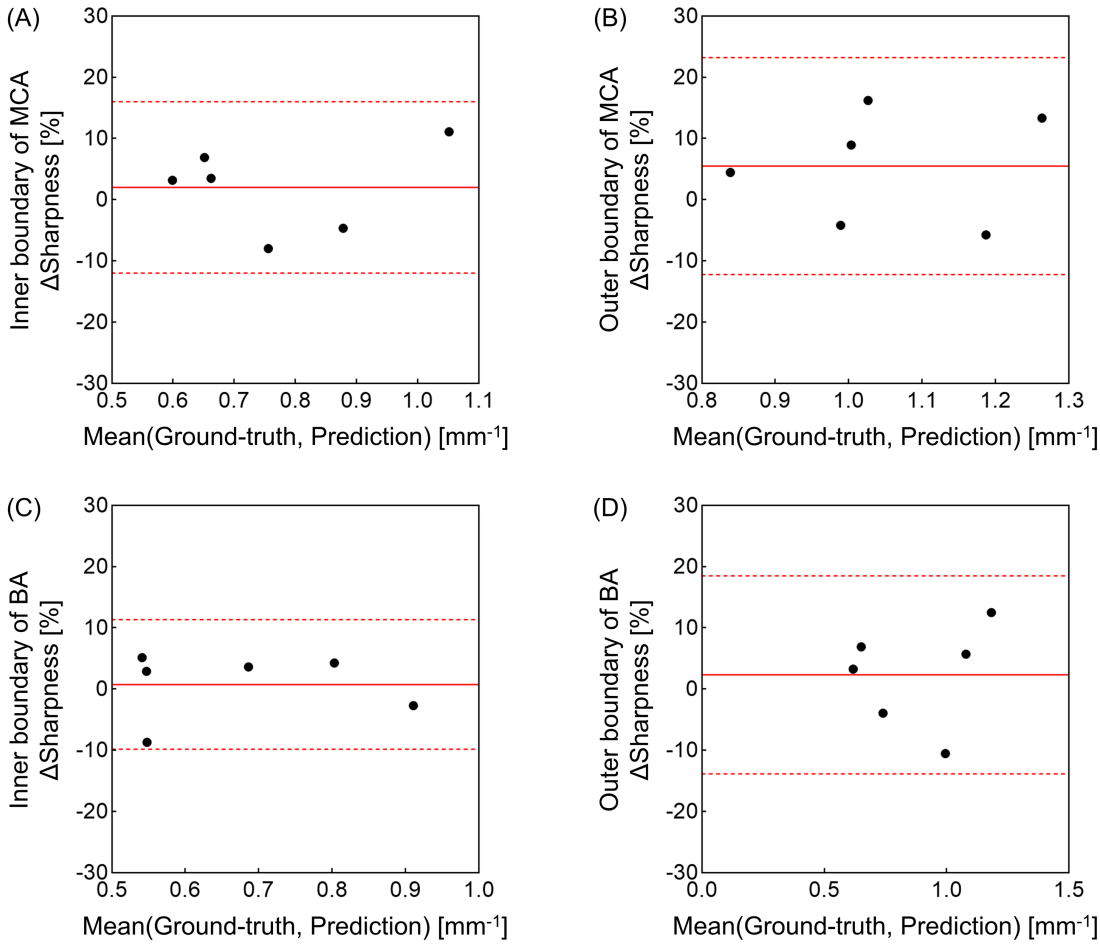

Figure 4.6 The Bland-Altman analyses for agreements of sharpness measurements at the inner and outer boundaries of middle cerebral artery (MCA) and basilar artery (BA) using the CAMWARE predictions and the corresponding ground-truth

4.3.4 Quality of atherosclerotic plaque delineation

Figure 4.7 displays zero-filling images, CAMWARE predictions and the target 2× PI in 2 representative patients. In comparison to zero-filling reconstruction, CAMWARE provided sharper delineation with higher SNR of atherosclerotic plaques. Signal intensity-based plaque features, such as pre-contrast hyper-intensity (Figure 4.7A) and post-contrast wall

enhancement (Figure 4.7B) were depicted comparably by CAMWARE with respect to the 2× PI images.

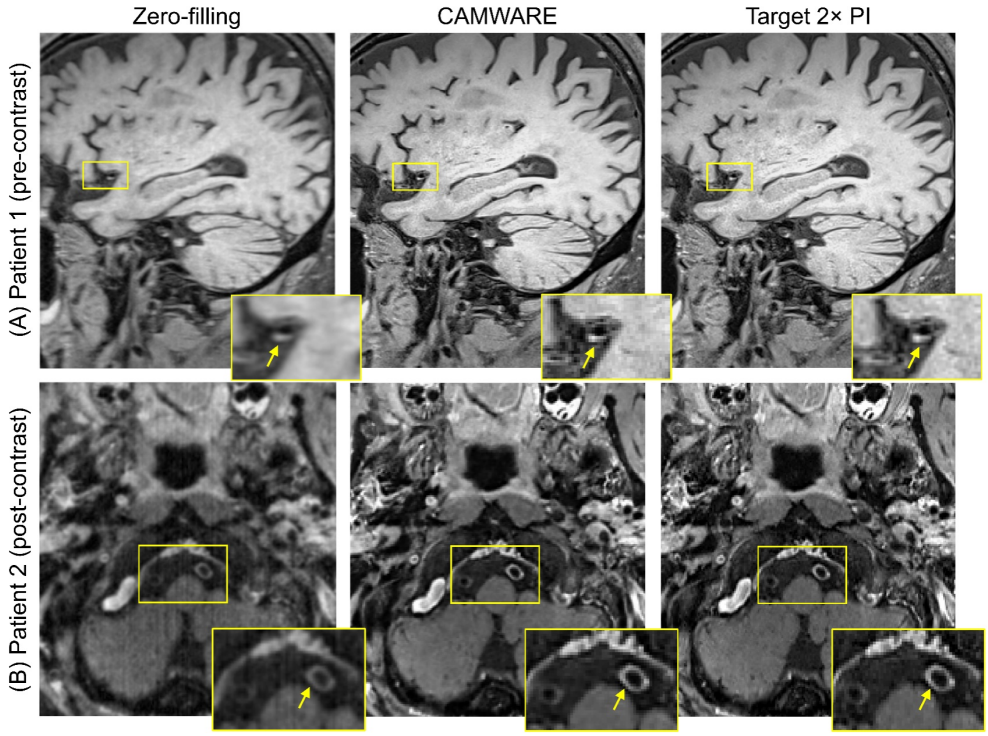

Figure 4.7 Comparison of zero-filling reconstructed images (< 4 min), CAMWARE predictions (< 4 min) and the corresponding target 2× PI (12 min) on two representative ischemic stroke patients. The proposed CAMWARE reconstructed images with better-preserved sharpness and textures compared to the zero-filling images. In addition, (A) the pre-contrast hyper-intense plaque on the middle cerebral artery and (B) the post-contrast wall enhancement on the vertebral artery are comparably well-depicted on the CAMWARE predictions with respect to the target 2× PI

From the testing set, 10 plaques were identified and underwent numerical assessments. The quality scores of plaque delineation on the CAMWARE predictions were significantly higher than those on the zero-filling images (2.70 ± 0.46 vs 0.60 ± 0.49, $P < 0.001$), and were comparable to those on the target 2× PI images (2.70 ± 0.46 vs 2.90 ± 0.30, $P = 0.17$) (Figure 4.8A). CRs measured on the CAMWARE predictions exhibited similar performance when compared to those measured on the 2× PI images

(1.89 ± 0.45 vs 1.88 ± 0.45, $P = 0.42$), but were significantly different from those measured on the zero-filling images (1.89 ± 0.45 vs 1.73 ± 0.30, $P = 0.03$) (Figure 4.8B).

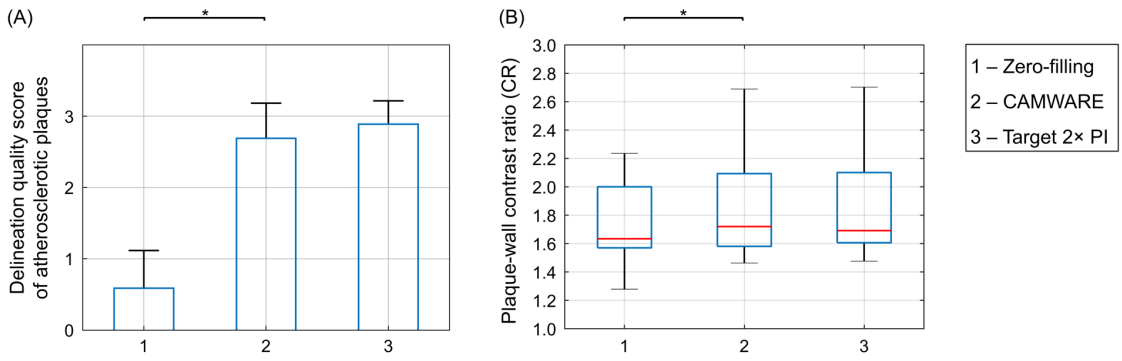

Figure 4.8 Assessments of (A) plaque delineation quality score and (B) plaque-wall contrast ratios (CR) based on the 10 atherosclerotic plaques identified by a neuroradiologist. The quality of plaque delineation on the CAMWARE predictions is significantly improved over that on the zero-filling images and is comparable to that on the corresponding target 2× PI. In terms of wall-plaque CRs, no significant difference was found between the CAMWARE predictions and the 2× PI images

4.4 DISCUSSION

3D MR VWI is emerging as a highly useful diagnostic imaging modality for neurovascular diseases[85]. However, its long acquisition time is a major hurdle to widespread clinical adoption. In this study, we developed a deep neural network-based reconstruction framework, CAMWARE, and validated its clinical performance against 2× PI, which is the current gold-standard approach for MR VWI, on ischemic stroke patients. With the proposed CAMWARE, we achieved 0.55-mm-resolution whole-brain 3D MR VWI scan within 4 min while providing image quality equivalent to that obtained by a 12-min 2× PI scan. This will allow for complete intracranial MR VWI investigation, including both pre-

and post-contrast scans, within 10 min. To the best of our knowledge, this is the first report of using deep learning for reconstructing intracranial MR VWI images from substantially undersampled k-space data.

CAMWARE cascades two identical subnetworks sequentially to build one large network which is end-to-end trainable, with the latter subnetwork acting as an extra step to reduce reconstruction errors of the former one. Each subnetwork consists of a CNN module followed by a DC module, similar to the previously proposed deep cascaded network[98]. The CNN module is implemented based on a 2D UNet backbone. To ensure a decent network performance on restoring fine vessel wall structures, we modified UNet in two aspects: (a) discrete wavelet transform was adopted as the downsampling and upsampling operations, respectively, to enlarge receptive field and alter resolution of feature maps without losing high-frequency details[105]; (b) iMR blocks were inserted before generating the final predictions to combine the representative information at multiple scales for reducing the loss of information along the image decoder. Both discrete wavelet transform and iMR have proved effective in other applications[105,106] and were introduced for the first time in this work to improve the performance of deep learning-driven MR VWI acceleration.

The proposed CAMWARE framework was evaluated on in vivo intracranial MR VWI datasets acquired from 6 ischemic stroke patients with clinical diagnosis of intracranial atherosclerosis. CAMWARE predictions were compared with conventional reconstruction approaches, such as zero-filling and CS, and state-of-the-art deep neural network reconstructions, such as variational network[95]. It was observed that CAMWARE outperformed all the aforementioned methods both qualitatively (overall image quality and

error maps) and quantitatively (SSIM and PSNR). Furthermore, sharpness measurements on intracranial vessel segments, as well as plaque assessment including delineation quality scores and plaque-wall CR quantifications, show that CAMWARE performed vessel wall and plaque delineation comparable to the target 2× PI acquired with a 12-min protocol.

It is important to note that in the experiments presented the feasibility of CAMWARE was demonstrated on datasets produced by retrospective undersampling of back transformed complex-valued images, which is equivalent to single-coil data. Although it would be more practical to apply CAMWARE on multi-coil data, the current results validated that CAMWARE owns the capability to reduce scan time of MR VWI and generate images comparable to 2× PI. In future, more experiments are necessary to figure out ways to efficiently leverage the correlation of phased arrays to further improve the performance of CAMWARE.

There are several limitations to this study. First, variable density Poisson-disc undersampling mask was applied to the k-space data Fourier transformed from images acquired with 2× PI to create voxel-wise aligned image pairs. It would be ideal to perform retrospective undersampling from the fully-sampled k-space data; however, considering the long acquisition time for high-resolution MR VWI, it's impractical for the patients to hold still for a fully-sampled scan (about 24 min). Second, the CS images were reconstructed by projection onto convex sets algorithm, which is not a commonly adopted CS reconstruction algorithm. However, since the undersampled k-space data were generated by Fourier transformation of coil-combined complex-valued images, the coil sensitivity information of multiple phased arrays was not available. Thus, the well-

established CS algorithms (i.e., ESPIRiT[112]) were inappropriate in this scenario. Last, the assessment was only performed in the testing set containing 6 ischemic stroke patient datasets. A systematic clinical study is warranted to further assess the feasibility of the proposed approach.

4.5 CONCLUSION

In this work, we developed a deep neural network-based reconstruction framework named CAMWARE that holds the potential to enable whole-brain intracranial MR VWI with 0.55-mm isotropic resolution within 4 min. Our study on ischemic stroke patients demonstrates that CAMWARE can preserve vessel wall structures and sharpness and ensure accurate assessment of vessel wall plaques in agreement with 2× PI.

CHAPTER 5

MR Multitasking-based Multidimensional Assessment of Cardiovascular System – Part I: Development and Feasibility Study on the Thoracic Aorta

5.1 INTRODUCTION

Thoracic aortic diseases are one of the most common causes of cardiovascular morbidity and mortality, and could end in potentially calamitous consequences[113,114]. For example, vulnerable atherosclerotic plaques at the aortic arch are considered a major embolic source for ischemic stroke[115], and aortic aneurysms increase the risk of aortic wall rupture and internal bleeding. Unfortunately, patients with aortic diseases usually have no signs or symptoms and are unaware of the pathological changes in their aortas before adverse events occur[116]. Thus, diagnosis and follow-up of aortic abnormalities depend exclusively on diagnostic imaging[117].

Several imaging modalities are traditionally used for thoracic aortic disease assessment in clinical practice. TEE provides high-quality imaging of the thoracic aorta because of the use of high-frequency transducers and the close proximity of the esophagus to the aorta[114]. However, this modality is invasive and introduces considerable discomfort to patients, and not all parts of the thoracic aorta can be visualized due to a limited FOV[118]. CT angiography is currently the most widely used diagnostic modality due

to its near universal availability and rapid acquisition[119,120]. However, CT angiography focuses on the detection of luminal abnormalities, while providing limited information on pathological changes within the aortic vessel wall[121]. In addition, CT angiography may be contraindicated in certain populations due to the concerns about exposure to ionizing radiation or allergic reaction to iodinated contrast material[122]. MR has emerged as a radiation-free, noninvasive imaging modality for diagnosing thoracic aortic diseases[120]. The most common MR approach is MR angiography, which can be achieved by exploiting either contrast-enhanced[5,6] or non-contrast (i.e., time-of-flight and steady-state free precession)[7–9] technologies. However, as another type of lumenography-based imaging modality, MR angiography shares with CT angiography the same limitation in lumen-only imaging.

The clinical potential of MR for the assessment of thoracic aortic diseases is being advanced with continued technical developments over the last decade. MR VWI, primarily based on the dark-blood contrast weighting, has been proposed as a useful tool for directly evaluating vessel wall characteristics (i.e., thickened, remodeled, or inflammatory status)[123,124]. More recently, MR VWI evolved from single, dark-blood contrast to multicontrast approaches to facilitate the characterization of vulnerable atherosclerotic plaque components or to provide a more comprehensive disease assessment. Several recently developed 3D techniques tailored to thoracic aorta acquire different image contrasts through separate scans[121,125]. MR cine imaging is another technique proposed for evaluating aortic wall functions such as vessel compliance. Abnormal compliance (or strain index) has been shown to be implicated in pathogenesis of aortic aneurysm and dissection[126,127]. Despite the prominent features and clinical necessities, adoption of a

comprehensive protocol is hindered by three typical limitations: (a) long acquisition time associated with the need for large spatial coverage and high spatial resolution, (b) image misregistration due to subject motion among multiple scans, and (c) nontrivial imaging setup and sacrifice of efficiency for addressing motion during data acquisition, such as ECG triggering and respiratory navigator gating or breath-holding, which is a particular problem for patients with cardiac arrhythmias or difficulty in holding their breath.

MR multitasking is a recently proposed imaging framework that can address several longstanding problems in cardiovascular MRI[55]. Instead of applying conventional motion-compensation strategies, which constrain data acquisition periodically in a predefined time window to minimize physiological motion and ensure a specific contrast weighting, MR multitasking allows continuous data acquisition and retrospectively resolves different dynamics (i.e., physiological motion and physical relaxation), making it possible to acquire multiple co-registered images in one single scan with no reliance on triggering signals. Furthermore, by adopting a low-rank tensor image model, which exploits the high correlation between images at different time points, MR multitasking bypasses the “curse of dimensionality” and thereby allows expedited acquisitions[55,128].

Because of the crucial role that imaging plays in the diagnosis of thoracic aortic diseases and longstanding challenges of conventional imaging modalities, in this chapter we develop an MR multitasking-based 3D multidimensional assessment of cardiovascular system (MT-MACS) technique for comprehensive thoracic aortic vessel imaging. Without the use of ECG and respiratory navigators, this technique allows for motion-resolved, isotropic high spatial resolution, multidimensional (multiple contrast weightings and cine images) imaging of the thoracic aorta within 6 min. Technical

feasibility was demonstrated in healthy volunteers and patients with thoracic aortic diseases.

5.2 METHODS

5.2.1 Multidimensional imaging based on MR multitasking

The proposed MT-MACS method uses a low-rank tensor image model with a cardiac time dimension for phase-resolved cine imaging, and a T2-prepared inversion recovery dimension for multicontrast (i.e., bright-blood [BB], dark-blood [DB], and gray-blood [GB]) assessment. Specifically, MT-MACS models a 6-dimensional aortic image as a 4-way multidimensional array (or "tensor") $\mathcal{I}$, with one dimension indexing 3D spatial location $\mathbf{x}$ and three time dimensions: cardiac motion t_{c}, respiration t_{r}, and inversion recovery t_{T1}. The strong correlation between aortic images along and across time dimensions makes $\mathcal{I}$ a low-rank tensor, and therefore partially separable in the following sense[56]:

$$\mathcal{I}(\mathbf{x}, t_{\mathrm{c}}, t_{\mathrm{r}}, t_{\mathrm{T1}}) = \sum_{\ell=1}^{L} u_{\ell}(\mathbf{x}) \phi_{\ell}(t_{\mathrm{c}}, t_{\mathrm{r}}, t_{\mathrm{T1}}) \tag{5.1}$$

where $u_{\ell}(\mathbf{x})$ is the ℓth of L basis images, and $\phi_{\ell}(t_{\mathrm{c}}, t_{\mathrm{r}}, t_{\mathrm{T1}})$ is the ℓth of L temporal functions. Furthermore, in the low-rank tensor image model, each $\phi_{\ell}(t_{\mathrm{c}}, t_{\mathrm{r}}, t_{\mathrm{T1}})$ is itself low-rank and can be factorized using individual bases for each time dimension:

$$\phi_{\ell}(t_{\mathrm{c}}, t_{\mathrm{r}}, t_{\mathrm{T1}}) = \sum_{m=1}^{M} \sum_{n=1}^{N} \sum_{p=1}^{P} c_{\ell mnp} v_m(t_{\mathrm{c}}) w_n(t_{\mathrm{r}}) z_p(t_{\mathrm{T1}}) \tag{5.2}$$

where v, w, and z denote basis functions along the cardiac motion, respiration, and inversion-recovery dimensions, respectively; and $c_{\ell mnp}$ denotes elements of the core tensor $\mathcal{C}$. Thus, our image tensor $\mathcal{I}$ can be expressed in matrix form as:

$$\mathbf{I}_{(1)} = \mathbf{U}_{\mathbf{x}}\mathbf{C}_{(1)}(\mathbf{Z}_{t_{\mathrm{T1}}} \otimes \mathbf{W}_{t_{\mathrm{r}}} \otimes \mathbf{V}_{t_{\mathrm{c}}}) \tag{5.3}$$

where $\mathbf{I}_{(1)}$ denotes mode-1 unfolding of the tensor $\mathcal{I}$ into a matrix; the factor matrix $\mathbf{U}_{\mathbf{x}}$ contains basis images; $\mathbf{C}_{(1)}$ denotes the unfolded core tensor; $\mathbf{V}_{t_{\mathrm{c}}}$, $\mathbf{W}_{t_{\mathrm{r}}}$, and $\mathbf{Z}_{t_{\mathrm{T1}}}$ contain temporal basis functions for each time dimension; and the $\otimes$ operator denotes the Kronecker product[129]. Currently, there are various low-rank strategies available for reconstruction of the multidimensional arrays, either implicitly or explicitly[55,130–134]. MR multitasking, based on the description of previous works[55,128,135,136], uses a mixed strategy that reconstructs the image tensor by directly recovering each of its factor matrices. Basically, in this work, image reconstruction can be divided into five steps:

1. Generate ungated images, which are reconstructed using explicit low-rank matrix imaging with only one time dimension representing elapsed time[55,128], for image-based cardiac phase and respiratory position identification by means of a modified T1 recovery–aware k-means clustering approach[55], placing the corresponding images into 14 cardiac bins and 6 respiratory bins.
2. Predetermine the temporal basis functions in $\mathbf{Z}_{t_{\mathrm{T1}}}$ (along the inversion-recovery dimension) from a training dictionary of inversion-recovery signals with different T1, T2, and B1 inhomogeneity values, which is generated according to the Bloch equations ahead of time[55,136].
3. Apply small-scale low-rank tensor completion to recover missing elements from a frequently sampled subset of k-space (“auxiliary data”), which will be

undersampled because it is impossible to acquire every combination of cardiac phase, respiratory phase, and inversion-recovery time point:

$$\widehat{D}_{\mathrm{aux}} = \arg \min_{D_{\mathrm{aux}} \in \mathrm{range}(\mathbf{Z}_{t_{\mathrm{T1}}})} \|\mathbf{d}_{\mathrm{aux}} - \Omega(D_{\mathrm{aux}})\|_2^2 + \lambda \sum_{n=1}^{4} \left\|\mathbf{D}_{\mathrm{aux},(n)}\right\|_* \qquad (5.4)$$

where $\mathbf{d}_{\mathrm{aux}}$ is the collected auxiliary data; $\Omega(\cdot)$ represents the undersampling pattern of the auxiliary dataset; $\mathbf{D}_{\mathrm{aux},(n)}$ denotes the mode-n flattening of the completed auxiliary tensor; and $\|\cdot\|_*$ is the nuclear norm that promotes low-rankness of each unfolded matrix.

4. Truncate the high-order singular value decomposition of $\widehat{\mathbf{D}}_{\mathrm{aux},(1)}$ to recover $\mathcal{C}$ and the temporal basis functions along the cardiac and respiratory phase directions, namely, $\mathbf{V}_{t_{\mathrm{c}}}$ and $\mathbf{W}_{t_{\mathrm{r}}}$, respectively.
5. Solve the following optimization problem to reconstruct the spatial coefficients $\mathbf{U}_{\mathbf{x}}$:

$$\widehat{\mathbf{U}}_{\mathbf{x}} = \arg \min_{\mathbf{U}_{\mathbf{x}}} \left\|\mathbf{d} - \Omega[\mathbf{F}\mathbf{S}\mathbf{U}_{\mathbf{x}} \cdot \mathbf{C}_{(1)}(\mathbf{Z}_{t_{\mathrm{T1}}} \otimes \mathbf{W}_{t_{\mathrm{r}}} \otimes \mathbf{V}_{t_{\mathrm{c}}})^T]\right\|_2^2 + \lambda R(\mathbf{U}_{\mathbf{x}}) \qquad (5.5)$$

where $\mathbf{d}$ is the acquired imaging data; $\mathbf{F}$ denotes the Fourier transform; and $\mathbf{S}$ denotes the coil sensitivity maps. The regularization functional $R(\cdot)$ here is chosen as a spatial wavelet sparsity penalty, and λ is the parameter used to balance between wavelet sparsity and noise artifacts.

5.2.2 Pulse sequence design

The MT-MACS technique is implemented based on a prototype free-running fast low-angle shot (FLASH) Cartesian acquisition immediately following intermittent T2-inversion recovery (T2-IR) magnetization preparation (Figure 5.1). The T2-IR preparative module is used to leverage T1 and T2 variances to (a) maximize the contrast between the vessel

wall and blood, and (b) create multiple image contrasts[137,138]. After the FLASH readouts, a short gap of fixed duration allows T1 recovery toward thermal equilibrium. Both phase and partition encodings for the imaging data $\mathbf{d}$ are collected with randomized ordering according to a variable-density Gaussian distribution, to achieve incoherent undersampling of the k-space. The auxiliary data $\mathbf{d}_{\text{aux}}$ collected at the center k-space (k_y = k_z = 0) is interleaved with the imaging data every 9 readouts. This ensures an auxiliary data sampling interval of 40 ms, which is adequate for capturing our targeted dynamic processes without sacrificing total imaging data. Too infrequent collection of auxiliary data cannot capture the overlapping dynamic processes, whereas too frequent collection comes at the cost of fewer imaging data, which would lead to degradation of the final image quality.

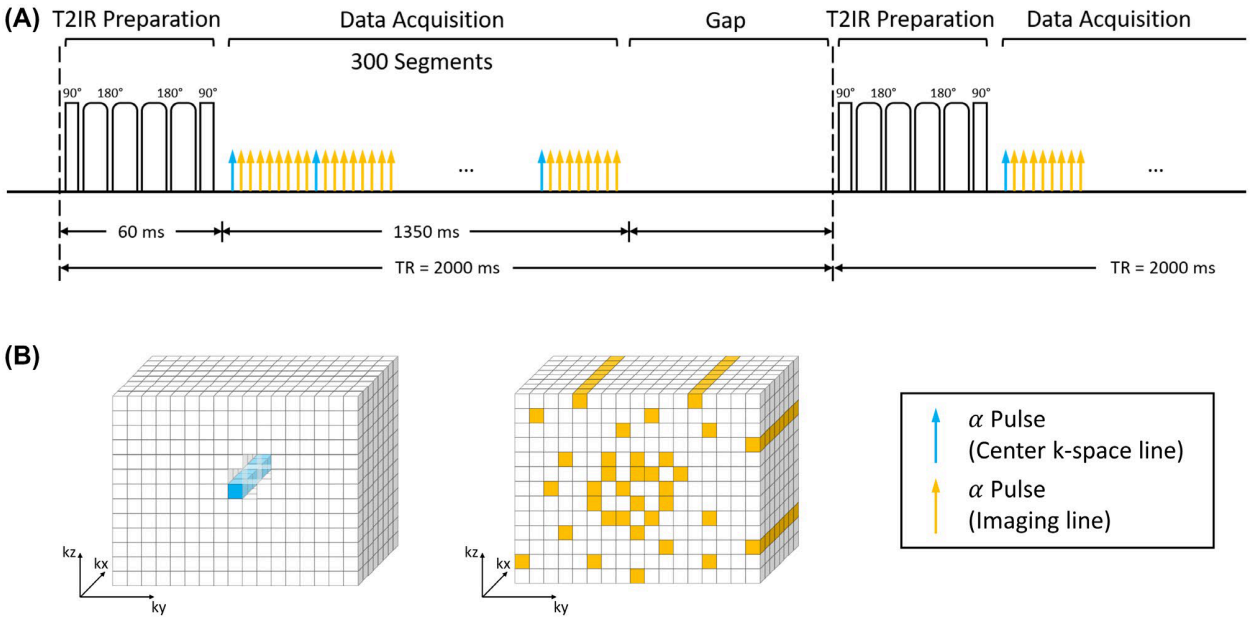

Figure 5.1 Pulse sequence diagram for the multitasking-based multidimensional assessment of cardiovascular system (MT-MACS) technique and corresponding k-space sampling pattern. A, Nonselective T2-preparation inversion-recovery (T2-IR) pulses are applied every TR, followed by continuous FLASH readout alpha pulses. One k-space line is collected every alpha pulse. After each blue arrow, an auxiliary line is acquired every 9 lines as the low-rank tensor subspace

training data. The data acquisition module containes 300 readout segments, followed by a short gap of fixed duration until the next T2-IR preparation pulse. B, Simplified illustration of k-space sampling strategy. The auxiliary data are collected at the k-space center. Cartesian sampling with randomized reordering with a variable-density Gaussian distribution in k_y and k_z directions is adopted in this sequence

5.2.3 Numerical simulations

To maximize the lumen-wall contrast, a simulation study was performed to optimize two parameters: (a) TR, which is the time interval between two consecutive T2-IR preparation pulses, and (b) the number of readout segments within each TR. The simulation study was conducted in two steps. We first assumed readouts were continuous, acquired every 4.5 ms (a practically achievable echo spacing) throughout the entirety of each TR. The curve of lumen-wall contrast against various TRs (Figure 5.2A) illustrates that short TRs would not provide adequate signal contrast between the vessel wall and blood. Moreover, long TRs may not be SNR-efficient, as the magnetization will spend too much time in the steady state rather than near the desired image contrasts. Therefore, a 2000-ms TR was empirically chosen here (Figure 5.2B) as a compromise. With the TR fixed, Figure 5.2C illustrates the lumen-wall contrast against the number of segments in each TR. Too many segments leads to less contrast; however, too few segments leads to a longer gap, reducing data acquisition efficiency and potentially degrading final image quality for a fixed total scan time. Based on simulations and several pilot in vivo experiments, we used 300 readout segments (approximately 1400 ms) followed by a 600-ms gap within each TR (Figure 5.2D). For the simulation purpose, the segment for which the vessel wall signal reached the nulling point was selected for the BB contrast, and the time point when the signal of lumen blood reached the nulling point was chosen for the DB contrast. The

relevant imaging parameters used in simulations were T1 = 1412 ms and T2 = 50 ms for vessel wall, T1 = 1932 ms and T2 = 275 ms for lumen blood, flip angle = 8º, echo spacing = 4.5 ms, and duration of T2-IR preparation module = 60 ms.

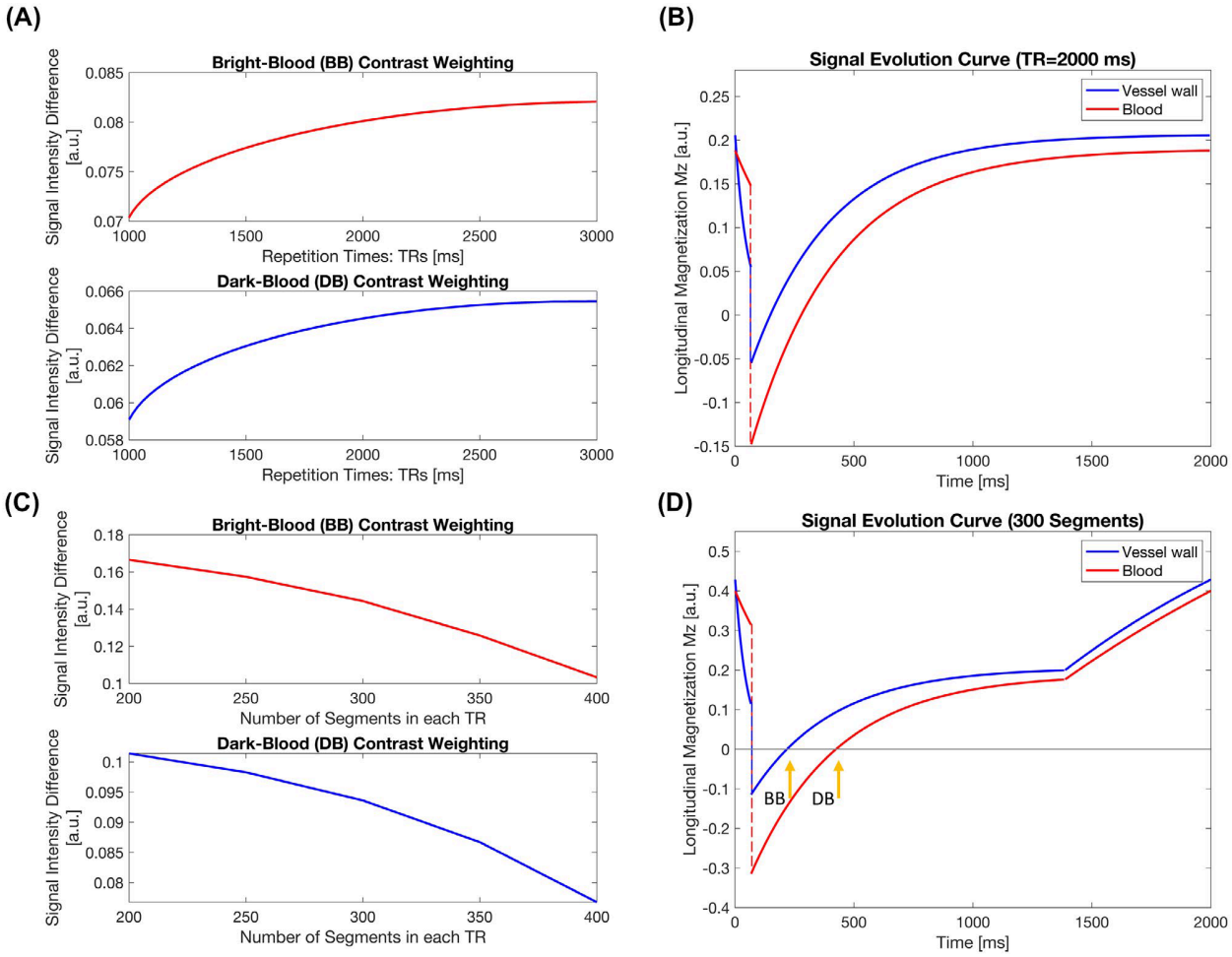

Figure 5.2 Simulation results. A, Curve of lumen-wall contrast with respect to bright-blood (BB) and dark-blood (DB) contrast weightings against various TRs with no gap until the next T2-IR-prepared pulse. B, Signal evolution curves of the aortic vessel wall and lumen blood with a 2000-ms TR. C, Curve of lumen-wall signal difference against numbers of segments during a single readout block with TR = 2000 ms. D, Signal evolution curves of the aortic vessel wall and lumen blood with 300 readout segments followed by a 600-ms gap until the next preparation pulse, under

the circumstance of TR = 2000 ms. Two representative time points were selected for BB and DB contrast weightings during the simulation study

5.2.4 In vivo study

The in vivo study was approved by the local institutional review board, and all subjects provided written informed consent before participation. Twelve healthy volunteers (aged 18-63 years, 7 females) and two patients (aged 38-71 years, 2 females) with aortic atherosclerosis and aortic aneurysm were recruited for the study. All imaging examinations were performed on a 3-T clinical MR scanner (MAGNETOM Skyra; Siemens Healthcare, Erlangen, Germany) with a standard 18-channel body coil and an integrated spine matrix coil.

In all healthy volunteers, MT-MACS imaging was performed with no ECG and respiratory navigator in an oblique sagittal orientation as determined using the three-point tool on localizer images. Major imaging parameters included FOV = 275 × 220 × 72 mm^3, matrix size = 200 × 160, number of slices = 52, spatial resolution = 1.38 mm isotropic, flip angle = 8º, TR/TE = 2000.0/2.1 ms, echo spacing = 4.5 ms, bandwidth = 1008 Hz/pixel, and 1-2-1 binomial-pulse spectrally selective water excitation for fat suppression. Imaging time was set for 10 minutes, and the acquired data later underwent offline reconstruction with different k-space raw data truncations corresponding to 4, 6, 8, and 10-minute scan durations for the goal of scan-time optimization. The MT-MACS imaging with 6-minute scan time (as optimized in the healthy volunteers) was performed on the 2 patients.

In addition, conventional sequences were also acquired in 9 of the 12 healthy subjects to serve as the references for morphological (i.e., lumen and wall area) and functional (i.e., strain index) quantification of the thoracic aorta. Briefly, 2D T1-weighted

DB vessel wall imaging based on double inversion recovery–prepared TSE sequence and 2D cine imaging based on the balanced SSFP sequence were performed at both the ascending and descending thoracic aorta, with ECG triggering and end-expiration breath holding. Major imaging parameters for 2D-TSE sequence included FOV = 350 × 285 mm^2, matrix size = 256 × 208, slice thickness = 5 mm, flip angle = 180º, TR = 1 cardiac cycle, TE = 27 ms, turbo factor = 12, echo spacing = 5.49 ms, bandwidth = 849 Hz/pixel, and ECG-triggered to the middiastole. Three contiguous slices were acquired with the purpose of reducing the measurement errors of vessel morphology induced by position-mismatch between the MT-MACS and 2D-TSE sequences. For 2D cine imaging, protocol parameters included FOV = 350 × 285 mm^2, matrix size = 256 × 208, slice thickness = 6 mm, flip angle = 50º, TR/TE = 45.9/2.5 ms, echo spacing = 3.3 ms, bandwidth = 962 Hz/pixel, and 25 phases based on retrospective gating.

5.2.5 Image analysis

Images acquired using the MT-MACS technique were reconstructed offline and generated in a DICOM format using MATLAB. These DICOM images were loaded to a workstation (LEONARDO, Siemens Healthcare) for the following analysis.

Qualitative analysis

For each healthy subject, four groups of multicontrast middiastolic end-expiratory images were reconstructed using different amounts of MT-MACS k-space raw data corresponding to 10, 8, 6, and 4-min long acquisitions, respectively. Three inversion-recovery time points were chosen to provide BB, DB, and GB image contrasts. All of the MT-MACS image sets were randomized and evaluated by 2 independent radiologists with at least 5 years of experience in cardiovascular imaging. Overall image quality was

graded using a 4-point scale: 0, poor: unidentifiable and completely blurred lumen and wall; 1, fair: identifiable but heavily blurred lumen and wall; 2, good: well-defined lumen and wall with slight artifacts; 3, excellent: excellent visualization and sharp vessel wall and lumen margins with no artifacts. The final image quality score was determined as an average between the 2 readers. Optimal scan time was determined as the shortest one that generated average scores of 2 or greater over all subjects for each image contrast.

Quantitative analysis

Quantitative analysis was performed on the MT-MACS images reconstructed using the data acquired within the scan time optimized previously. Contrast-to-noise ratio (CNR) of the vessel wall versus lumen blood was determined from all three image contrasts at the middiastolic end-expiratory phase using the following equation:

$$CNR = \frac{|SI_{LB} - SI_{VW}|}{\sigma_{BG}} \tag{5.6}$$

where SI_{LB} and SI_{VW} represent the mean signal intensity of the lumen blood and the vessel wall, respectively, within three regions of interest located at the ascending aorta, aortic arch, and descending aorta; and σ_{BG} is the standard deviation of signal intensities in a neighboring artifact-free air region.

For the accuracy analysis of lumen area (LA) and wall area (WA) measurements, the DB images of MT-MACS at the middiastolic end-expiratory phase were reformatted to match the 2D DB TSE images in both location and slice thickness. Inner and outer boundaries of the vessel wall on all cross-sectional slices acquired by each of the two sequences were manually traced by a radiologist. Based on these contours, the LA and WA of both the ascending aorta and descending aorta were measured. The mean LA and

WA values of each healthy subject were obtained by averaging the measurement results of the three contiguous slices.

For the accuracy analysis of the strain index measurement, cardiac phase-resolved BB images of MT-MACS were reconstructed and reformatted to match cine balanced SSFP images in both location and slice thickness. The strain index was measured for each of the two sequences using the following equation34:

$$Strain = \frac{(SA - DA)}{DA} \tag{5.7}$$

where SA is the maximal systolic LA and DA is the minimal diastolic LA of the aorta. The LA was determined after manually contouring the lumen by a radiologist.

5.2.6 Statistical analysis

Linear regression and ICCs were used to test measurement agreement in morphological and functional parameters between MT-MACS and corresponding 2D reference sequences. The extent of agreement was also determined using Bland-Altman analysis. A *P* value < 0.05 was considered to indicate statistical significance. All statistical analyses were performed using OriginPro (version 9.1; OriginLab, Northampton, MA).

5.3 RESULTS

The MT-MACS imaging was performed successfully on all 12 healthy subjects and 2 patients with thoracic aortic diseases. Figure 5.3 is the illustration of multiple time dimensions for the MT-MACS technique and some example images resulting from the multidimensional image reconstruction. Six respiratory phases lie along the respiratory

time axis (vertical); 14 cardiac phases lie along the cardiac time axis (depth); and 300 inversion-recovery segments lie along the T1 recovery time axis (horizontal). Three representative time points were picked out among the 300 segments for BB, DB and GB imaging, respectively.

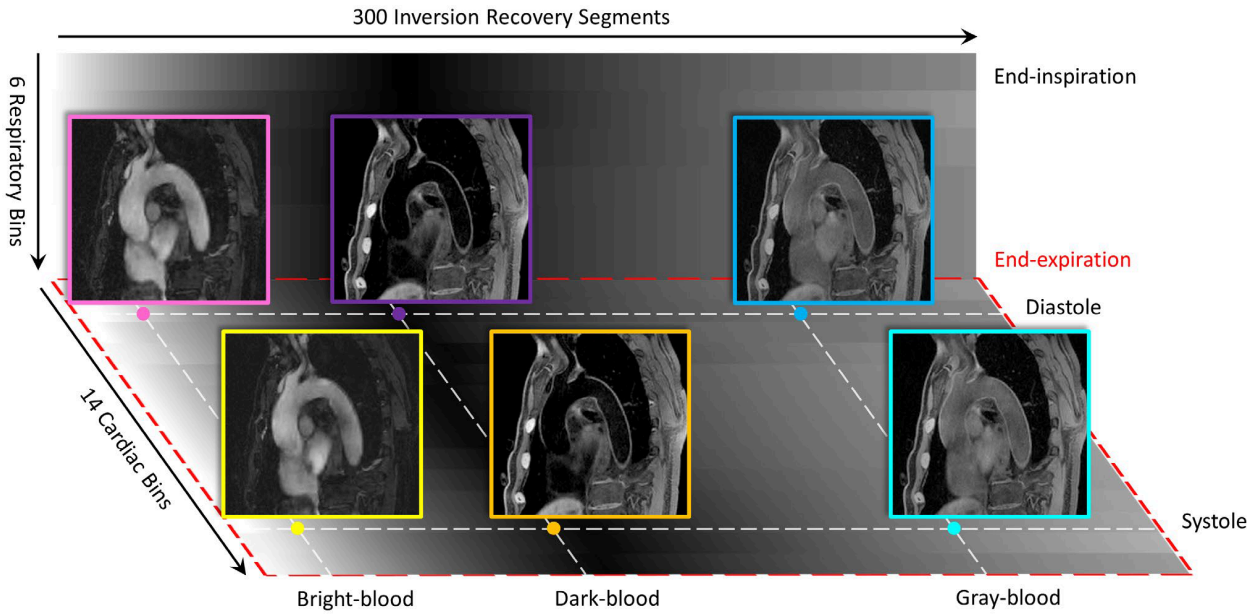

Figure 5.3 Illustration of different time dimensions for MT-MACS, namely, cardiac pulsation, respiration, and T2-IR dimensions. For phase-resolved imaging, MT-MACS divides cardiac motion and respiratory movement into 14 and 6 bins, respectively. Within each inversion-recovery period, MT-MACS contains 300 readout segments that can generate 300 various contrast weightings. Three typical contrast weightings (i.e., bright blood, dark blood, and gray blood) are selected for multicontrast assessment

5.3.1 Qualitative analysis

A total of 144 (3 image contrasts × 4 data amounts × 12 subjects) 3D image sets were scored for image quality. Figure 5.4 shows the average image-quality scores and corresponding standard deviations over all subjects for each image contrast within each scan-time category (Figure 5.4A) and representative images (Figure 5.4B).

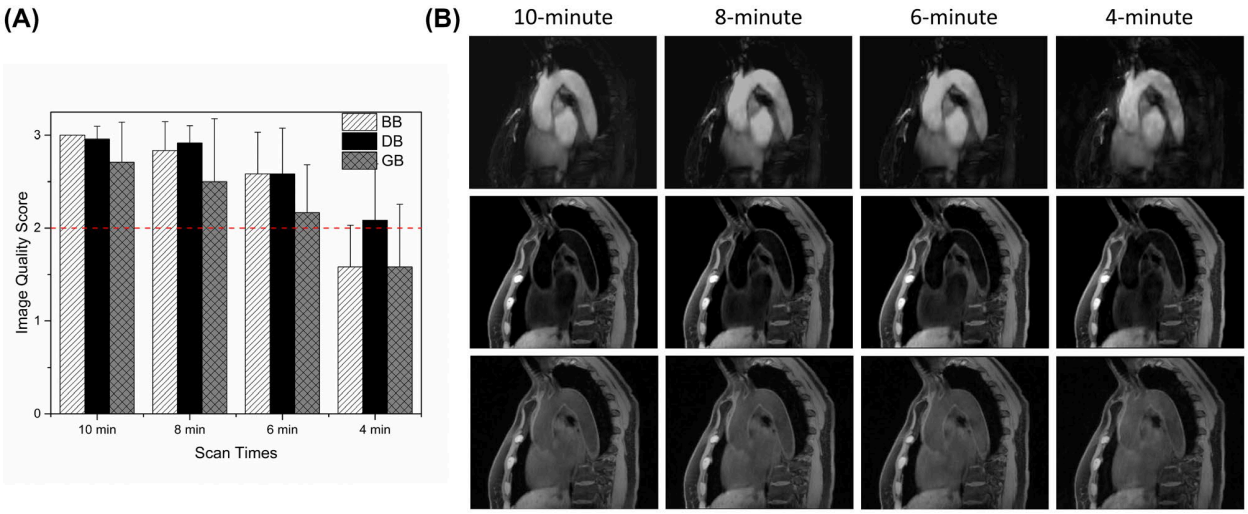

Figure 5.4 Qualitative analysis results. A, Average values of the overall image-quality scores given by two readers and the standard deviationss over all 12 subjects for each image contrast within each scan-time category. The optimal scan time was determined as the shortest one that generated average scores of 2 or greater (above the red dotted line) over all subjects for each image contrast above this level. For BB and GB images reconstructed using a 4-min data set, the average image-quality scores were less than 2, which were not enough for clinicians and radiologists to obtain clinically related information. B, One of the empirical studies illustrated the tradeoff between the overall image quality and scan time. Further reduction of the scan time to 4 min will lead to severe deterioration of the overall image quality. BB, bright-blood; DB, dark-blood; GB, gray-blood

For BB MT-MACS images, the image-quality scores for 10-min, 8-min, 6-min, and 4-min data sets were 3.00 ± 0.00, 2.83 ± 0.33, 2.58 ± 0.46, and 1.58 ± 0.46, respectively; for DB MT-MACS images, the image quality scores were 2.96 ± 0.14, 2.92 ± 0.19, 2.58 ± 0.50, and 2.08 ± 0.63, respectively; for MT-MACS GB images, the image-quality scores were 2.71 ± 0.45, 2.5 ± 0.71, 2.17 ± 0.53, and 1.58 ± 0.70, respectively. Scans in as short as 6 min provided good or excellent image quality with moderate to high interreader agreement quantified by weighted Cohen's kappa (κ) values 0.667 (P = .014), 1.000 (P < .001), and 0.739 (P < .001) for BB, DB and GB imaging, respectively (image-quality

scores given by both readers are shown in Figure 5.5). Thus, the 6-min image sets were chosen for the following quantitative analysis.

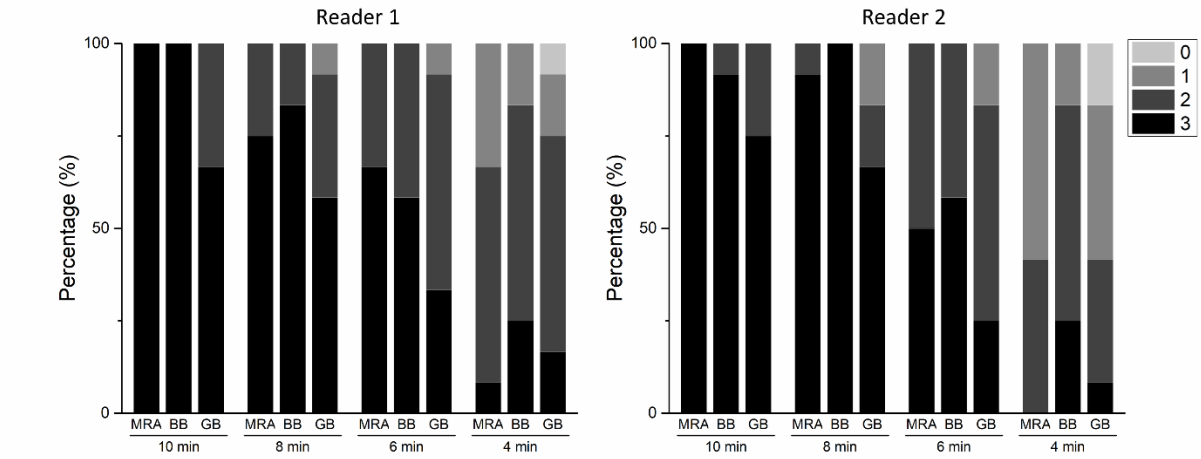

Figure 5.5 Distribution of the overall image quality scores for each image contrast within 4 scan time categories given by 2 raters (N = 12)

5.3.2 Quantitative analysis

The CNR measurements for BB, DB, and GB contrast weightings are 49.2 ± 12.8, 20.0 ± 5.8, and 2.8 ± 1.8, respectively, which are in line with the values published in the literature[123,139,140].

A comparison of measurements for several morphological parameters, including the LA and WA for both the ascending aorta and descending aorta, is shown in Figure 5.6A. In Figure 5.6B and 5.6D, linear regression analyses demonstrated excellent intraclass correlation between two imaging techniques (ICC = 0.993, $P < .001$ for LA; ICC = 0.969, $P < .001$ for WA), with slopes and ordinate intercepts of approximately one (range: 0.97 to 1.00) and zero (range: −0.08 to 0.00 cm2), respectively. According to Bland-Altman plots (Figure 5.6C and 5.6E), excellent agreements of both LA and WA measurement results were observed between MT-MACS and 2D DB TSE image sets.

For LA measurements, there was an absolute mean difference of 0.067 with 95% limits of agreement from −0.234 to 0.368 (N = 18 slices); for WA measurements, the absolute mean difference was 0.058 with 95% limits of agreement from −0.119 to 0.235 (N = 18 slices).

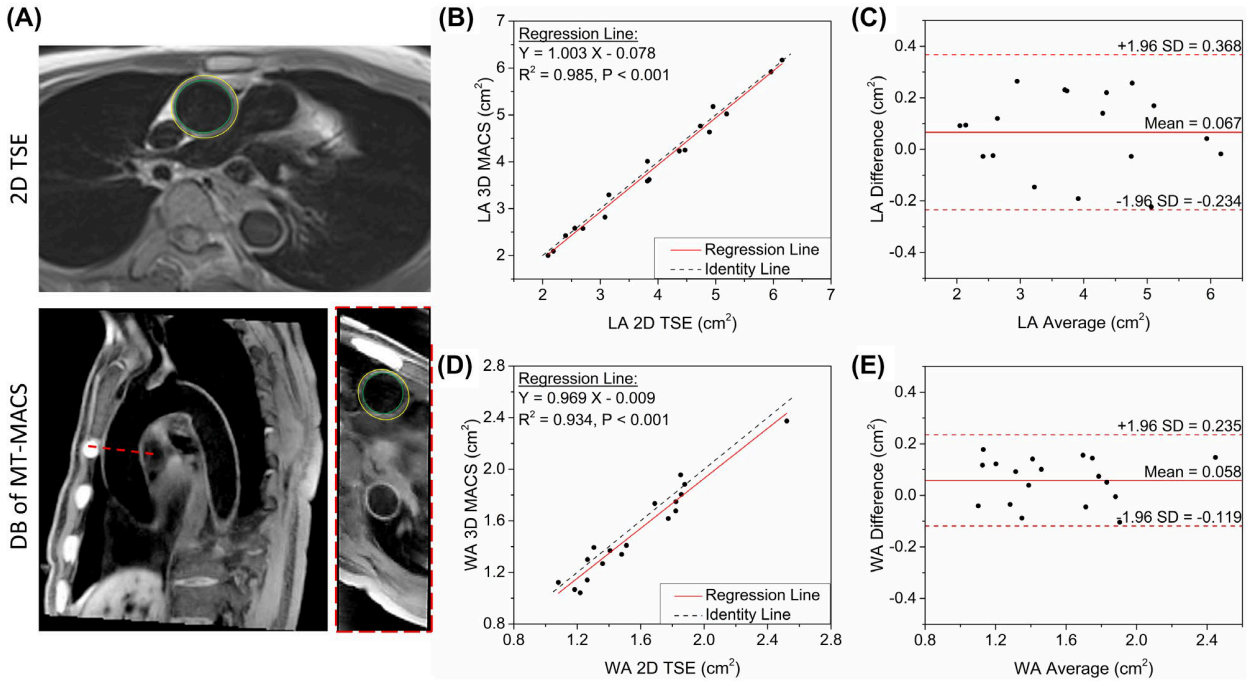

Figure 5.6 Quantification of morphological parameters of aortic vessels. A, Graphic illustration of measuring the lumen area (LA) and wall area (WA) in healthy subjects. The inner and outer contours were manually traced on both 2D turbo spin-echo (TSE) images and DB images of MT-MACS. Both the slice position and slice thickness were matched during the measurements. B,D, Comparison of LA and WA measurement, respectively, using the proposed MT-MACS and a convention 2D-TSE reference. Black dotted lines represent the identity line (Y = X), whereas solid red lines represent regression of the results from these two methods. The intraclass correlation coefficients for LA and WA measurements were 0.993 (P < .001) and 0.969 (P < .001), respectively. C,E, Bland-Altman plots comparing measurement results acquired by these two imaging techniques. Solid red lines and dashed red lines indicate the means and SDs of LA and WA values between the different methods

Comparison of aortic vessel strain index measurements between MT-MACS and 2D cine balanced SSFP is displayed in Figure 5.7. Good agreement was observed

between these two techniques (mean: 3.1%; 95% limits of agreement: −5.0% to 11.1%; N = 18 slices). The regression analysis illustrated a good linear relation (R2 = 0.890, *P* < .001) and correlation (ICC = 0.947, *P* < .001) between measurements.

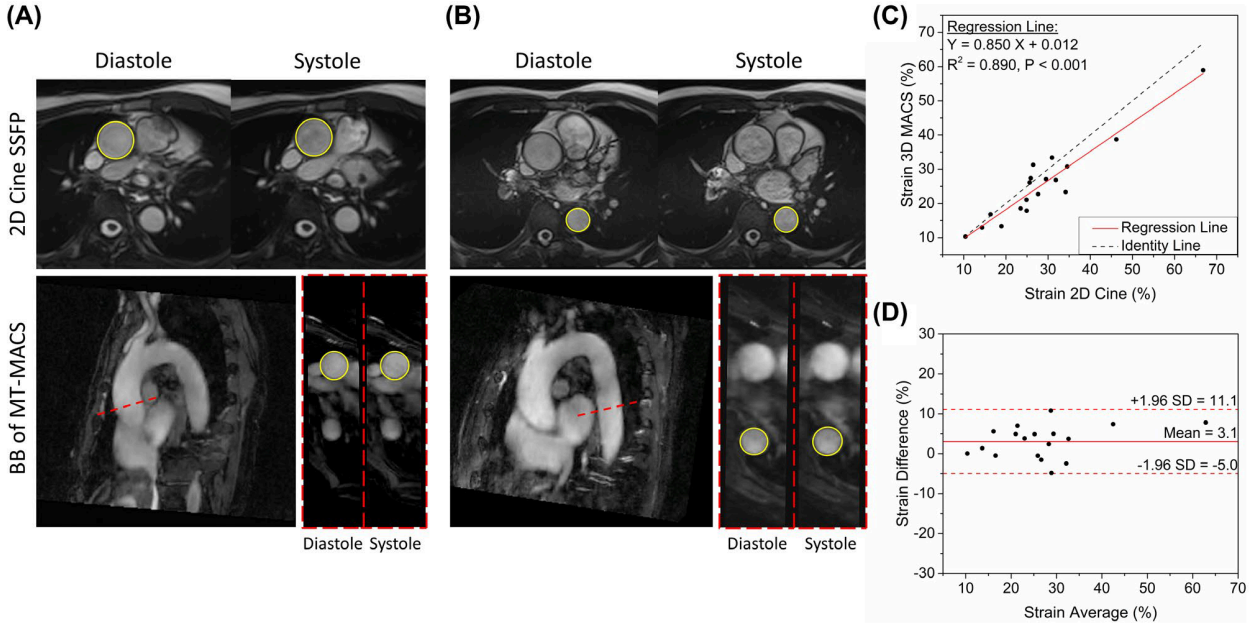

Figure 5.7 Quantification of the functional parameter of aortic vessels. A,B, Graphic illustration of measuring the diastolic and systolic LA of both the ascending and descending aortas in healthy subjects. The lumen boundaries were traced manually on 2D cine SSFP images and BB images of MT-MACS. Both the slice position and slice thickness were matched during the measurements. C, Comparison of aortic vessel strain measurement, using the proposed MT-MACS and a convention 2D cine reference. The black dotted line represents the identity line (Y = X), whereas the solid red line represents regression of the results from these two methods. The intraclass correlation coefficient was 0.947 (*P* < .001). D, Bland-Altman plots comparing the measurement results acquired by these two imaging techniques. Solid red line and dashed red lines indicate the mean and standard deviation of the strain values between the different methods

5.3.3 Detection of aortic abnormalities

Figure 5.8A – 5.8C shows the BB, DB, and GB contrasts, respectively, acquired by MT-MACS sequence from a 38-year-old female patient with aortic aneurysm. Aneurysm affecting the patient's descending aorta was clearly depicted in all three image contrasts

(red boxes). Moreover, through GB imaging, calcified spots, which were pointed out by yellow arrowheads, were identified. The circumferential extent of the abnormalities could be better understood through reformatted short-axis views (yellow arrowheads).

Figure 5.8D – 5.8F shows the imaging results of a 71-year-old female patient with aortic atherosclerosis. Wall thickness at the descending aorta was 4.491 mm (marked in red on the oblique sagittal DB image), which is much higher than that of healthy subjects (approximately 2 mm). The increase of aortic-vessel wall thickness could be confidently identified through the short-axis views of DB and GB image contrasts (pointed out by the yellow arrows), which suggested the existence of aortic atherosclerosis.

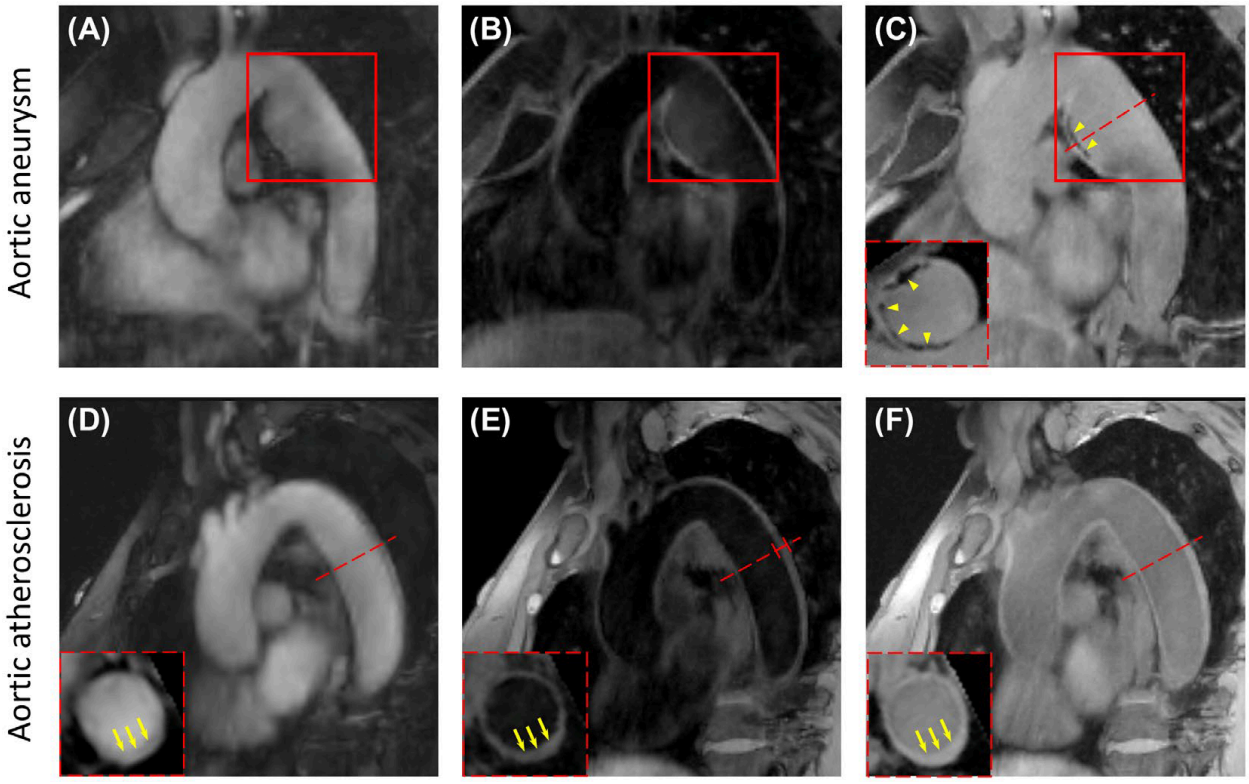

Figure 5.8 Images from 2 patients with aortic aneurysm and aortic atherosclerosis, respectively. The BB (A), DB (B), and GB (C) contrast weightings from a 38-year-old female patient with aortic aneurysm. Aneurysm in the patient's descending aorta was depicted (red boxes). Calcifications were also identified by GB imaging, and the circumferential extent of the abnormalities could be seen through short-axis views (yellow arrowheads). The BB (D), DB (E), and GB (F) images

acquired from a 71-year-old female patient with aortic atherosclerosis. Increased aortic wall thickness (4.491 mm) was marked out in red on the oblique sagittal DB image. The severe thickening of the vessel wall could be clearly identified through the short-axis views of the DB and GB imaging, which were indicated by the yellow arrows. BB, bright-blood; DB, dark-blood; GB, gray-blood

5.4 DISCUSSION

In this study, we present a novel ECG-free and navigator-free 3D MT-MACS technique and demonstrate its feasibility on the thoracic aorta in healthy subjects and patients with thoracic aortic diseases. The proposed MT-MACS achieved high spatial resolution with complete thoracic aorta coverage, and more importantly, provided a comprehensive assessment (multiple image contrasts and cine imaging) of the thoracic aorta within a single 6-minute scan.

Thoracic aortic disease is a stealth condition, which develops silently and typically without any symptoms, but the catastrophic results could affect people at any age[113]. Therefore, imaging plays a crucial role in the monitoring and treatment planning of different types of aortic diseases[120]. Given the abundant strengths of MR over other imaging modalities, in this study, MT-MACS was developed to provide a comprehensive assessment of the thoracic aorta. Compared with previous MR techniques tailored for the thoracic aorta, the proposed method has several advantages. First, MT-MACS provides multiple co-registered images with different image-contrast weightings in a single 6-min scan. To date, MR angiography, including both contrast-enhanced and unenhanced (SSFP, time-of-flight) techniques, has been increasingly favored by clinicians and radiologists in the assessment of thoracic aortic diseases[5,8]. However, characterizing

aortic diseases by simply visualizing the aortic lumen may underestimate the vulnerability and severity of diseases under certain pathological circumstances (i.e., positive remodeling effects in the development of aortic atherosclerosis)[121,141]. Therefore, many MR multicontrast aortic imaging studies were performed with the purpose of directly visualizing the aortic vessel wall and major plaque components, such as intraplaque hemorrhage and calcification[121,142]. Yet, the long acquisition time (about 30-40 min) and misregistration due to interscan subject motion rendered multicontrast imaging logistically impractical and complicated to interpret[125]. In this study, we adopted a T2-IR module to maximize the contrast between the aortic vessel wall and lumen blood and acquired different image contrasts by retrospectively selecting images at different time points along the T1 recovery time dimension. More specifically, there were 300 readout segments within each inversion-recovery period; thus, 300 different image contrasts were available through this sequence. Three typical image contrasts out of 300 were selected, namely BB, DB, and GB image contrasts. The BB images had significantly high signal in the aortic lumen and can be used to detect lumen abnormalities, such as luminal stenosis. The second image contrast, DB images, with suppressed blood signal and higher signal in the aortic vessel wall, can be used to directly visualize the wall morphology. The third image contrast, GB images, which had similar signal levels in the lumen and wall, is designed specifically for the detection of calcification, especially the superficial calcified nodules[140,143]. However, DB image contrast may not ideally identify the vessel wall boundary due to the insufficient contrast between vessel wall and surrounding tissues. As a technical advantage, MT-MACS can provide sliding contrasts to help better delineate aortic wall boundaries. With all these co-registered image contrasts acquired within the

same scan, we can greatly simplify the acquisition workflow and improve the interpretation efficiency and accuracy.

Second, by adopting the MR multitasking framework, the acquisition eliminates the need for ECG triggering, respiratory navigators, or breath-holds. For aortocardiac imaging, one of the major challenges is to perform imaging in the presence of physiological movement (i.e., cardiac pulsation and respiration). Conventional cardiovascular MR techniques adopt ECG for triggering data acquisition to a quiescent cardiac phase (usually middiastole) and breath-holding or navigator gating with a low-rate acceptance window to resolve respiratory motion, thus leading to dramatically inefficient imaging. Furthermore, these unreliable (i.e., ECG triggering at 3-T) or uncomfortable (i.e., breath-holding) motion-resolving strategies may result in severe motion artifacts for specific subjects, such as patients with cardiac arrhythmias[55]. The presented work could potentially overcome these problems by developing an ECG-free and navigator-free imaging technique adapted from the MR multitasking framework. By a single, simple, setup scan, the proposed technique can simplify the imaging workflows and avoid the impact of external motion compensation signal corruption. Moreover, this motion-resolved aortic imaging technique had another advantage over conventional methods: slicing the 4-way imaging tensor along both diastole and systole phases allowed the aortic vessel strain index and distensibility to be determined, which serves as an important illustration for certain types of aortic diseases[144].

In this work, there was a tradeoff between the scan time and the overall image quality. This is because insufficient imaging data would result in a more undersampled optimization problem to recover the spatial coefficients $\mathbf{U_x}$, as shown in Equation 5.5,

which then led to degeneration of the overall image quality. Hence, an optimized protocol needs to balance between the image quality and scan time. Expressly, an optimized scan time means that within this specific scan time, enough clinically relevant diagnostic information could be gained; further reduction of the scan time would lead to deterioration of the overall image quality and unconfident diagnoses. Images reconstructed from at least 6 minutes of data produced average scores of 2 or higher for each contrast weighting and no nondiagnostic images (all ≥ 1). One GB image set was scored “1” by reader 1 and two GB image sets were scored “1” by reader 2. The reason for the fair image-quality scores was inhomogeneous signal intensities between the ascending and descending aortas, which did not affect the diagnosis of calcifications (black spots). Thereby, the scan time for this proposed technique was finalized as 6 minutes, and all quantitative analyses were based on the 6-minute data sets. Measurement results of certain morphological parameters (i.e., lumen and wall area) and functional parameters (i.e., vessel strain index) were in line with those measured through conventional 2D reference techniques, with the lowest ICC equal to 0.947 ($P < .001$). The quantitative analysis further illustrates the feasibility of our proposed MT-MACS technique on thoracic aorta.

Our study has some limitations. First, online reconstruction for MT-MACS technique is not available at this stage. Offline reconstruction was performed on a workstation equipped with two 2.70-GHz 12-core Intel Xeon central processing units and 256 GB of random-access memory, with a 110-minute median reconstruction time. However, with computing power upgrade and advanced reconstruction methodologies, this challenge may be overcome. Second, a further increase in spatial resolution is necessary. Currently, our spatial resolution is 1.38 × 1.38 × 1.38 mm^3 isotropic; however,

for thoracic aortic imaging, especially aortic vessel wall imaging, a higher resolution is highly desirable to better delineate the aortic vessel and reduce partial-volume effects. However, additional scan time is needed to achieve a higher spatial resolution. In the future, additional sources of acceleration, such as deep learning-based super-resolution[145], may be integrated into this technique. Third, feasibility of the proposed technique requires further validation on a larger patient cohort. With multidimensional information, our developed method could be used to assess a variety of thoracic aortic diseases, including aortic atherosclerosis, aortic dissection, aortic aneurysm and vasculitis, either before contrast or after contrast. Thus, more patients need to be recruited to further test the sensitivity and specificity of this technique with respect to different types of thoracic aortic diseases.

5.5 CONCLUSION

We have demonstrated that the proposed MT-MACS technique provides high-quality, multidimensional images for a comprehensive assessment of the thoracic aorta. Technical feasibility of MT-MACS was shown in healthy subjects and patients with thoracic aortic diseases. Further studies in the setting of various thoracic aortic diseases are warranted to validate the clinical utility of this technique. The work presented in this chapter was published in “Hu, Z., et al. (2020). *Magnetic Resonance in Medicine*, 84(5), 2376-2388.”

CHAPTER 6

MR Multitasking-based Multidimensional Assessment of Cardiovascular System – Part II: An Extension to the Entire Heart

6.1 INTRODUCTION

Cardiovascular diseases, such as congenital heart diseases, cardiac masses (i.e., cardiac thrombi or tumors), and vascular diseases, are leading causes of death internationally[146,147]. Diagnosis, risk stratification, and planning of interventional procedures of cardiovascular diseases require accurate evaluation of cardiac anatomy and function[148]. As a versatile imaging modality, cardiovascular MR has the potential to provide a comprehensive assessment of both morphology and function of the entire heart through multi-contrast, motion-resolved and water-fat imaging. For example, bright-blood and dark-blood imaging enables complementary visualization of cardiac chambers and great thoracic vessels[149], and phase-resolved cine imaging is considered the gold standard for assessment of cardiac function[150]. In addition, water-fat imaging based on Dixon methods allows additional fat quantification, which could provide additional diagnostic information of relevance[151,152].

However, despite the aforementioned prominent features, cardiovascular MR is still not widely adopted in current clinical practice[153]. This is mainly owing to three typical

challenges: (a) long imaging time associated with the need for large spatial coverage and high spatial resolution, (b) cumbersome imaging paradigm in which cardiac images are acquired in separate scans with several non-standard planes due to the complexity of cardiovascular anatomy, and (c) nontrivial imaging setup and sacrifice of efficiency for addressing cardiac and respiratory motion during data acquisition, such as ECG triggering and respiratory navigator gating or breath-holding. Hence, current cardiovascular MR acquisition is performed in a time-consuming sequential manner, and must be individually tailored and adjusted, which is highly dependent on operator experience and patient cooperation[154].

In Chapter 6, we presented an MR MultiTasking-based 3D Multi-dimensional Assessment of Cardiovascular System (MT-MACS) technique for comprehensive thoracic aortic imaigng, including multi-contrast imaging and cardiac phase-resolved imaging, with a single 6-min scan[155]. Based on the MR Multitasking framework[55], instead of applying traditional motion removal or correction strategies, MT-MACS allows continuous data acquisition and retrospectively resolves multiple dynamics (i.e., physiological motion and physical relaxation), thereby getting rid of the reliance on ECG-triggering signals or respiratory navigators or breath-holds. In this chapter, we further extend the application of MT-MACS to the comprehensive assessment of the whole cardiac structures and great thoracic vessels with a simple imaging setup. Specifically, the 3D whole-heart MT-MACS technique allows for ECG- and respiratory navigator-free, multi-dimensional (multiple contrast weightings, cine series and water-fat images) imaging with a single 10.3-min scan. The proposed technique was compared with breath-

held, ECG-gated 2D conventional cardiac imaging sequences for validation of morphological and functional measurements of the heart.

6.2 METHODS

6.2.1 Pulse sequence design

In this work, the MT-MACS technique was implemented based on a free-running dual-echo stack-of-stars FLASH readouts with tiny-golden-angle (Ψ = 32.039º) in-plane k-space sampling. T2-prepared inversion recovery (T2-IR) magnetization preparations were applied at constant intervals to maximize the contrast between myocardium/vessel wall and blood and create flexible contrast weightings during T1 recovery. Following each T2-IR preparation module, RF pulse flip angles were 3º for the first 300 segments, and 1º for the next 200 segments. The 1º low-flip-angle readouts were adopted to allow for greater magnetization recovery while collecting continuous motion information. Auxiliary data were interleaved with imaging data every 6 segments and were collected at the 0º radial spoke of the center partition (Figure 6.1). Partition-encoding ordering for the imaging data was randomized with a variable-density Gaussian distribution with the highest density at the center partition.

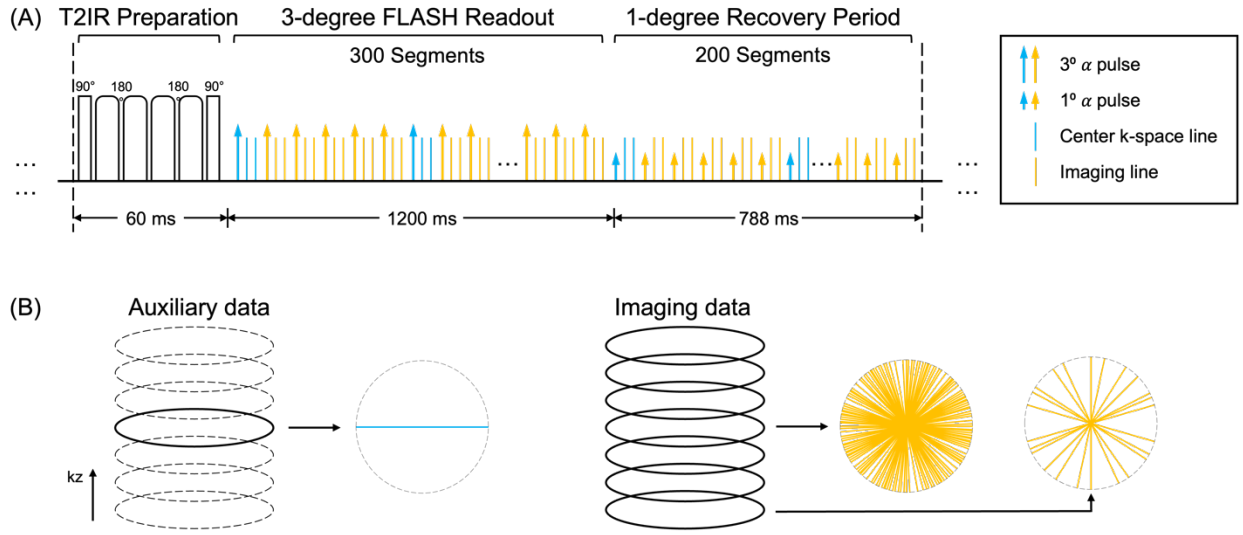

Figure 6.1 Pulse sequence diagram for the MT-MACS technique and corresponding k-space sampling pattern. A, T2-prepared inversion recovery (T2-IR) magnetization preparations are applied at constant intervals followed by dual-echo stack-of-stars FLASH readouts. Following each T2-IR preparation module, RF pulse flip angles were 3º for the first 300 segments, and 1º for the next 200 segments. Auxiliary data were interleaved with imaging data every 6 segments. B, Simplified illustration of k-space sampling strategy. The auxiliary data were collected at the 0º radial spoke of the center partition. For the imaging data, randomized reordering with a variable-density Gaussian distribution with the highest density at the center partition was adopted in this sequence

6.2.2 Image reconstruction framework

Similar to that in the previous chapter, in this work, MT-MACS method adopts a low-rank tensor image model for 7D aortocardiac imaging with three spatial dimensions for whole-heart imaging, a cardiac phase dimension for phase-resolved cine imaging, a respiratory motion dimension for free-breathing imaging, a T2-prepared inversion recovery time dimension for multi-contrast assessment and a T2* decay time dimension for dual-echo imaging. Specifically, a 7D aortocardiac image $I(\mathbf{r}, t_{\mathrm{c}}, t_{\mathrm{r}}, t_{\mathrm{T1}}, t_{\mathrm{E}})$ is modeled as a 5-way multidimensional array (or "tensor") $\mathcal{I}$ with one voxel location dimension $\mathbf{r} = [x, y, z]^T$ indexing 3D spatial locations and four time dimensions indexing cardiac motion t_{c},

respiratory motion t_{r}, inversion recovery t_{T1} and echo time t_{E}, respectively. High image correlation along and across different time dimensions induces $\mathcal{I}$ to be a low-rank tensor, such that it can be separated in the following sense:

$$\mathcal{I} = \mathcal{C} \times_1 \mathbf{U_r} \times_2 \mathbf{V}_{t_{\mathrm{c}}} \times_3 \mathbf{W}_{t_{\mathrm{r}}} \times_4 \mathbf{Y}_{t_{\mathrm{T1}}} \times_5 \mathbf{Z}_{t_{\mathrm{E}}} \tag{6.1}$$

where $\times_n$ denotes n-mode multiplication; the columns of factor matrix $\mathbf{U_r}$ contain the spatial basis images and the columns of $\mathbf{V}_{t_{\mathrm{c}}}$, $\mathbf{W}_{t_{\mathrm{r}}}$, $\mathbf{Y}_{t_{\mathrm{T1}}}$, and $\mathbf{Z}_{t_{\mathrm{E}}}$ contain the temporal basis functions for each time dimension[129].

Based on the MR Multitasking framework, MT-MACS uses a mixed strategy that reconstructs the image tensor $\mathcal{I}$ by directly recovering the core tensor and different factor matrices, which can be divided into 5 steps[128,155]:

1. Generate ungated images, which are reconstructed using explicit low-rank matrix imaging with only one time dimension representing elapsed time, for image-based cardiac phase and respiratory position identification[55] by means of a modified T1 recovery-aware k-means clustering approach, placing the corresponding images into 20 cardiac bins and 6 respiratory bins.
2. Determine the inversion recovery basis functions in $\mathbf{Y}_{t_{\mathrm{T1}}}$ from a pre-generated dictionary of inversion-recovery signals built from the Bloch equations with a range of T1, T2 and B1 inhomogeneity values.
3. Estimate core tensor $\mathcal{C}$ and the basis functions along the cardiac motion, respiratory phase, and echo time dimensions, namely $\mathbf{V}_{t_{\mathrm{c}}}$, $\mathbf{W}_{t_{\mathrm{r}}}$, and $\mathbf{Z}_{t_{\mathrm{E}}}$, respectively, from the high-temporal-resolution auxiliary data. Reconstruct the spatial coefficients $\mathbf{U_r}$ by fitting the derived tensor factors to the acquired imaging data.

6.2.3 In vivo study

The in vivo study was approved by the local institutional review board, and all subjects provided written informed consent before participation. Nine healthy volunteers (aged 28-79 years, 5 females) were recruited for the study. All imaging examinations were performed on a 3-T clinical MR scanner (MAGNETOM Vida; Siemens Healthcare, Erlangen, Germany) with a standard 18-channel body coil and a 32-channel spinal coil. MT-MACS imaging was prescribed based on an axial scout scan to cover the whole heart with no ECG triggering or respiratory navigator. Major imaging parameters were set as follow: coronal orientation, FOV = 224 × 224 × 162.4 mm^3, spatial resolution = 1.4 × 1.4 × 2.8 mm^3 and then interpolated to 1.4-mm isotropic during the process of image reconstruction, duration of T2-IR preparation module = 60 ms, TR/TE1/TE2 = 3.94/1.23/2.46 ms, bandwidth = 1250 Hz/pixel, total acquisition time = 10.3 min. In addition, conventional ECG-triggered and end-expiration breath-held sequences were also acquired in all healthy subjects to serve as the references for morphological (i.e., myocardial wall thickness for each cardiac chamber) and functional (i.e., left ventricular ejection fraction [LVEF]) quantification of the heart. Specifically, 2D T2-weighted dark-blood TSE sequence was performed in a 4-chamber orientation with major imaging parameters including: FOV = 360 × 360 mm^2, matrix size = 256 × 256, slice thickness = 5 mm, flip angle = 180º, TR = 1 cardiac cycle, TE = 71 ms, turbo factor = 17, echo spacing = 5.49 ms, bandwidth = 849 Hz/px, and ECG-triggered to the mid-diastole. Multislice 2D cine imaging based on the balanced SSFP sequence was performed in a short axis orientation with major imaging parameters including: FOV = 300 × 300 mm^2, matrix size = 224 × 224, slice thickness = 8 mm, flip angle = 36º, TR/TE = 27.1/1.31 ms, echo spacing

= 3.01 ms, bandwidth = 1313 Hz/px, 25 phases based on retrospective gating, and a total of 12 contiguous slices were acquired for each healthy subject for full left ventricular coverage.

6.2.4 Image analysis

Images acquired using MT-MACS were reconstructed offline to generate water-only images with multiple contrast weightings (i.e., BB, DB, GB) and corresponding cine series as well as fat-only images. The DICOM-format MT-MACS images were loaded to a workstation (LEONARDO, Siemens Healthcare) and reformatted to match the 2D reference images in both location and slice thickness. All quantitative analyses were performed using cvi42 version 5.12.1 (Circle Cardiovascular Imaging, Calgary, Canada).

Qualitative analysis

Subjective image quality assessments of both water-only and fat-only image sets at mid-diastolic end-expiratory phase were performed by 2 independent radiologists with at least 5 years of experience in cardiovascular imaging. For water-only images, image quality scores were recorded for two anatomic structures (cardiac chambers and thoracic aorta) with three representative image contrasts (BB, DB, and GB). For fat-only images, overall image quality for the entire 3D volume was graded for each image set. The criteria used for image quality scoring were listed in Table 6.1.

Table 6.1 Image quality scoring criteria

Cardiac Chambers	1: Chambers not visualized or diagnostically not assessable. 2: Chambers distinguishable but myocardial walls poorly defined, only gross features evaluable. 3: Chambers clearly distinguishable with well-defined myocardial walls confidently evaluable but with poor definition of the papillary muscles. 4: Chambers clearly distinguishable with excellent myocardial wall definition and with clear definition of the papillary muscles.
Thoracic Aortas	1: Aortas not visualized or diagnostically not assessable. 2: Aortas distinguishable but with poor vessel wall definition. 3: Aortas clearly distinguishable with good vessel wall definition but with poor sharpness due to motion artifacts. 4: Aortas clearly distinguishable with excellent vessel wall definition and good sharpness.
Fat	1: Severe blurring of cardiac chambers and thoracic aortas. 2: Significant blurring of cardiac chambers and thoracic aortas. 3: Mild blurring of cardiac chambers and thoracic aortas. 4: No blurring of cardiac chambers and thoracic aortas.

Quantitative analysis

To validate the accuracy of MT-MACS in quantifying morphological parameters of the cardiac chambers, myocardial wall thicknesses of the left atria (LA)/left ventricle (LV)/right atria (RA)/right ventricle (RV) were measured and compared with the conventional reference images. Specifically, myocardial wall thickness of each cardiac chamber was measured at the same location on the DB images of MT-MACS at the mid-diastolic end-expiratory phase and corresponding matched 2D T2-TSE images, respectively.

For the accuracy analysis of LVEF measurement, the blood-myocardium boundary was manually contoured in each slice of the MT-MACS BB images and corresponding

matched 2D cine images for both the end-diastolic and end-systolic phases, respectively. LVEF was then calculated for each sequence using the following equation (14):

$$\mathrm{LVEF} = \frac{\mathrm{LVEDV} - \mathrm{LVESV}}{\mathrm{LVEDV}} \times 100\% \tag{6.2}$$

where LVEDV and LVESV represents the end-diastolic and end-systolic left ventricular volume, respectively.

6.2.5 Statistical analysis

For qualitative analysis, weighted Cohen's kappa (κ) values were used to evaluate interreader agreement for image quality scoring. For myocardial wall thickness measurements of the LA/LV/RA/RV, ICCs and Bland-Altman analysis were used to measure agreement between MT-MACS and corresponding matched 2D references. For LVEF measurement, linear regression and Bland-Altman analyses were adopted to assess quantification agreement. All statistical analyses were performed in SPSS version 24 (IBM Corp., Armonk, NY). A *P* value < 0.05 was considered to indicate statistical significance.

6.3 RESULTS

The MT-MACS imaging was performed successfully on all subjects. Figure 6.2 shows slices of the ventricular chambers (coronal view and short axis view) and thoracic aorta (candy-cane view) at the mid-diastolic end-expiration phase in two representative healthy subjects. Both water-only and fat-only images generated by MT-MACS are displayed. For water-only images, BB, DB and GB image contrasts are shown for each slice orientation.

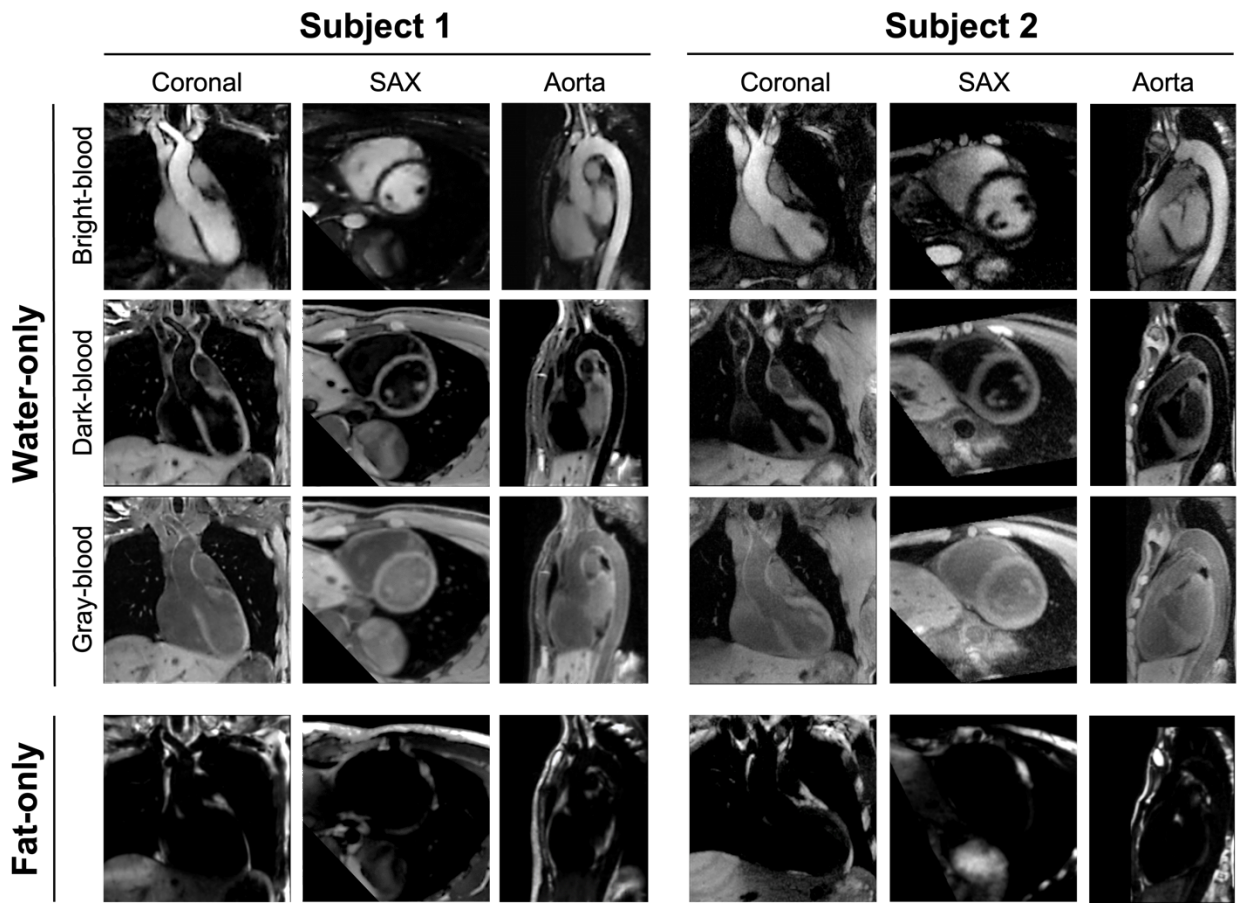

Figure 6.2 Example MT-MACS images of the ventricular chambers (coronal view and short axis view) and thoracic aorta at the mid-diastolic end-expiration phase generated from a 28-year-old female subject (Subject 1) and a 65-year-old male subject (Subject 2). Water-only images with multiple contrast weightings, including bright-blood (BB), dark-blood (DB) and gray-blood (GB), and fat-only images are displayed for each slice orientation

6.3.1 Qualitative analysis

For qualitative analysis, a total of 36 3D image sets (3 water-only contrasts and 1 fat-only) were scored for image quality. Image quality scores given by both readers are shown in Table 6.2. For cardiac chambers, the interreader agreements quantified by weighted Cohen's kappa values 0.727, 0.609, and 1.000 for BB, DB, and GB MT-MACS images, respectively; for thoracic aorta, the interreader agreements for BB, DB, and GB MT-MACS images were 0.727, 0.727, and 1.000, respectively; and 1.000 for fat-only images.

Table 6.2 Image quality scores given by 2 independent radiologists over all 9 healthy subjects

	Cardiac Chambers						Thoracic Aorta						Fat	
	BB		DB		GB		BB		DB		GB			
	R1	R2	R1	R2	R1	R2	R1	R2	R1	R2	R1	R2	R1	R2
S1	4	4	4	4	4	4	4	4	4	4	4	4	4	4
S2	4	4	4	4	4	4	4	4	3	3	4	4	4	4
S3	3	3	4	3	4	4	3	3	3	3	4	4	4	4
S4	3	3	3	3	4	4	4	4	3	4	3	3	4	4
S5	4	3	4	4	4	4	4	4	4	4	4	4	4	4
S6	4	4	4	4	4	4	3	4	4	4	4	4	4	4
S7	4	4	4	4	4	4	3	3	4	4	4	4	3	3
S8	4	4	4	4	4	4	4	4	4	4	4	4	4	4
S9	4	4	4	4	3	3	4	4	4	4	3	3	4	4
Mean	3.8	3.7	3.9	3.8	3.9	3.9	3.7	3.8	3.7	3.8	3.8	3.8	3.9	3.9
SD	0.4	0.5	0.3	0.4	0.3	0.3	0.5	0.4	0.5	0.4	0.4	0.4	0.3	0.3

Abbreviations: BB – bright-blood; DB – dark-blood; GB – gray-blood; R1 – reader 1; R2 – reader 2; S1-7 – subject 1-7; SD – standard deviation

6.3.2 Quantitative analysis

An illustration of myocardial wall thickness measurements of the LA/LV/RA/RV is shown in Figure 6.3A. The thicknesses were measured to be 2.52 ± 0.19 mm, 8.99 ± 0.53 mm, 2.50 ± 0.21 mm, and 4.32 ± 0.78 mm for LA, LV, RA, and RV by MT-MACS, respectively, which are all within the normal anatomical range[156–158]. The cardiac structures on 2D T2-TSE images from 2 subjects were substantially blurred due to respiratory motion and were therefore excluded from analysis. Good to excellent agreement in myocardial wall thickness measurements was demonstrated with Bland-Altman plots between MT-MACS

and 2D T2-TSE in the remaining 7 subjects. The ICCs were 0.781/0.929/0.680/0.878 for LA/LV/RA/RV, respectively (Figure 6.3B).

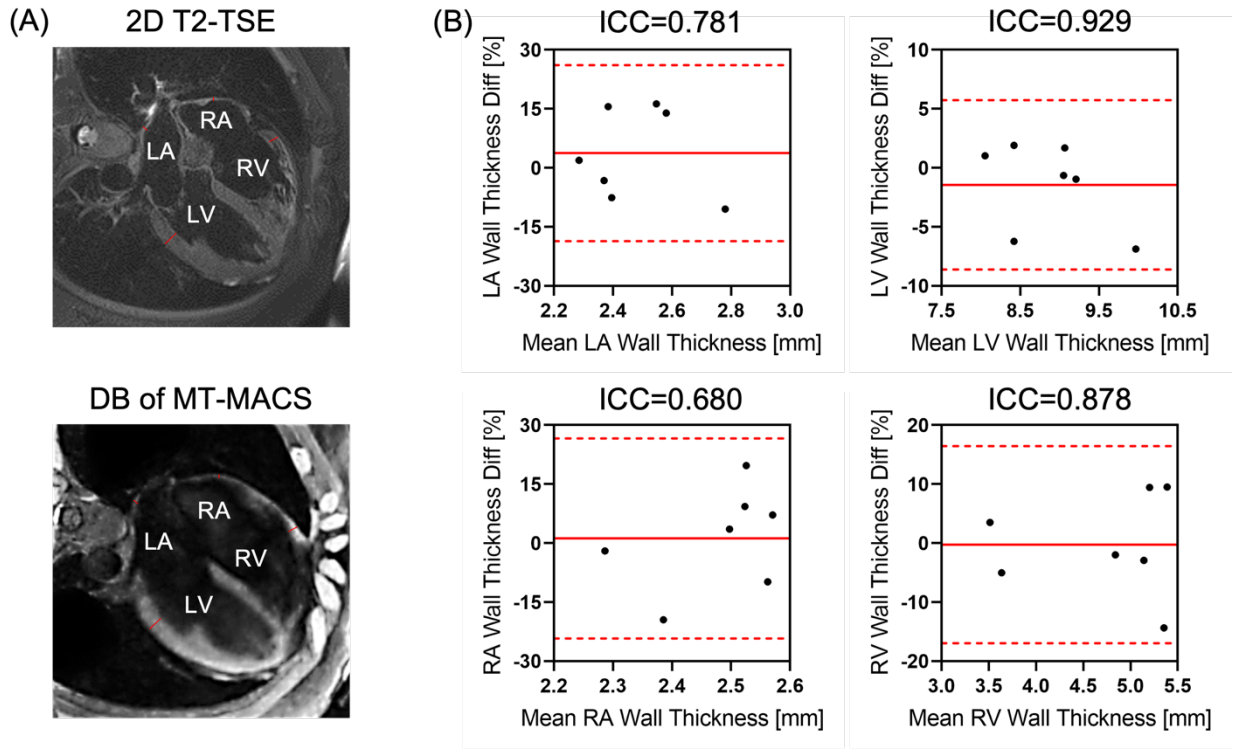

Figure 6.3 Quantification of myocardial wall thickness of the left atria (LA)/left ventricle (LV)/right atria (RA)/right ventricle (RV). A, Graphic illustration of measuring the myocardial wall thickness of the LA/LV/RA/RV in a 40-year-old male subject. Myocardial wall thickness of each cardiac chamber was measured at the same location on the dark-blood images of MT-MACS at the mid-diastolic end-expiratory phase and corresponding 2D T2-weighted turbo spin-echo images with matched location and slice thickness. B, Bland-Altman plots and intraclass correlation coefficients comparing measurement agreements between these two imaging techniques

Comparison of LVEF measurement between MT-MACS and 2D cine balanced SSFP is displayed in Figure 6.4. Overall, MT-MACS provided slightly lower LVEF measurements compared with the 2D cine sequence (regression line: Y = 1.060X – 0.075; R2 = 0.855, $P < 0.001$), which may result from the contrast difference between gradient-echo-based and SSFP-based sequences, but the overall values were still within the physiological range[159].

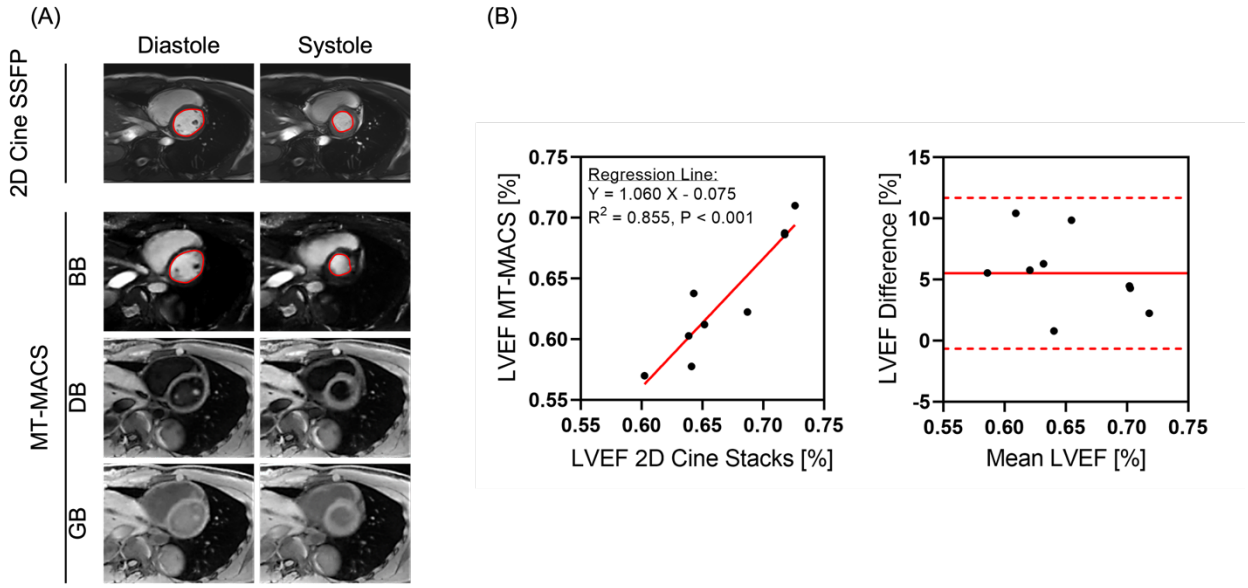

Figure 6.4 Quantification of left ventricular ejection fraction (LVEF). A, Graphic illustration of measuring LVEF in a 39-year-old male subject. The blood-myocardium boundary was manually contoured in each slice of the MT-MACS bright-blood images and corresponding 2D cine balanced SSFP images with matched location and slice thickness for both the end-diastolic and end-systolic phases. B, Linear regression and Bland-Altman analyses comparing the measurement results acquired by these two imaging techniques

6.4 DISCUSSION

Accurate assessment of morphology as well as function of the heart is crucial for diagnosis and treatment planning in patients with cardiovascular diseases. Cardiovascular MR is considered the only single imaging modality that can achieve a comprehensive assessment of the entire cardiovascular system[160]. However, cardiovascular MR is still not a first-line study in today's clinical practice, largely due to the slow imaging speed and complex clinical workflow[150,153]. To optimize clinical scan time and simplify imaging workflow, in the past few years, various novel comprehensive cardiovascular MR approaches have been developed[149,154,161–163]. Feng et al. proposed

a 5D cardiac and respiratory motion-resolved whole-heart imaging technique based on extra-dimensional golden-angle radial sparse parallel (XD-GRASP) framework, which can provide whole-heart anatomical information at different cardiac phases[154]. However, only a single bright-blood image contrast is available through this technique, and this lumenography-based imaging alone may not be optimal in myocardium or vessel wall visualization[155]. To generate complementary image contrasts, a 3D simultaneous bright-blood and black-blood phase sensitive (BOOST) whole-heart MR sequence was developed by Ginami et al.[164]. However, the dark-blood volume was retrospectively generated using 2 differently weighted bright-blood volumes after non-rigid motion correction; thereby any residual motion artifacts would propagate into the black-blood volume leading to image blurring[149]. In addition, the acquisition was ECG-triggered to mid-diastolic resting period and thus cardiac functional parameters cannot be evaluated with this technique.

A novel ECG- and respiratory navigator-free 3D MT-MACS technique was recently published, and its technical feasibility was demonstrated on thoracic aortas[155]. To meet the clinical needs and address the drawbacks of other comprehensive techniques, in this work, we extended the spatial coverage of the previous MT-MACS technique to assess the whole cardiac structures and great thoracic vessels. Compared with previous comprehensive MR techniques tailored for whole-heart assessment, the proposed method has several advantages. First, MT-MACS provides multiple co-registered images with different image contrast weightings in a single 10.3-min acquisition. A T2-IR preparation module was adopted to maximize the contrast between the myocardium/vessel wall and blood while acquiring multiple image contrasts by

retrospectively picking out images at different time points along the inversion recovery time dimension. Specifically, 3 typical image contrast weightings out of 300 FLASH readout segments were selected, namely BB, DB and GB image contrasts. Second, by adopting a continuous 3D stack-of-stars sampling scheme, MT-MACS eliminates the need for ECG triggering, respiratory navigators, or breath-holds. This greatly improves the acquisition efficiency and reduces the complexity of imaging workflow, and, in the meantime, avoids unreliability or discomfort induced by those external motion compensation methods. Moreover, by unfolding the 5-way imaging tensor along the cardiac motion dimension, MT-MACS can provide cardiac phase-resolved cine images for functional imaging (i.e., LVEF quantification), which serves as an important illustration for certain types of cardiovascular diseases[165]. Third, the dual-echo acquisition scheme allows MT-MACS to achieve water-fat imaging based on Dixon methods[166,167]. Specifically, by adopting a two-point Dixon method, MT-MACS has the capability to depict and quantify the relative composition of water and fat in tissues, which could potentially help form a more comprehensive basis for assessment of the cardiovascular system since fat volume has been linked to increased risk of certain cardiovascular diseases[168].

Our study has some limitations. First, the proposed MT-MACS achieves water-fat imaging based on the original two-point Dixon method, which is under the assumption of perfect B0 field and negligible susceptibility. However, with a shift in B0 field, water and fat will accumulate an additional phase shift, resulting in the mixtures of both water and fat on the final water-only and fat-only images. A possible solution would be to use the extended two-point Dixon[169] or three-point Dixon methods[170]. Second, feasibility of the proposed technique requires further validation on patients. The MT-MACS technique

could be used to assess various of cardiovascular diseases, such as congenital heart diseases and intracardiac thrombus. Therefore, such patients need to be recruited to investigate the sensitivity and specificity of this technique regarding to different types of diseases.

6.5 CONCLUSION

In this work, we extended the previously developed MT-MACS technique to comprehensive assessment of the combined cardiac and thoracic aortic system. With a simple imaging setup, MT-MACS allows for multi-dimensional imaging of the entire heart without the need for ECG-triggering, respiratory navigator gating or breath holding. Further studies in the setting of various cardiovascular diseases are warranted to validate the clinical utility of this technique.

CHAPTER 7

MR Multitasking for Cerebrovascular Evaluation: Simultaneous Quantification of Permeability and Leakage-insensitive Perfusion by Dynamic T1/T2* Mapping

7.1 INTRODUCTION

Dynamic MR imaging with the administration of a paramagnetic CA is widely used for assessing brain tissue abnormalities[12,171]. Two common methods are dynamic contrast-enhanced MR (DCE-MR)[12] and dynamic susceptibility contrast-enhanced MR (DSC-MR)[13], which track the tissue-level contrast kinetics based on CA-induced T1- and T2/T2*-shortening effects, respectively[172]. Using pharmacokinetic and/or biophysical modeling, DCE-MR can quantify vascular permeability-related properties, such as fractional plasma volume (v_p), transfer constant (K^{trans}), and fractional extravascular-extracellular volume (v_e), and DSC-MR can quantify perfusion-related properties, such as cerebral blood volume (CBV) and cerebral blood flow (CBF). While both permeability and perfusion parameters are often cited for assessing various cerebrovascular disorders, especially brain cancer, previous studies have demonstrated that they may provide different but complementary information[34]. Therefore, the comprehensive analysis of permeability and perfusion metrics may form a more complete basis for disease evaluation than with either one alone and thus improve diagnostic and prognostic performance[43].

A comprehensive assessment of vascular permeability and perfusion can be achieved by separately acquiring both DCE-MR and DSC-MR sequences in one imaging session[44]. However, this approach requires additional scan time and, more importantly, multiple doses of CA that may raise risk of health in patients[46,48,49]. Integrating vascular permeability and perfusion quantification into a single acquisition along with single-dose contrast administration is a more compelling solution. However, when combined together, both DCE-MR and DSC-MR signals can be adversely impacted by the opposing relaxation effects (i.e., T1 vs. T2/T2*). This is non-negligible when BBB breaks down and CA extravasates, which is common in brain tumor areas. Several early methods based on single-echo acquisitions have been published to correct the contrast leakage effect for perfusion imaging. The most widely-established is the Boxerman-Schmainda-Weisskoff algorithm that estimates the leakage effects by comparing tumor relaxation curves with those in a reference non-enhancing tissue[173]. However, this method suffers from the restrictive assumption of identical hemodynamic properties between the tumor and reference tissue, leading to unreliable estimations of perfusion parameters[174].

In the past two decades, multi-echo-based methods have been shown to be more reliable for simultaneously estimating DCE-MR and DSC-MR parameters[175–177]. With multi-echo data, the T1-leakage effects caused by BBB disruption can be quantified and applied to estimate permeability parameters. After eliminating the T1-leakage effects, the remaining T2/T2*-leakage effects, which typically lead to overestimations of perfusion parameters, can further be mitigated by adopting either gamma-variate fitting or model-based postprocessing approaches[178–181].

Despite these promising results, multi-echo-based methods continue to face several technical challenges. First, temporal resolution and/or spatial coverage are often sacrificed because of the longer readout time of multiple echoes[180]. However, high temporal resolution is crucial for accurate quantification of DCE-MR and DSC-MR parameters[182]. Second, most existing techniques linearly transform the dynamic changes in signal intensity to CA concentration for kinetic modeling. However, the linearity approximation may result in considerable quantification errors in tissues with high-contrast uptake[183,184]. Third, as the most commonly used acquisition strategy for current multi-echo-based approaches, the gradient-echo EPI pulse sequences suffer from susceptibility-induced signal dropout and imaging distortion. These artifacts appear particular around air-tissue interfaces, and in the case of brain tumors, around resection cavities, which precludes the quantification of permeability and perfusion in these regions[172].

MR multitasking is a recently proposed imaging framework that models multiple dynamics in a multidimensional array and exploits the strong spatiotemporal correlation along and across different dimensions to achieve accelerated imaging[55]. To address the aforementioned limitations of existing multi-echo-based methods, in this work, we developed an MR MultiTasking-based Dynamic Imaging for Cerebrovascular Evaluation (MT-DICE) technique for combined DCE-MR and DSC-MR. With a single 7.6-min scan and a single-dose contrast injection, MT-DICE allows for simultaneous quantification of vascular permeability and leakage-insensitive perfusion based on dynamic T1/T2* mapping at a 1.2-s temporal resolution.

7.2 METHODS

7.2.1 Pulse sequence design

The MT-DICE technique employs a 3D Cartesian acquisition with periodic non-selective saturation recovery (SR) preparations (SR interval = 1.2 s) followed by 60 continuous multi-echo FLASH readout segments (Figure 7.1). During each segment of the data acquisition (segment duration = 19.30 ms), 6 echoes are consecutively collected (TEs = 2.46/4.92/7.38/9.84/12.30/17.22 ms). Two interleaved subsets of k-space data are collected, as demonstrated in Figure 7.1B: the high-temporal-resolution training data ($\mathbf{d}_{\mathrm{tr}}$) are acquired every 4 segments at the center encoding line (k_y = k_z = 0)[55], and the imaging data ($\mathbf{d}$) are randomly collected with a 3D variable-density Gaussian sampling pattern along both phase- and partition-encoding directions to achieve incoherent k-space undersampling.

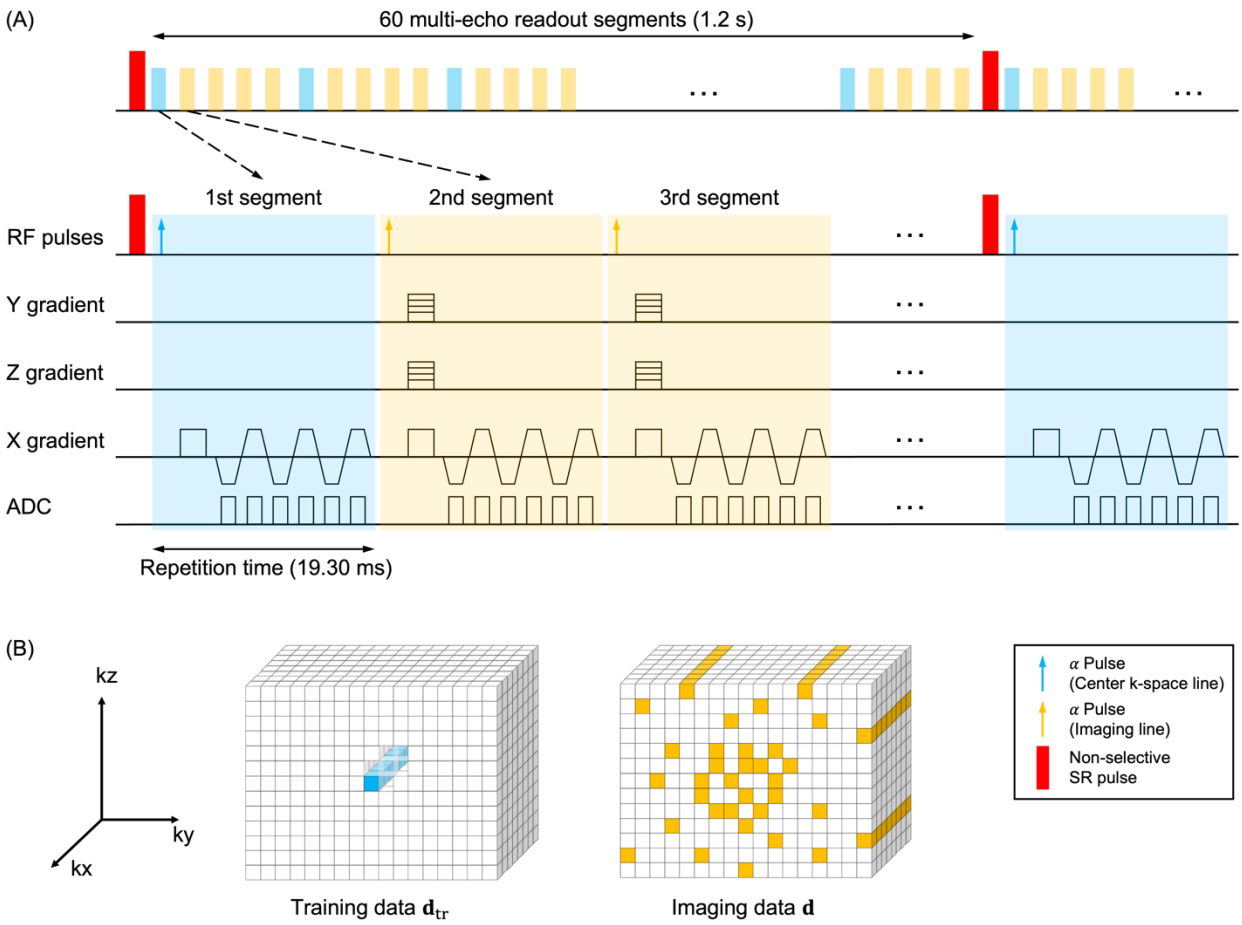

Figure 7.1 Pulse sequence diagram for the MT-DICE technique and corresponding k-space sampling pattern. A, Non-selective saturation recovery (SR) pulses were applied every 60 FLASH readout segments. Within each segment, 6 lines with different echo times were collected at the same k-space location after every alpha pulse. The high-temporal-resolution training data are acquired every 4 multi-echo readout segments as the low-rank tensor subspace training data. B, Simplified illustration of k-space sampling strategy. The training data were collected at the center encoding line, and the imaging data were collected by Cartesian sampling with randomized reordering with a variable-density Gaussian distribution in k_y and k_z directions

7.2.2 Multidimensional imaging based on MR multitasking

Image model

The MT-DICE method adopts a low-rank tensor (LRT) image model for 6D brain imaging with three spatial dimensions for 3D whole-brain coverage, an SR time dimension and an

echo time dimension for dynamic T1 and T2* quantification, respectively, and a contrast dynamics dimension for capturing contrast kinetics. Specifically, a 6D brain image $I(\mathbf{r}, \tau, t_{\mathrm{E}}, t)$ is modeled as a 4-way multidimensional array (or "tensor") $\mathcal{I}$ with elements $\mathcal{I}_{abcd} = I(\mathbf{r}_a, \tau_b, t_{\mathrm{E,c}}, t_d)$, where the first tensor dimension indexes the set of A voxel locations $\{\mathbf{r}_a = [x_a, y_a, z_a]^T\}_{a=1}^{A}$ and other tensor dimension indexes time dimensions including SR time τ, echo time t_{E} and contrast dynamic t. For example, $\{\tau_b\}_{b=1}^{B}$ indexes B segments within each SR period, $\{t_{\mathrm{E,c}}\}_{c=1}^{C}$ indexes C echo times, and $\{t_d\}_{d=1}^{D}$ indexes D contrast dynamic phases. The high correlation between images along and across time dimensions makes $\mathcal{I}$ an LRT, and is therefore partially separable in the following sense:

$$I(\mathbf{r}, \tau, t_{\mathrm{E}}, t) = \sum_{\ell=1}^{L} u_\ell(\mathbf{r}) \phi_\ell(\tau, t_{\mathrm{E}}, t) \tag{7.1}$$

where $u_\ell(\mathbf{r})$ is the ℓth of L spatial basis images, and $\{\phi_\ell(\tau, t_{\mathrm{E}}, t)\}_{\ell=1}^{L}$ spans the multidimensional temporal subspace representing a mixture of SR times, multiple echo times, and dynamic contrast changes. Furthermore, in the LRT image model, each $\phi_\ell(\tau, t_{\mathrm{E}}, t)$ is itself low-rank and can be factorized into basis functions for each time dimension:

$$\phi_\ell(\tau, t_{\mathrm{E}}, t) = \sum_{m=1}^{M} \sum_{n=1}^{N} \sum_{p=1}^{P} c_{\ell mnp} v_m(\tau) w_n(t_{\mathrm{E}}) z_p(t) \tag{7.2}$$

where $v_m(\tau)$, $w_n(t_{\mathrm{E}})$ and $z_p(t)$ denote the mth, nth and pth basis functions along the SR time, echo time and contrast dynamics dimensions, respectively; and $c_{\ell mnp}$ denotes the elements of the core tensor $\mathcal{C}$. Thus, the image tensor $\mathcal{I}$ can be expressed as:

$$\mathcal{I} = \mathcal{C} \times_1 \mathbf{U} \times_2 \mathbf{V} \times_3 \mathbf{W} \times_4 \mathbf{Z} \tag{7.3}$$

where $\times_n$ denotes n-mode multiplication; the columns of factor matrix $\mathbf{U}$ contain the spatial basis images and the columns of $\mathbf{V}$, $\mathbf{W}$, and $\mathbf{Z}$ contain the temporal basis functions for each time dimension[129].

Image reconstruction

There are various low-rank strategies available for reconstruction of the undersampled multidimensional array, either implicitly or explicitly[55,130,131,133,134]. MT-DICE, similar to the original MR multitasking work[55], adopts a mixed strategy that reconstructs the image tensor by sequentially recovering each of its factor matrices. Specifically, in this work, image reconstruction can be divided into 4 steps:

1. Predetermine the temporal basis functions in $\mathbf{V}$ (along the SR time dimension). According to the Bloch equations, a predefined training dictionary of physically feasible SR-FLASH signal curves is generated ahead of time with different T1 and B1 inhomogeneity values. Basis functions in $\mathbf{V}$ are extracted from the singular value decomposition (SVD) of this training dictionary. Temporal basis functions for the echo time dimension are not determined in this step due to the complexity of modeling B0 inhomogeneities and will instead be generated in the following steps[185].
2. Apply small-scale LRT completion to recover missing elements from the training tensor $\mathcal{D}_{\mathrm{tr}}$, which is reshaped from the collected high-temporal-resolution training data $\mathbf{d}_{\mathrm{tr}}$. The training tensor $\mathcal{D}_{\mathrm{tr}}$ covers multiple dynamic contrast combinations throughout the scan; however, it is still highly undersampled since it is impossible to acquire all the image contrast combinations.

$$\widehat{\mathcal{D}}_{\mathrm{tr}} = arg \min_{\mathbf{D}_{\mathrm{tr},(2)} \in \mathrm{range}(\mathbf{V})} \|\mathbf{d}_{\mathrm{tr}} - M(\mathcal{D}_{\mathrm{tr}})\|_2^2 + \lambda \sum_{n=1,3,4} \left\|\mathbf{D}_{\mathrm{tr},(n)}\right\|_* \quad (7.4)$$

where $M(\cdot)$ represents the undersampling pattern of the training dataset; $\mathbf{D}_{\mathrm{tr},(n)}$ denotes the mode-n (n =1,2,3,4) unfolding of the training tensor $\mathcal{D}_{\mathrm{tr}}$; $\|\cdot\|_*$ is the nuclear norm that promotes low-rankness of each unfolded matrix and λ weights the nuclear norm penalties.

3. Extract temporal basis functions along the echo time and contrast dynamics dimensions, namely, columns in $\mathbf{W}$ and $\mathbf{Z}$ respectively, as well as the core tensor $\mathcal{C}$ from the high-order SVD of the completed training tensor $\widehat{\mathcal{D}}_{\mathrm{tr}}$.
4. Estimate the spatial coefficients $\mathbf{U}$ by solving the following optimization problem:

$$\widehat{\mathbf{U}} = arg \min_{\mathbf{U}} \|\mathbf{d} - \Omega[\Phi \times_1 \mathbf{FSU}]\|_2^2 + R(\mathbf{U}) \quad (7.5)$$

where $\Phi = \mathcal{C} \times_2 \mathbf{V} \times_3 \mathbf{W} \times_4 \mathbf{Z}$ is the combined temporal factor; $\Omega(\cdot)$ is the undersampling operator; $\mathbf{F}$ denotes spatial Fourier transform; and $\mathbf{S}$ denotes the coil sensitivity maps. $R(\cdot)$ applies the regularization functional, which is chosen as an anisotropic spatial total variation penalty to incorporate compressed sensing into the presented image reconstruction framework.

A diagram of the LRT image model adopted in the proposed MT-DICE and overall reconstruction workflow are shown in Figure 7.2.

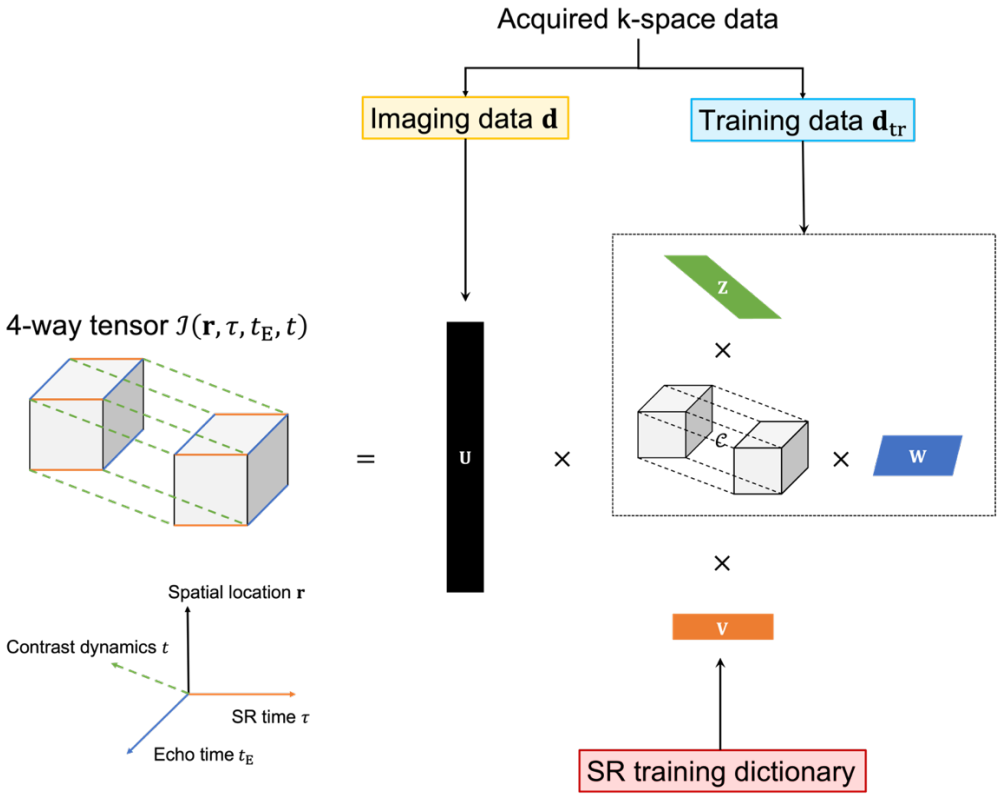

Figure 7.2 Illustration of multiple dimensions of the 4-way low-rank tensor image model adopted by MT-DICE and corresponding reconstruction workflow

7.2.3 Dynamic T1/T2* quantification

Voxel-wise dynamic T1/T2* quantification is performed following image reconstruction. At a given pixel, the multi-echo SR-FLASH signal intensity can be expressed as:

$$S\left(\mathrm{A}, \alpha, \mathrm{B}, \mathrm{n}, \mathrm{TE}, \mathrm{T}_1(t), \mathrm{T}_2^*(t)\right) = \mathrm{A}\frac{1-e^{-\mathrm{TR}/\mathrm{T}_1(\mathrm{t})}}{1-e^{-\mathrm{TR}/\mathrm{T}_1(\mathrm{t})}\cos\alpha}\left[1+(\mathrm{B}-1)(e^{-\mathrm{TR}/\mathrm{T}_1(\mathrm{t})}\cos\alpha)^{\mathrm{n}}\right]e^{-\mathrm{TE}/\mathrm{T}_2^*(\mathrm{t})}\sin\alpha \quad (7.6)$$

where amplitude A absorbs proton density; α denotes the FLASH flip angle; B represents saturation factor (ideally zero); n denotes SR segment index; TE represents echo times; $\mathrm{T}_1(t)$ and $\mathrm{T}_2^*(t)$ are the dynamic T1/T2* values over all contrast phases, respectively. For

each pixel, we fit for A, α, B, $\mathrm{T}_1(t)$ and $\mathrm{T}_2^*(t)$ using the lsqnonlin (nonlinear least-square) solver in MATLAB (R2018a, MathWorks, Natick, MA).

7.2.4 Estimations of permeability and leakage-insensitive perfusion parameters

The T1-based CA concentration for tissues of interest was directly derived from the dynamic longitudinal relaxation rates $\mathrm{R}_1(t)$ (R1 = 1/T1) according to the following equation:

$$C_{\mathrm{t}}^{\mathrm{T}_1}(t) = \frac{\Delta \mathrm{R}_1(t)}{r_1} = \frac{\mathrm{R}_1(t) - \mathrm{R}_1(0)}{r_1} \tag{7}$$

where the longitudinal relaxivity r_1 was set to be 3.6 L·mmol^{-1}·s^{-1} in this work[186]. The resultant $C_{\mathrm{t}}^{\mathrm{T}_1}(t)$ was used to assess DCE-MR related permeability parameters with the two-compartment extended Tofts model[187]. The T1-based arterial input function (AIF) was generated by averaging CA concentration time courses from 10 voxels manually selected in regions of the middle cerebral arteries (5 voxels from each side). The derived permeability metrics were further adopted to perform leakage correction for the estimations of DSC-MR metrics based on a combined biophysical and pharmacokinetic approach, in which the change of transverse relaxation rates $\Delta \mathrm{R}_2^*(t)$ ($\mathrm{R}_2^* = 1/\mathrm{T}_2^*$) can be expressed as the sum of contributions from both the intravascular and the extravascular-extracellular spaces[181]:

$$\Delta \mathrm{R}_2^*(t) = C_{\mathrm{b}}^{\mathrm{T}_2^*}(t) \otimes (r_{2,p}^* R(t) + r_{2,e}^* \mathrm{K}^{\mathrm{trans}} \cdot e^{-\frac{\mathrm{K}^{\mathrm{trans}}}{\mathrm{v_e}} t}) \tag{7.8}$$

where $C_{\mathrm{b}}^{\mathrm{T}_2^*}(t)$ represents T_2^*-based AIF, which was estimated from the same 10 voxels as generating the T_1-based AIF with a quadratic model[188], $R(t)$ represents the residue function, and $\otimes$ denotes convolution operation[189]. $r_{2,p}^*$ and $r_{2,e}^*$ refer to the transverse

relaxivities within the intravascular and extravascular-extracellular spaces, respectively. For technical demonstration, $r_{2,p}^{*}$ = 87 L·mmol^{-1}·s^{-1} and $r_{2,e}^{*}$ = 30 L·mmol^{-1}·s^{-1} were used in this work according to Schmiedeskamp et al.[179]. Leakage-insensitive perfusion metrics were then determined from the intravascular component[190].

7.2.5 Validation experiments

All imaging experiments were performed on a 3-T clinical MR scanner (MAGNETOM Vida; Siemens Healthcare, Erlangen, Germany) with a 20-channel head-neck coil. The in vivo study was approved by the local institutional review board, and all subjects provided written informed consent before participation.

Validation of T1/T2 quantification: phantom study*

The phantom study was performed on a standard 6-vial Calimetrix phantom (Calimetrix, Madison, WI). Each vial has a unique combination of T1/T2* values that can be used to validate the T1/T2* mapping accuracy of the developed MT-DICE technique. Reference T1/T2* maps were obtained with the conventional single-slice inversion-recovery spin-echo (IR-SE) and 3D multi-echo gradient-echo (ME-GRE) sequences, respectively. The detailed imaging protocols of both the reference sequences and MT-DICE are listed in Table 7.1. T1/T2* maps of the Calimetrix phantom were generated by fitting the reconstructed images voxel-by-voxel with Equation 7.6. The mean values of each vial were determined from a central slice of the MT-DICE and reference T1/T2* maps.

Table 7.1 The detailed imaging protocols of the reference methods and MT-DICE used in the phantom study are listed below

Imaging protocol	Scan parameters
Inversion-recovery spin-echo (IR-SE) 140 minutes	• FOV = 220×220 mm^2 • Spatial resolution = 1.5×1.5 mm^2 • Slice thickness = 4 mm • TR = 8000 ms • TE = 8 ms • TIs = [21, 100, 200, 400, 800, 1600] ms • Flip angle 1 = 90° • Flip angle 2 = 180°
Multi-echo gradient-echo (ME-GRE) 4 minutes	• FOV = 220×220×88 mm^3 • Spatial resolution = 1.5×1.5×4.0 mm^3 • TR = 19.30 ms • TEs = 2.46/4.92/7.38/9.84/12.30/17.22 ms • Flip angle = 10°
MT-DICE 4 minutes	• FOV = 220×220×88 mm^3 • Spatial resolution = 1.5×1.5×4.0 mm^3 • TR = 19.30 ms • TEs = 2.46/4.92/7.38/9.84/12.30/17.22 ms • SR period = temporal resolution = 1.2s • Flip angle = 10°

Validation of T1/T2 quantification: healthy control study*

Eight subjects (aged 24-67 years, 3 females) without known brain abnormalities were recruited. MT-DICE imaging was performed in an oblique transverse orientation with the following imaging parameters: FOV = 216×216×128 mm^3, spatial resolution = 1.5×1.5×4.0 mm^3, TR = 19.30 ms, TEs = 2.46/4.92/7.38/9.84/12.30/17.22 ms, SR period (the temporal resolution of dynamic T1/T2* mapping) = 1.2 s, flip angle = 10°, total time

= 7.6 min. Single dose (0.1 mmol/kg of body weight) of CA (Gadavist; Bayer Schering Pharma, Berlin, Germany) was administered through antecubital intravenous access 1.5 min into the scan at the rate of 3.0 mL/s, followed by a 20 mL saline flush at the same rate. In addition, 2D inversion-recovery TSE (IR-TSE) and 3D ME-GRE sequences were acquired before MT-DICE to serve as the pre-contrast references for T1/T2* quantification, respectively. Detailed imaging protocols for reference sequences are shown in Table 7.2. Followed by image reconstruction and dynamic T1/T2* fitting, two tissue compartments (i.e., GM and WM) were selected as regions of interests (ROIs) for T1/T2* validation on all healthy subjects.

Table 7.2 The detailed imaging protocols of the reference methods used in the healthy control study are listed below

Imaging protocol	Scan parameters
Inversion-recovery turbo spin-echo (IR-TSE) 12 minutes	• FOV = 216×216×128 mm^3 • Spatial resolution = 1.5×1.5 mm^2 • Slice thickness = 4 mm • TIs = [50, 200, 350, 500, 1000, 1500, 2400] ms • GRAPPA factor = 2
Multi-echo gradient-echo (ME-GRE) 4 minutes	• FOV = 220×220×128 mm^3 • Spatial resolution = 1.5×1.5×4.0 mm^3 • TR = 19.30 ms • TEs = 2.46/4.92/7.38/9.84/12.30/17.22 ms • Flip angle = 10°

Validation of kinetic parameter estimations: numerical simulations

Numerical simulations were performed to validate the accuracy of MT-DICE in the estimation of permeability and leakage-insensitive perfusion metrics. To better simulate

the highly heterogeneous environment within brain tumors, a 3D anthropomorphic digital reference brain phantom incorporating a tumor model from a deidentified glioblastoma patient was created[191–193]. The T1-/T2*-based AIFs were generated according to Jaspers et al.[194] and Simpson et al.[195], respectively, with realistic parameters at a 0.1-s temporal resolution. The dynamic T1/T2* curves were generated for gray matter (GM), white matter (WM) and tumor with the detailed parameters listed in Table 7.3. Subsequently, the simulated dynamic signal intensities were calculated based on Equation 7.6 using the downsampled dynamic T1/T2* curves at a temporal resolution of 1.2 s (as used in the healthy control study protocol). The generated k-space data were first undersampled and then reconstructed using the MT-DICE technique. Dynamic T1/T2* fitting and kinetic modeling were performed on all slices involving the tumor. In addition to the leakage-insensitive perfusion parameters, the perfusion metrics without leakage correction were derived in the conventional way[190].

Table 7.3 Parameters adopted in the numerical simulation study. For the numerical simulation study, the dynamic T1/T2* curves were generated for gray matter (GM), white matter (WM) and tumor with the following parameters[196–199] and the residual function was modeled as $R(t) = \exp(-\mathrm{CBF} \cdot t/\mathrm{CBV})$

	$\mathbf{v_p}$	$\mathbf{K^{trans}}$	$\mathbf{v_e}$	CBV	CBF	T10	T2*0
GM	0.06	0	0	3.75	40	1380	60
WM	0.03	0	0	1.60	20	832	50
Tumor	0-0.1	0.03-0.6	0-0.6	0.02-12	12-240	1000	52

Validation of kinetic parameter estimations: intersession repeatability analysis

Among the 8 recruited healthy subjects, 3 of them returned within 2 weeks for a second scan with the same sequence setup as the first scan to assess intersession repeatability.

Specifically, permeability and perfusion metrics were generated on the repeated data from these 3 healthy volunteers. Twelve ROIs were manually drawn on the frontal, parietal and occipital regions of the GM and WM of both left and right hemispheres from a slice located at the level of the mid brain. ROIs of the 2 separate scans were drawn at the same locations.

7.2.6 Patient pilot study

Four patients (aged 14-60 years, 1 female) with known brain tumors were recruited, including 2 patients with glioblastoma (World Health Organization [WHO] grade IV), 1 patient with ependymoblastoma (WHO grade IV), and 1 patient with meningioma (WHO grade II). The MT-DICE sequence was incorporated in a clinical MR study and was acquired during a single dose contrast injection without any preload bolus, using the same protocol as mentioned above. The clinical protocol included pre- and post-contrast T1 (MPRAGE), pre-contrast T2-FLAIR, pre-contrast T2 (TSE) and DWI (RESOLVE).

In each brain cancer patient, the tumor region was identified on the post-contrast T1 images. Dynamic T1/T2* fitting and kinetic modeling were performed on three continuous slices covering the tumor region. Both leakage-insensitive perfusion metrics and those without leakage correction were derived[190].

7.2.7 Statistical analysis

All statistical analyses were performed in SPSS version 24 (IBM Corp., Armonk, NY). A *P* value < 0.05 was considered to indicate statistical significance.

Validation of T1/T2 quantification*

For the phantom study, linear regression analysis, ICCs, Bland-Altman analysis and paired t-tests were used to assess the T1/T2* measurement agreement and difference for each vial between MT-DICE and corresponding reference methods. For the healthy control study, the agreements and differences between MT-DICE and corresponding references in pre-contrast T1/T2* measurement of the GM and WM were evaluated by ICCs and paired t-tests, respectively.

Validation of kinetic parameter estimations

For the numerical simulation study, the mean, standard deviation and range of each permeability and leakage-insensitive perfusion parameters for GM, WM and the tumor region were derived, respectively. In addition, mean percentage differences between the derived values and the corresponding ground-truth were also calculated. The intersession repeatability of MT-DICE-based $\mathrm{v_p}$, $\mathrm{K^{trans}}$, CBV and CBF quantification was evaluated for GM and WM ROIs separately with the Bland-Altman analysis and ICCs.

7.3 RESULTS

The MT-DICE imaging was performed successfully on all subjects. All image reconstructions were performed off-line on a Linux workstation with a 2.70 GHz dual 12-core Intel Xeon processor equipped with 256 GB RAM and running MATLAB. The reconstruction took about 1.0 h while the post-processing (including dynamic T1/T2* fitting and parameter estimation) took about 40 min for each slice.

7.3.1 Validation of T1/T2* quantification

Phantom study

Figure 7.3A displays the T1/T2* maps of the Calimetrix phantom generated by MT-DICE and reference sequences, respectively. There were no significant differences in the T1/T2* values between the two methods (*P* = 0.247/0.202). Excellent agreements in the T1/T2* values were observed with R^2 = 0.999/0.998, and ICC = 0.997/0.998 (Figure 7.3B). Figure 7.3C shows the Bland-Altman plots for T1/T2* quantification between MT-DICE and corresponding references. The mean differences were less than 2.5% with limits of agreement all within ±12%.

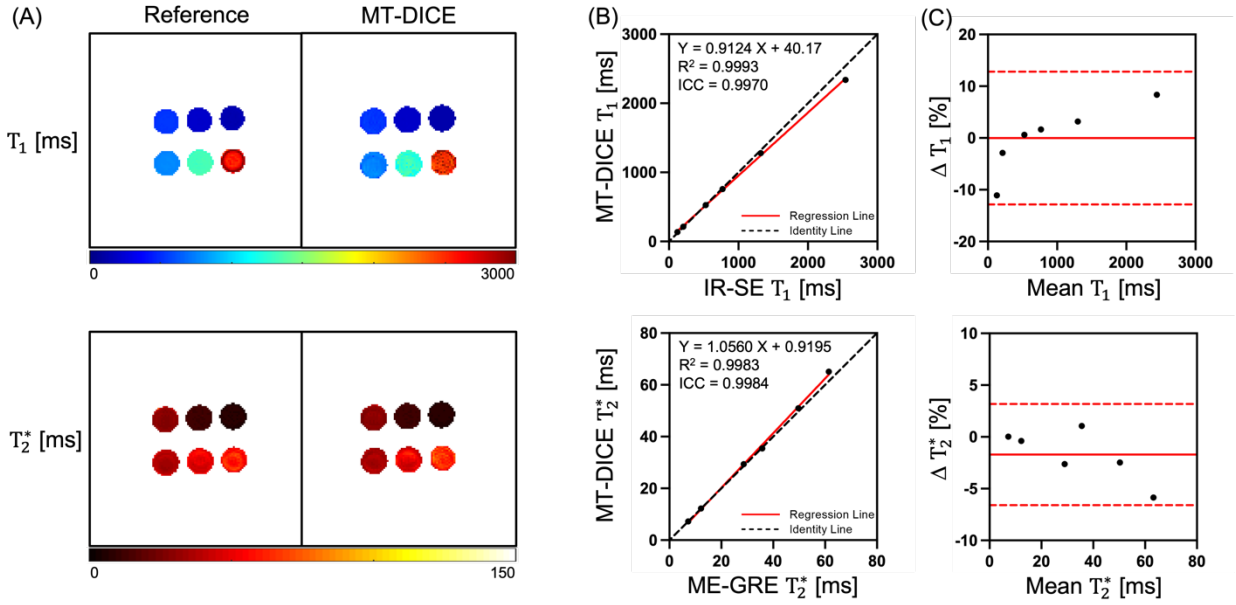

Figure 7.3 Phantom study results. A, T1/T2* maps of the quantitative 6-vial Calimetrix phantom generated by MT-DICE and reference sequences (2D inversion-recovery spin-echo for T1 and 3D multi-echo gradient-echo for T2* measurements). B, Linear regression analyses and intraclass correlation coefficients (ICC) of the T1/T2* measurements between MT-DICE and references. The black dashed lines represent identity lines (Y=X), whereas the red solid lines represent regression lines. The T1/T2* measurements from MT-DICE are in substantial quantitative agreement with reference measurements, as demonstrated by the high R^2 and ICC (R^2 = 0.999/0.998, and ICC = 0.999/0.998 for T1/T2*)

Healthy control study

With the proposed MT-DICE protocol, there were 380 contrast phases within the entire 7.6-min scan, each of which contains 60 SR times and 6 echo times. Reconstructed brain images at 3 representative contrast phases (pre-contrast phase t = 20 s, first-pass phase at t = 110 s, and post-contrast phase at t = 420 s) corresponding to 2 SR times (τ = 600 ms and τ = 1200 ms) and 2 echo times (t_E = 2.46 ms and t_E = 17.22 ms) are displayed in Figure 7.4.

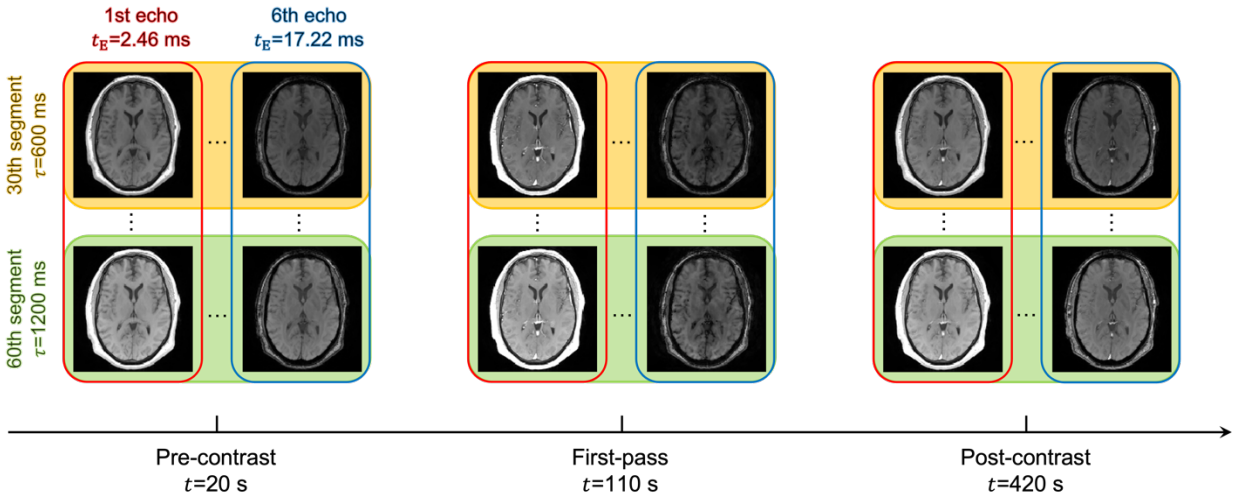

Figure 7.4 Illustration of multiple time dimensions for MT-DICE and representative images from a healthy control study. Multidimensional images are reconstructed from the low-rank tensor framework in the saturation recovery time dimension τ, echo time dimension t_E, and contrast phase dimension t. Example brain images at 3 representative contrast phases (pre-contrast phase with t = 0 s, first-pass phase with t = 20 s, and post-contrast phase with t = 360 s) corresponding to 2 SR times (τ = 600 ms and τ = 1200 ms) and 2 echo times (t_E = 2.46 ms and t_E = 17.22 ms) are displayed

Figure 7.5 demonstrates the process of conversion from signal intensity curves to T1- and T2*-based contrast concentration curves using MT-DICE. Figure 7.5A displays the representative signal intensity curves over all time dimensions (SR time, echo time and contrast dynamics dimensions) generated by averaging the curves of all voxels within a 3-by-3 ROI for blood, GM and WM, respectively. Figure 7.5B and 7.5C show the

corresponding dynamic T1/T2* curves, and Figure 7.5D and 7.5E display the T1- and T2*-based CA concentration curves for each of these three tissues.

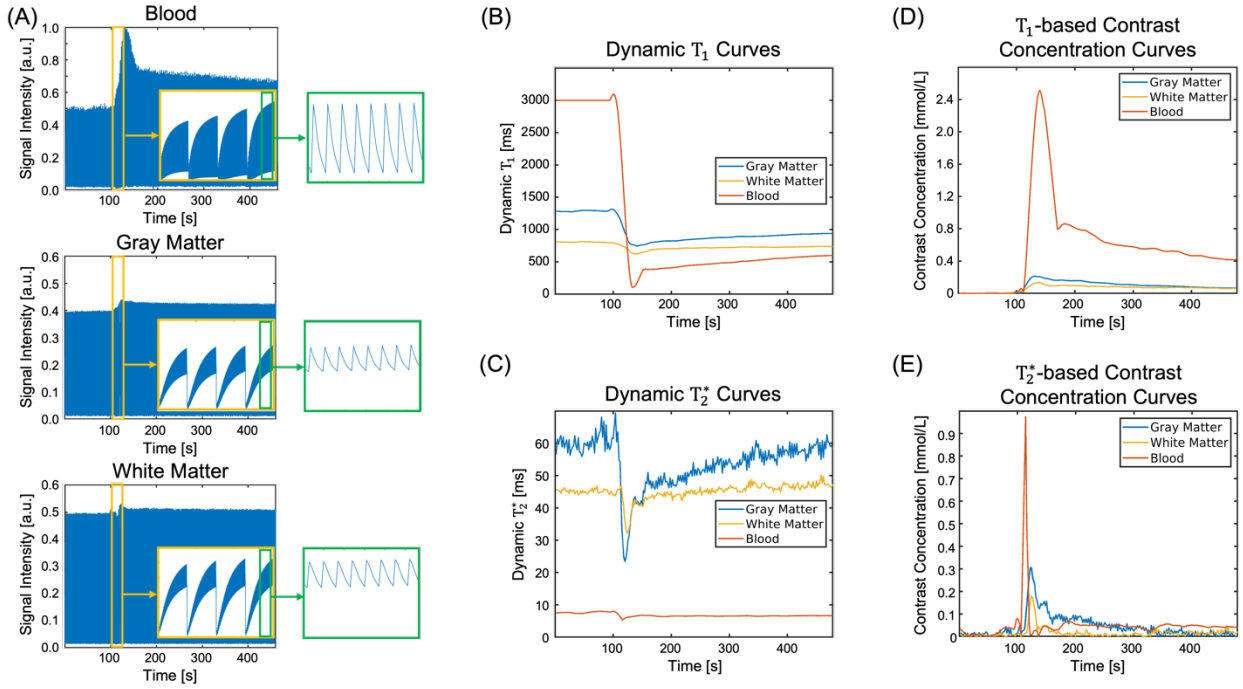

Figure 7.5 Conversion from signal intensity curves to T1-/T2*-based contrast concentration curves in MT-DICE. A, Representative dynamic signal intensity curves for blood, gray matter and white matter. The yellow zoomed-in areas show the saturation recovery curves and the green zoomed-in areas show the multi-echo decay curves. B, C, Dynamic T1/T2*curves. D, E, T1-/T2*-based CA concentration curves derived directly from the dynamic T1/T2* values

Pre-contrast T1/T2* maps of 2 representative slices generated by MT-DICE and corresponding reference sequences are displayed for a healthy subject in Figure 7.6. The parametric maps acquired by MT-DICE were of high image quality and comparable with reference maps, with well-preserved brain tissue structures and contrasts. In quantitative comparisons between MT-DICE and the reference methods (Table 7.4), all the ICCs of T1/T2* measurements in GM/WM were within the “excellent” definition range (ICC = 0.860/0.925 and 0.962/0.975 for GM and WM respectively). The *P* values of paired t-tests

were 0.219/0.769 and 0.221/0.315 for GM and WM respectively, indicating insignificant differences between the T1/T2* values quantified by MT-DICE and the references.

Table 7.4 Comparison of pre-contrast T1/T2* measurements of the gray/white matter between MT-DICE and corresponding references

		MT-DICE [ms]	Reference [ms]	ICC, 95% CI	Paired t-test (*P* value)
Pre-con T1	GM	1301.4 ± 21.7	1291.2 ± 19.9	0.860, [0.681,0.971]	0.219
	WM	781.6 ± 31.6	788.0 ± 36.6	0.962, [0.823,0.992]	0.221
Pre-con T2*	GM	56.1 ± 1.5	56.0 ± 1.4	0.925, [0.620,0.985]	0.769
	WM	39.3 ± 2.4	40.5 ± 2.2	0.975, [0.941,0.997]	0.315

Note: T1/T2* are presented as mean ± standard deviation

Abbreviations: ICC, intraclass correlation coefficients; CI, confidence interval; Pre-con, pre-contrast; GM, gray matter; WM, white matter

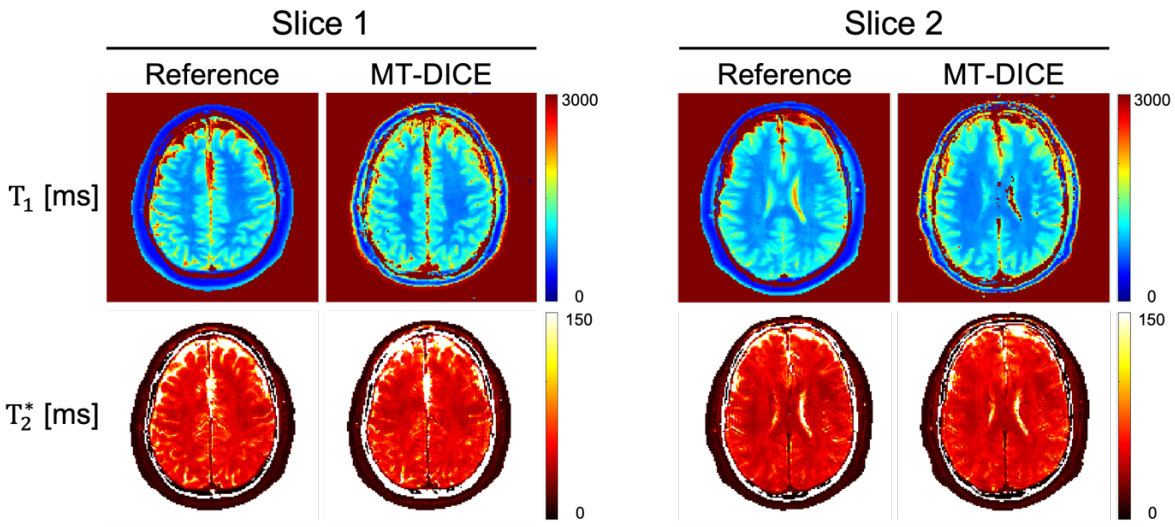

Figure 7.6 Example pre-contrast T1/T2* generated by MT-DICE and corresponding references on a healthy subject

7.3.2 Validation of kinetic parameter estimations

Numerical simulations

The simulated dynamic image series at τ = 1200 ms and t_E = 2.46 ms of one representative slice from the digital brain phantom, and the ground-truth and MT-DICE derived maps of DCE- and DSC-MR parameters as well as their error maps are shown in Figure 7.7. MT-DICE was capable to mitigate contrast leakage effects, which is more evident in CBV quantification, thus leading to smaller mean percentage errors compared to the without leakage correction counterpart (14.39% vs. 18.87%).

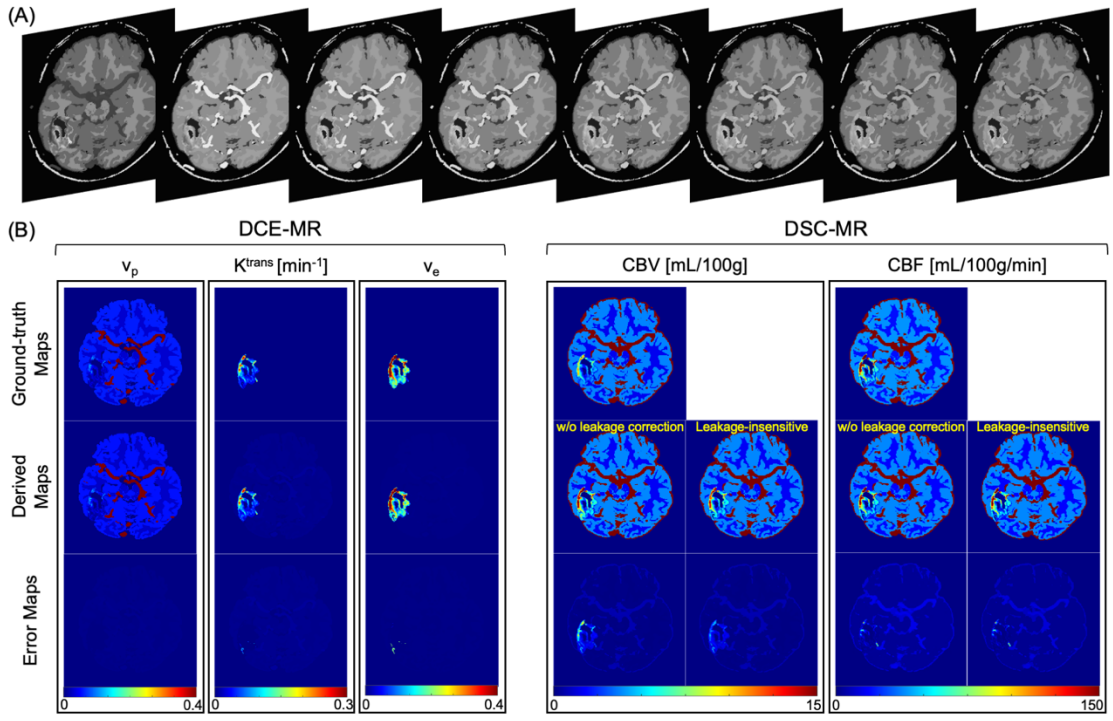

Figure 7.7 A, Simulated dynamic image series at τ = 1200 ms and t_E = 2.46 ms of one representative slice from the constructed digital reference brain phantom. Different phases of dynamic contrast enhancement are clearly visualized from the image series. B, The ground-truth maps and derived maps of vascular permeability (i.e., v_p, K^{trans}, and v_e) and perfusion (i.e., CBV and CBF) parameters together with their absolute difference maps. The derived leakage-corrected perfusion metrics were displayed and compared with their non-leakage-corrected counterparts to validate the capability of MT-DICE to estimate leakage-insensitive perfusion parameters

Table 7.5 summarizes the quantitative results measured from GM, WM and the entire tumor model except the necrotic core with the proposed leakage correction

algorithm. Different from GM and WM, which were assigned identical kinetic parameters for all voxels during simulation, respectively, the mean, standard deviation and range of each kinetic parameter are reported for the heterogenous tumor region. The simulation results validated the accuracy of the proposed MT-DICE in kinetic parameter estimations.

Table 7.5 Ground-truth values, MT-DICE derived values, and corresponding percentage differences of the DCE-MR permeability and leakage-corrected DSC-MR perfusion parameters

Gray matter/White matter				
		GT	**Derived**	**Mean Diff**
DCE-MR	v_p	0.0600/0.0300	0.0560/0.0276	6.67%/8.00%
	K^{trans} [min^{-1}]	0.0000/0.0000	0.0001/0.0001	-/-
	v_e	0.0000/0.0000	0.0001/0.0000	-/-
DSC-MR	CBV [mL/100g]	3.7500/1.6000	3.8470/1.6560	2.59%/3.50%
	CBF [mL/100g/min]	40.0000/20.0000	38.4300/18.6800	3.92%/6.60%
Tumor region				
		GT	**Derived**	**Mean Diff**
DCE-MR	v_p	0.0280 ± 0.0040	0.0281 ± 0.0038	0.36%
	K^{trans} [min^{-1}]	0.0780 ± 0.0460	0.0872 ± 0.0478	11.58%
	v_e	0.1685 ± 0.0726	0.1624 ± 0.0694	3.97%
DSC-MR	CBV [mL/100g]	3.3703 ± 1.9802	3.8477± 2.3769	14.39%
	CBF [mL/100g/min]	53.1957 ± 22.8970	58.6976 ± 27.7613	10.54%

Abbreviations: GT, ground-truth; Mean Diff, mean percentage difference

Intersession repeatability analysis

Good to excellent intersession repeatability of the selected permeability (i.e. v_p and K^{trans}) and perfusion metrics (i.e. CBV and CBF) in GM and WM were demonstrated with Bland-Altman plots (Figure 7.8). The ICCs of v_p, K^{trans}, CBV and CBF were 0.822, 0.694, 0.853 and 0.846 respectively in GM, and 0.884, 0.875, 0.727 and 0.750 respectively in WM.

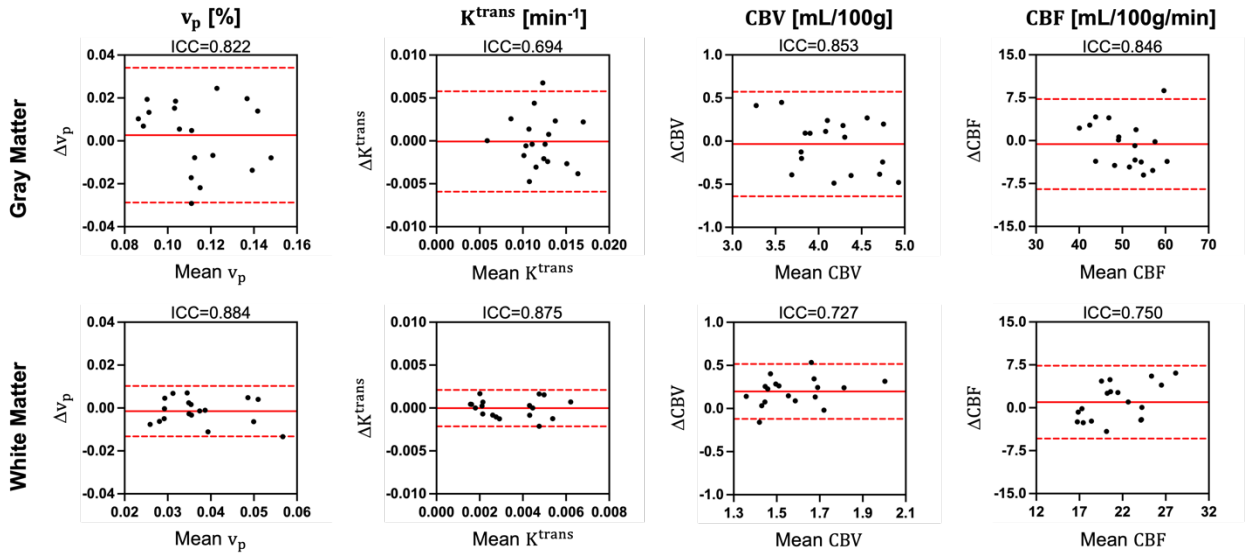

Figure 7.8 Bland-Altman analysis for intersession repeatability assessment on 3 healthy subjects who were scanned twice on separate days. Four kinetic parameters (i.e. v_p, K^{trans}, CBV, and CBF) were measured from 12 regions of interests (frontal, parietal and occipital regions of the gray matter and white matter of both left and right hemispheres from a slice located in the mid brain). Intraclass correlation coefficient (ICC) of each parameter is shown on top of the corresponding Bland-Altman plot

7.3.3 Patient pilot study

Figure 7.9 shows the images acquired by MT-DICE and clinical protocols from two representative patients. The patient displayed in Figure 7.9A is a 14-year-old male patient diagnosed with ependymoblastoma (WHO grade IV). Intracerebral hemorrhage is presented within the tumor region and is confirmed by the clinical susceptibility-weighted images. The patient shown in Figure 7.9B is a 51-year-old male patient diagnosed with recurrent glioblastoma (WHO grade IV), who underwent radiation therapy prior to this imaging session. In both patients, the tumor regions were visualized on both the clinical images and quantitative MT-DICE maps. In addition to distinguishing the abnormalities from normal tissues, with the proposed MT-DICE technique, the heterogeneity within the tumor area was observed from the vascular permeability and leakage-insensitive

perfusion parameters. The perfusion metrics without leakage correction showed that CBV is slightly overestimated, likely due to the T2* leakage effect.

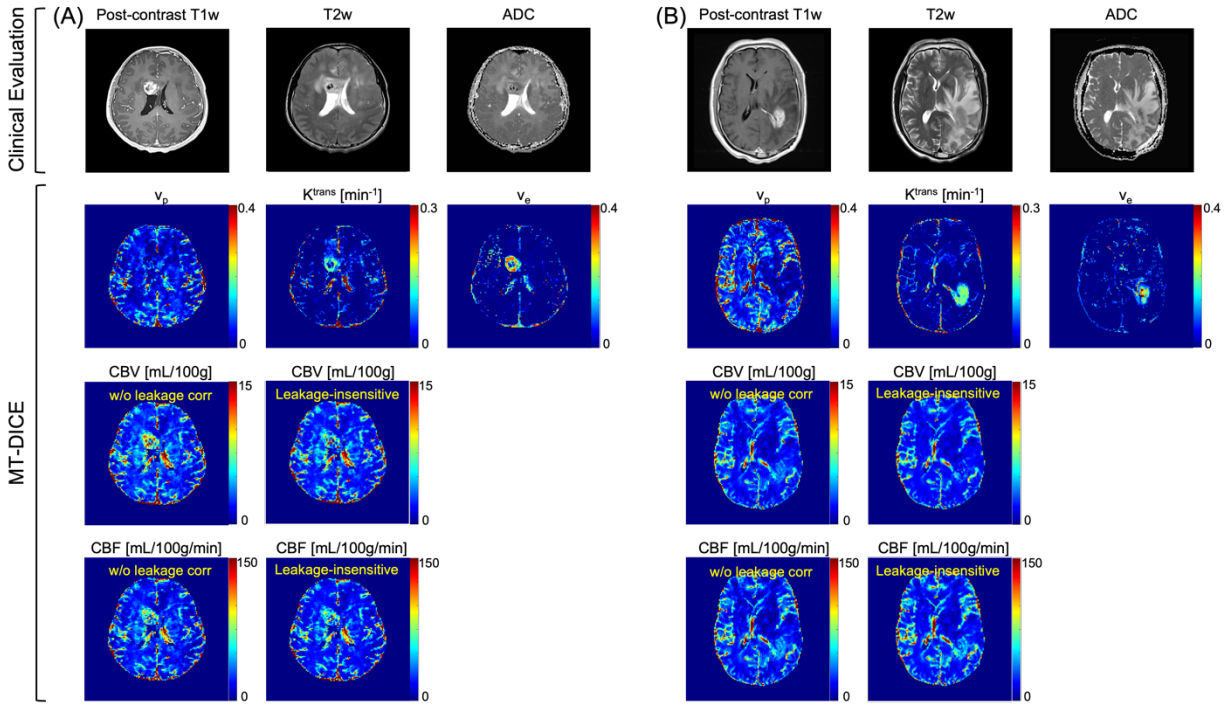

Figure 7.9 Representative images of A, a 60-year-old female patient with ependymoblastoma (World Health Organization grade IV) and B, a 51-year-old male patient with recurrent glioblastoma (World Health Organization grade IV). With MT-DICE, in addition to distinguishing the tumor abnormalities from normal tissues, the heterogeneity within the tumor region could be observed from the vascular permeability maps (v_p, K^{trans}, and v_e) and leakage-corrected perfusion metrics (CBV and CBF). The non-leakage-corrected perfusion parameters are also displayed as comparison

7.4 DISCUSSION

In this work, we developed an MT-DICE technique for simultaneous DCE- and DSC-MR quantification with a single-dose injection. With a single 7.6-min scan, the technique provides 3D whole-brain coverage, high temporal resolution of 1.2 s without

compromising spatial resolution, dynamic T1/T2* mapping, and permeability and leakage-insensitive perfusion maps with reduced EPI-associated image distortions. Hence, a more comprehensive evaluation of cerebrovascular conditions can be achieved with this technique.

Compared with existing multi-echo-based combined DCE-MR and DSC-MR techniques, the proposed method has several advantages. First, MT-DICE can achieve as high as 1.2 s temporal resolution without the compromise in the spatial resolution or coverage. For both DCE-MR and DSC-MR methods, a sufficient temporal resolution is critical for accurate quantification of kinetic parameters. The general consensus is that a temporal resolution equals to or less than 1.5 s is required for DSC-MR because of the need for adequately capturing the fast passage of CA through tissues[200]. For DCE-MR, the requirement for the temporal resolution is typically less stringent than DSC-MR and is recommended to be less than 5.3 s for brain tumor assessment[201]. However, Li et al. reported that a temporal resolution on the order of 1 s is required to accurately measure AIF, which tends to change more rapidly compared with normal brain tissues[202]. To achieve a sufficiently high temporal resolution, the spatial resolution or coverage may be sacrificed due to the trade-off between spatial and temporal resolutions. An insufficient spatial resolution will lead to partial volume effects, particularly in the AIF, and can affect the reliability of the estimated parameters[203]. In this work, MT-DICE can achieve a high temporal resolution and a high spatial resolution simultaneously, thanks to the MR multitasking framework which adopts an LRT image model for expedited acquisitions[55].

Second, MT-DICE quantifies the CA concentration from dynamic T1/T2* values rather than from T1-/T2*-weighted signal intensities. In most of the existing DCE-MR and

DSC-MR techniques, contrast concentration is derived directly by linear transformation of the dynamic signal intensities. The linearity assumption is valid only when CA concentration is low within the tissue of interests and may introduce quantification errors in tissues with high CA uptake[135,183]. It has been demonstrated that the mapping-based approach provides more accurate estimations compared to the conventional linear approach[184]. The pre-contrast T1/T2* fitting accuracy was validated in both phantom and healthy control studies. For healthy control study, MT-DICE yielded consistent GM and WM T1/T2* measurements with excellent agreement with the corresponding references. Post-contrast mapping results were not assessed in this work since the contrast washout may lead to different T1/T2* values at different time points. Furthermore, the dynamic T1 mapping of MT-DICE not only provides excellent T1 sensitivity, but also eliminates the necessity of acquiring a separate pre-contrast T1 map, which is required in conventional DCE-MR methods to convert signal intensities into concentration curves[204]. This may potentially improve the accuracy of parameter estimations since it gets rid of the interscan subject motion and eliminates the impact of spatial variations in B1 when utilizing variable flip angles for pre-contrast T1 mapping[205,206].

Third, MT-DICE employs a 3D Cartesian acquisition with segmented multi-echo FLASH readouts, which provides vascular permeability and hemodynamic perfusion maps with reduced image distortions. For existing simultaneous DCE-MR and DSC-MR techniques, single-shot EPI is the most widely used acquisition strategy. However, the major drawback to EPI-based sequences is the geometric distortions due to considerable off-resonance effects during the long readouts required to fully sample the k-space. In addition to adopting advanced EPI acquisitions to reduce the readout length and thereby

mitigate distortions, other alternative non-Cartesian readout methods may provide advantages over EPI-based readouts[172,178]. While these non-Cartesian techniques reduce the distortion artifacts induced by EPI, they may lead to other types of image artifacts that could affect the kinetic parameter estimations[178].

The developed technique is able to simultaneously measure vascular permeability metrics, such as v_p, K^{trans} and v_e, together with leakage-insensitive perfusion metrics, such as CBV and CBF. The quantification results from both control and patient groups are generally within the literature range[196,197]. In various cerebrovascular diseases, such as brain cancer and stroke, a disrupted BBB results in CA extravasation and may affect the estimated perfusion parameters. Although it has been demonstrated that multi-echo-based acquisitions can elegantly address the T1-shortening effects induced by CA extravasation[178–181,197,207,208], this type of acquisition strategy alone is insufficient for correcting the remaining T2/T2*-leakage effects. In this study, we adopted a combined biophysical and pharmacokinetic approach which utilized the derived permeability parameters to address the residual T2*-leakage effect on perfusion estimations[181]. Unlike the method presented by Schmiedeskamp et al.[179], this model avoids sophisticated and multistep parameter fitting, which could potentially improve the robustness of kinetic modeling.

Our study has several limitations. First, only gradient-echo DSC-MR parameters were available in this work. Given the fact that gradient-echo and spin-echo DSC-MR have different sensitivities on macro-and microvascular perfusion respectively, measurements of both may increase the diagnostic value, which has already been verified in practice[179,209]. In the future, another T2 time dimension could be added to the

LRT image model for dynamic T2 mapping and used to generate spin-echo DSC-MR parameters[136,185]. Second, there is no comparison between the permeability and perfusion parameters generated by MT-DICE and those acquired using conventional DCE-MR and DSC-MR, respectively. However, it is not easy to validate both DCE-MR and DSC-MR metrics simultaneously since this requires multiple contrast injections on a single subject. As an alternative, a numerical simulation study was performed in this work to validate the accuracy of MT-DICE in deriving kinetic parameters. Yet, although a tumor model was incorporated to mimic more realistic scenarios, one major limitation of the numerical simulation study is that the susceptibility effects cannot be appropriately modeled without considering field perturbations within heterogenous tumor structures, which may result in some biases for DSC-MR quantification. In the future, studies with careful designs are warranted to directly compare MT-DICE with conventional DCE-MR and DSC-MR. Last, feasibility of the proposed technique requires further validation on a large patient cohort. More patient cases are required to further validate the capability of MT-DICE in simultaneous permeability and perfusion assessment, and in the meantime, to evaluate whether this technique has better clinical performance in diagnosis, tumor grading, surgical guidance and treatment monitoring compared to conventional methods.

7.5 CONCLUSION

The developed MT-DICE technique facilitates simultaneous permeability and leakage-insensitive perfusion quantifications with a single-dose contrast injection. With a single 7.6-min scan, it enables 3D whole-brain coverage, high temporal resolution of 1.2 s without compromising spatial resolution, dynamic T1/T2* mapping, and provides kinetic

maps with mitigated image distortion. Our study demonstrates the technical feasibility in healthy subjects and brain tumor patients. Further studies in brain tumors are warranted to validate the clinical utility of this technique.

CHAPTER 8

Conclusions and Future Directions

Vascular imaging plays a critical role in the diagnosis, staging, and treatment monitoring of various vascular diseases. MR, due to its unique advantages, has the capability to provide not only the macroscopic morphological delineation (i.e., lumen area, vessel wall sharpness, etc.), but also the microscopic functional information (i.e., vascular permeability, hemodynamic perfusion, etc.). In recent years, with advancements in imaging and reconstruction technologies, MR vascular imaging has been included in clinical workflows for numerous diseases, such as stroke and brain cancer. For instance, MR angiography, the most widely adopted MR macroscopic vascular imaging technique, is nearly always adopted as an adjunct in stroke etiology evaluation workup to tell the lumen stenosis degree. DCE-MR and DSC-MR, on the other hand, enables non-invasive evaluation of the microscopic environment of brain cancers and have the potential to provide insights into tumor grading, surgical planning, and treatment response. However, as discussed in Chapter 1, some major technical limitations of current MR vascular imaging techniques hinder the further exploiting of it in specific applications. To tackle these technical challenges, the ultimate goal of the presented dissertation is to develop advanced MR vascular imaging techniques, including both macrovascular and microvascular imaging techniques, to better leverage the advantages of MR in diagnosis, prognosis, and treatment response assessment of various vascular diseases and improve patient outcomes. Specifically, advanced MR macrovascular imaging techniques were

developed to assist stroke etiology evaluation, while a novel MR microscopic vascular imaging technique was developed and validated on brain cancer patients to probe into the heterogenous environment within the tumor region.

8.1 SUMMARY OF THE WORK

8.1.1 MR Macroscopic Vascular Imaging for Stroke Etiology Evaluation

In this work, we developed a novel 2-station MR macroscopic vascular imaging strategy that could serve as a complement for current standard evaluation for stroke etiology. Our proposed strategy covered both the head-neck vessels as well as the heart and the great thoracic vessels to provide a more comprehensive etiology evaluation. First, a motion-compensated, data-driven accelerated MR VWI technique targeting on the head-neck vessels was proposed. In Chapter 3, we incorporated 2 modules in the conventional TSE sequence for compensation of both bulk head motion and localized movement of internal anatomies. Specifically, vNav was introduced to resolve bulk head motion and SG was introduced for localized movement. In Chapter 4, to further reduce the total acquisition time of current MR VWI, we present a deep learning-based reconstruction framework named CAMWARE that holds the potential to enable whole-brain MR VWI with 0.55-mm isotropic resolution within 4 min. Second, we proposed a comprehensive aortocardiac imaging technique that can provide multi-contrast imaging as well as cardiac phase-resolved cine imaging all within a single acquisition to examine the cardiac structures and the thoracic aorta. We started the technical development on the thoracic aorta in Chapter 5 and further extended its spatial coverage to the entire heart in Chapter 6. Some

technical modifications were made including switching the sampling trajectory from Cartesian to tiny-golden-angle radial sampling to better resolve cardiac and respiratory motion.

8.1.2 MR Microscopic Vascular Imaging for Brain Cancer Evaluation

MR microscopic vascular imaging plays a crucial role in brain cancer evaluation workflow. To obtain complementary permeability and perfusion information and reduce the overall CA dosage, in Chapter 7, a MR multitasking-based dynamic imaging for cerebrovascular evaluation (MT-DICE) technique was presented. Validated on brain tumor patients, the developed MT-DICE technique facilitates simultaneous permeability and leakage-insensitive perfusion quantifications with a single-dose contrast injection. With a single 7.6-min scan, it enables 3D whole-brain coverage, high temporal resolution of 1.2 s without compromising spatial resolution, dynamic T1/T2* mapping, and provides kinetic maps with mitigated image distortion.

8.2 FUTURE DIRECTIONS

Currently, all the techniques presented within different chapters in this dissertation are still at the early technical development stage. Although validated on certain patients, i.e., ischemic stroke patients with atherosclerosis and brain cancer patients, validation studies on a large patient cohort are warranted. For example, for the novel 2-station MR macrovascular imaging-based stroke etiology evaluation strategy, stroke patients with different subtypes will be enrolled in our study to assess the clinical values of our proposed strategy. For the MR microvascular imaging technique, which is the MT-DICE

for simultaneous permeability and leakage-insensitive evaluation, we are currently collaborating with clinicians to recruit patients with glioblastoma multiforme. The goal is to compare our developed MR-DICE technique with conventional DCE-MR and DSC-MR sequences in kinetic parameter estimations and to figure out what additional values our technique can provide to benefit brain tumor patients.

In the meantime, we are also working on further improving the clinical feasibility of the developed techniques so that they can be easily incorporated into the routine clinical workflow. For example, for those techniques based on MR multitasking framework, the relatively long reconstruction time is a major limitation for the wide clinical application. The bottleneck is to iteratively resolve spatial factor. One possible solution is to incorporate deep learning network into the reconstruction procedure so as to highly speed up the total reconstruction procedure.

REFERENCES

1. Murphy, D. J., Aghayev, A. & Steigner, M. L. Vascular CT and MRI: a practical guide to imaging protocols. *Insights into Imaging 2018 92* **9**, 215–236 (2018).
2. Nishimiya, K., Matsumoto, Y. & Shimokawa, H. Recent Advances in Vascular Imaging. *Arterioscler. Thromb. Vasc. Biol.* **40**, E313–E321 (2020).
3. Kuo, A. H., Nagpal, P., Ghoshhajra, B. B. & Hedgire, S. S. Vascular magnetic resonance angiography techniques. *Cardiovasc. Diagn. Ther.* **9**, S28 (2019).
4. Bullitt, E., Reardon, D. A. & Smith, J. K. A review of micro- and macrovascular analyses in the assessment of tumor-associated vasculature as visualized by MR. *Neuroimage* **37 Suppl 1**, (2007).
5. Beck, L. *et al.* MRI measurements of the thoracic aorta and pulmonary artery. *J. Med. Imaging Radiat. Oncol.* **62**, 64–71 (2018).
6. Krishnam, M. S. *et al.* Image quality and diagnostic accuracy of unenhanced SSFP MR angiography compared with conventional contrast-enhanced MR angiography for the assessment of thoracic aortic diseases. *Eur. Radiol.* **20**, 1311–1320 (2010).
7. Russo, V., Renzulli, M., La Palombara, C. & Fattori, R. Congenital diseases of the thoracic aorta. Role of MRI and MRA. *Eur. Radiol.* **16**, 676–684 (2006).
8. Potthast, S. *et al.* Measuring aortic diameter with different MR techniques: comparison of three-dimensional (3D) navigated steady-state free-precession (SSFP), 3D contrast-enhanced magnetic resonance angiography (CE-MRA), 2D

T2 black blood, and 2D cine SSFP. *J. Magn. Reson. Imaging* **31**, 177–184 (2010).

9. Lanzman, R. S. *et al.* Nonenhanced Free-Breathing ECG-Gated Steady-State Free Precession 3D MR Angiography of the Renal Arteries: Comparison Between 1.5 T and 3 T. *http://dx.doi.org/10.2214/AJR.09.2814* **194**, 794–798 (2012).
10. Dieleman, N. *et al.* Imaging intracranial vessel wall pathology with magnetic resonance imaging: current prospects and future directions. *Circulation* **130**, 192–201 (2014).
11. Mandell, D. M. *et al.* Intracranial Vessel Wall MRI: Principles and Expert Consensus Recommendations of the American Society of Neuroradiology. *AJNR. Am. J. Neuroradiol.* **38**, 218–229 (2017).
12. Yankeelov, T. & Gore, J. Dynamic Contrast Enhanced Magnetic Resonance Imaging in Oncology: Theory, Data Acquisition, Analysis, and Examples. *Curr. Med. Imaging Rev.* **3**, 91–107 (2009).
13. Willats, L. & Calamante, F. The 39 steps: evading error and deciphering the secrets for accurate dynamic susceptibility contrast MRI. *NMR Biomed.* **26**, 913–931 (2013).
14. Giruparajah, M. *et al.* Global survey of the diagnostic evaluation and management of cryptogenic ischemic stroke. *Int. J. Stroke* **10**, 1031–1036 (2015).
15. Thompson, G., Mills, S. J., Coope, D. J., O'Connor, J. P. B. & Jackson, A. Imaging biomarkers of angiogenesis and the microvascular environment in cerebral tumours. *Br. J. Radiol.* **84**, S127 (2011).
16. Benjamin, E. J. *et al.* Heart Disease and Stroke Statistics—2019 Update: A Report From the American Heart Association. *Circulation* **139**, e56–e528 (2019).

17. HP, A. *et al.* Classification of subtype of acute ischemic stroke. Definitions for use in a multicenter clinical trial. TOAST. Trial of Org 10172 in Acute Stroke Treatment. *Stroke* **24**, 35–41 (1993).

18. Ay, H. *et al.* A computerized algorithm for etiologic classification of ischemic stroke: The causative classification of stroke system. *Stroke* **38**, 2979–2984 (2007).

19. Arsava, E. M. *et al.* The Causative Classification of Stroke system: an international reliability and optimization study. *Neurology* **75**, 1277–1284 (2010).

20. Caplan, L. R. Intracranial branch atheromatous disease. *Neurology* **39**, 1246–1246 (1989).

21. Mair, G. & Wardlaw, J. M. Imaging of acute stroke prior to treatment: current practice and evolving techniques. *Br. J. Radiol.* **87**, (2014).

22. Saver, J. L. CLINICAL PRACTICE. Cryptogenic Stroke. *N. Engl. J. Med.* **374**, 2065–74 (2016).

23. Yaghi, S., Bernstein, R. A., Passman, R., Okin, P. M. & Furie, K. L. Cryptogenic Stroke: Research and Practice. *Circ. Res.* **120**, 527–540 (2017).

24. Song, J. W. *et al.* Vessel Wall MRI Added to MR Angiography in the Evaluation of Suspected Vasculopathies. *J. Neuroimaging* **29**, 454–457 (2019).

25. Ross, R. The pathogenesis of atherosclerosis: a perspective for the 1990s. *Nature* **362**, 801–809 (1993).

26. Mertens, L. & Friedberg, M. K. The gold standard for noninvasive imaging in congenital heart disease: echocardiography. *Curr. Opin. Cardiol.* **24**, 119–124 (2009).

27. Miller, K. D. *et al.* Brain and other central nervous system tumor statistics, 2021. *CA. Cancer J. Clin.* **71**, 381–406 (2021).

28. Ostrom, Q. T. *et al.* CBTRUS Statistical Report: Primary Brain and Other Central Nervous System Tumors Diagnosed in the United States in 2013–2017. *Neuro. Oncol.* **22**, iv1–iv96 (2020).

29. Hardee, M. E. & Zagzag, D. Mechanisms of glioma-associated neovascularization. *Am. J. Pathol.* **181**, 1126–1141 (2012).

30. Villanueva-Meyer, J. E., Mabray, M. C. & Cha, S. Current Clinical Brain Tumor Imaging. *Neurosurgery* **81**, 397–415 (2017).

31. Ellingson, B. M. *et al.* Consensus recommendations for a standardized Brain Tumor Imaging Protocol in clinical trials. *Neuro. Oncol.* **17**, 1188–1198 (2015).

32. Maia, A. C. M. *et al.* MR cerebral blood volume maps correlated with vascular endothelial growth factor expression and tumor grade in nonenhancing gliomas. *Am. J. Neuroradiol.* **26**, 777–783 (2005).

33. Law, M. *et al.* Glioma Grading: Sensitivity, Specificity, and Predictive Values of Perfusion MR Imaging and Proton MR Spectroscopic Imaging Compared with Conventional MR Imaging. *Am. J. Neuroradiol.* **24**, 1989–1998 (2003).

34. Law, M. *et al.* Comparison of cerebral blood volume and vascular permeability from dynamic susceptibility contrast-enhanced perfusion MR imaging with glioma grade. *Am. J. Neuroradiol.* **25**, 746–755 (2004).

35. Mabray, M. C., Barajas, R. F., Jr & Cha, S. Modern Brain Tumor Imaging. *Brain Tumor Res. Treat.* **3**, 8 (2015).

36. Taal, W. *et al.* Incidence of early pseudo-progression in a cohort of malignant

glioma patients treated with chemoirradiation with temozolomide. *Cancer* **113**, 405–410 (2008).

37. Sorensen, A. G. *et al.* A ‘vascular normalization index’ as potential mechanistic biomarker to predict survival after a single dose of cediranib in recurrent glioblastoma patients. *Cancer Res.* **69**, 5296–5300 (2009).
38. Abe, T. *et al.* Diagnosis of brain tumors using dynamic contrast-enhanced perfusion imaging with a short acquisition time. *Springerplus* **4**, (2015).
39. Artzi, M. *et al.* Optimization of DCE-MRI protocol for the assessment of patients with brain tumors. *Magn. Reson. Imaging* **34**, 1242 (2016).
40. Schmainda, K. M. *et al.* Multisite Concordance of DSC-MRI Analysis for Brain Tumors: Results of a National Cancer Institute Quantitative Imaging Network Collaborative Project. *AJNR. Am. J. Neuroradiol.* **39**, 1008–1016 (2018).
41. Schmainda, K. M. *et al.* Moving Toward a Consensus DSC-MRI Protocol: Validation of a Low-Flip Angle Single-Dose Option as a Reference Standard for Brain Tumors. *AJNR. Am. J. Neuroradiol.* **40**, 626–633 (2019).
42. Kim, H. S. *et al.* Which combination of MR imaging modalities is best for predicting recurrent glioblastoma? Study of diagnostic accuracy and reproducibility. *Radiology* **273**, 831–843 (2014).
43. Seeger, A. *et al.* Comparison of three different MR perfusion techniques and MR spectroscopy for multiparametric assessment in distinguishing recurrent high-grade gliomas from stable disease. *Acad. Radiol.* **20**, 1557–1565 (2013).
44. Van Cauter, S. *et al.* Combined DCE-MRI and DSC-MRI in brain lesions: a feasibility study. *Annu. Meet. ISMRM Benelux Chapter* **4**, 58 (2012).

45. Pineda, F., Sheth, D., Abe, H., Medved, M. & Karczmar, G. S. Low-dose imaging technique (LITE) MRI: initial experience in breast imaging. *Br. J. Radiol.* **92**, (2019).

46. Kanda, T., Ishii, K., Kawaguchi, H., Kitajima, K. & Takenaka, D. High signal intensity in the dentate nucleus and globus pallidus on unenhanced T1-weighted MR images: relationship with increasing cumulative dose of a gadolinium-based contrast material. *Radiology* **270**, 834–841 (2014).

47. Adin, M. E. *et al.* Hyperintense Dentate Nuclei on T1-Weighted MRI: Relation to Repeat Gadolinium Administration. *AJNR. Am. J. Neuroradiol.* **36**, 1859–1865 (2015).

48. Prince, M. R., Zhang, H. L., Roditi, G. H., Leiner, T. & Kucharczyk, W. Risk factors for NSF: a literature review. *J. Magn. Reson. Imaging* **30**, 1298–1308 (2009).

49. McDonald, R. J. *et al.* Intracranial gadolinium deposition after contrast-enhanced MR imaging. *Radiology* **275**, 772–782 (2015).

50. Melki, P. S., Jolesz, F. A. & Mulkern, R. V. Partial RF echo planar imaging with the FAISE method. I. Experimental and theoretical assessment of artifact. *Magn. Reson. Med.* **26**, 328–341 (1992).

51. Constable, R. T. & Gore, J. C. The loss of small objects in variable TE imaging: implications for FSE, RARE, and EPI. *Magn. Reson. Med.* **28**, 9–24 (1992).

52. Ortendahl, D. A., Kaufman, L. & Kramer, D. M. Analysis of hybrid imaging techniques. *Magn. Reson. Med.* **26**, 155–173 (1992).

53. Mugler, J. P. Optimized three-dimensional fast-spin-echo MRI. *J. Magn. Reson. Imaging* **39**, 745–767 (2014).

54. Henningsson, M. *et al.* Black-Blood Contrast in Cardiovascular MRI. *J. Magn. Reson. Imaging* **55**, 61–80 (2022).

55. Christodoulou, A. G. *et al.* Magnetic resonance multitasking for motion-resolved quantitative cardiovascular imaging. *Nat. Biomed. Eng. 2018 24* **2**, 215–226 (2018).

56. Liang, Z. P. Spatiotemporal imaging with partially separable functions. *2007 4th IEEE Int. Symp. Biomed. Imaging From Nano to Macro - Proc.* 988–991 (2007) doi:10.1109/ISBI.2007.357020.

57. Lingala, S. G., Hu, Y., Dibella, E. & Jacob, M. Accelerated dynamic MRI exploiting sparsity and low-rank structure: K-t SLR. *IEEE Trans. Med. Imaging* **30**, 1042–1054 (2011).

58. Zhao, B., Haldar, J. P., Christodoulou, A. G. & Liang, Z. P. Image reconstruction from highly undersampled (k, t)-space data with joint partial separability and sparsity constraints. *IEEE Trans. Med. Imaging* **31**, 1809–1820 (2012).

59. Bhogal, P. *et al.* Intracranial vessel wall MRI. *Clin. Radiol.* **71**, 293–303 (2016).

60. Alexander, M. D. *et al.* High-resolution intracranial vessel wall imaging: imaging beyond the lumen. *J. Neurol. Neurosurg. Psychiatry* **87**, 589–597 (2016).

61. Bodle, J. D. *et al.* High Resolution MRI: An Emerging Tool for Evaluating Intracranial Arterial Disease. *Stroke.* **44**, 287 (2013).

62. Qiao, Y. *et al.* Intracranial arterial wall imaging using three-dimensional high isotropic resolution black blood MRI at 3.0 Tesla. *J. Magn. Reson. Imaging* **34**, 22–30 (2011).

63. Fan, Z. *et al.* Whole-brain intracranial vessel wall imaging at 3 Tesla using

cerebrospinal fluid-attenuated T1-weighted 3D turbo spin echo. *Magn. Reson. Med.* **77**, 1142–1150 (2017).

64. Zhang, L. *et al.* High resolution three dimensional intracranial arterial wall imaging at 3 T using T1 weighted SPACE. *Magn. Reson. Imaging* **33**, 1026–1034 (2015).

65. Fan, Z., Zuehlsdorff, S., Liu, X. & Li, D. Prospective Self-Gating for Swallowing Motion: A Feasibility Study in Carotid Artery Wall MRI Using 3D Variable-Flip-Angle TSE. *Magn. Reson. Med.* **67**, 490 (2012).

66. Wu, F. *et al.* Differential Features of Culprit Intracranial Atherosclerotic Lesions: A Whole-Brain Vessel Wall Imaging Study in Patients With Acute Ischemic Stroke. *J. Am. Heart Assoc.* **7**, (2018).

67. Zhang, N. *et al.* 3D whole-brain vessel wall cardiovascular magnetic resonance imaging: A study on the reliability in the quantification of intracranial vessel dimensions. *J. Cardiovasc. Magn. Reson.* **20**, 1–12 (2018).

68. Qiao, Y. *et al.* MR Imaging Measures of Intracranial Atherosclerosis in a Population-based Study. *Radiology* **280**, 860–868 (2016).

69. Thesen, S., Heid, O., Mueller, E. & Schad, L. R. Prospective Acquisition Correction for head motion with image-based tracking for real-time fMRI. *Magn. Reson. Med.* **44**, 457–465 (2000).

70. Godenschweger, F. *et al.* Motion correction in MRI of the brain. *Phys. Med. Biol.* **61**, R32–R56 (2016).

71. Lindenholz, A., Van Der Kolk, A. G., Zwanenburg, J. J. M. & Hendrikse, J. The use and pitfalls of intracranial vessel wall imaging: How we do it. *Radiology* **286**, 12–28 (2018).

72. Pauletto, P. *et al.* Factors Underlying the Increase in Carotid Intima-Media Thickness in Borderline Hypertensives. *Arterioscler. Thromb. Vasc. Biol.* **19**, 1231–1237 (1999).

73. Harteveld, A. A. *et al.* Data on vessel wall thickness measurements of intracranial arteries derived from human circle of Willis specimens. *Data Br.* **19**, 6 (2018).

74. Maclaren, J., Herbst, M., Speck, O. & Zaitsev, M. Prospective motion correction in brain imaging: a review. *Magn. Reson. Med.* **69**, 621–636 (2013).

75. Tisdall, M. D. *et al.* Volumetric navigators for prospective motion correction and selective reacquisition in neuroanatomical MRI. *Magn. Reson. Med.* **68**, 389–399 (2012).

76. Larson, A. C. *et al.* Self-gated cardiac cine MRI. *Magn. Reson. Med.* **51**, 93–102 (2004).

77. Yang, Q. *et al.* Whole-brain vessel wall MRI: A parameter tune-up solution to improve the scan efficiency of three-dimensional variable flip-angle turbo spin-echo. *J. Magn. Reson. Imaging* **46**, 751–757 (2017).

78. McCarthy, R. M. *et al.* Coronary MR angiography: True FISP imaging improved by prolonging breath holds with preoxygenation in healthy volunteers. *Radiology* **227**, 283–288 (2003).

79. Andrews-Shigaki, B. C., Armstrong, B. S. R., Zaitsev, M. & Ernst, T. Prospective motion correction for magnetic resonance spectroscopy using single camera retro-grate reflector optical tracking. *J. Magn. Reson. Imaging* **33**, 498–504 (2011).

80. Forman, C., Aksoy, M., Hornegger, J. & Bammer, R. Self-encoded marker for

optical prospective head motion correction in MRI. *Med. Image Anal.* **15**, 708–719 (2011).

81. Liu, C., Bammer, R., Kim, D. H. & Moseley, M. E. Self-navigated interleaved spiral (SNAILS): application to high-resolution diffusion tensor imaging. *Magn. Reson. Med.* **52**, 1388–1396 (2004).

82. Van Der Kouwe, A. J. W., Benner, T. & Dale, A. M. Real-time rigid body motion correction and shimming using cloverleaf navigators. *Magn. Reson. Med.* **56**, 1019–1032 (2006).

83. White, N. *et al.* PROMO – Real-time Prospective Motion Correction in MRI using Image-based Tracking. *Magn. Reson. Med.* **63**, 91 (2010).

84. Dyverfeldt, P., Deshpande, V. S., Kober, T., Krueger, G. & Saloner, D. Reduction of motion artifacts in carotid MRI using free-induction decay navigators. *J. Magn. Reson. Imaging* **40**, 214–220 (2014).

85. Mattay, R. R. *et al.* Current Clinical Applications of Intracranial Vessel Wall MR Imaging. *Semin. Ultrasound. CT. MR* **42**, 463–473 (2021).

86. Song, J. W. *et al.* MR Intracranial Vessel Wall Imaging: A Systematic Review. *J. Neuroimaging* **30**, 428–442 (2020).

87. Leao, D. J., Agarwal, A., Mohan, S. & Bathla, G. Intracranial vessel wall imaging: applications, interpretation, and pitfalls. *Clin. Radiol.* **75**, 730–739 (2020).

88. Zhu, C. *et al.* Accelerated whole brain intracranial vessel wall imaging using black blood fast spin echo with compressed sensing (CS-SPACE). *MAGMA* **31**, 457–467 (2018).

89. Jia, S. *et al.* Joint intracranial and carotid vessel wall imaging in 5 minutes using

compressed sensing accelerated DANTE-SPACE. *Eur. Radiol.* **30**, 119–127 (2020).

90. Pruessmann, K. P., Weiger, M., Scheidegger, M. B. & Boesiger, P. SENSE: Sensitivity encoding for fast MRI. *Magn. Reson. Med.* **42**, 952–962 (1999).

91. Sodickson, D. K. & Manning, W. J. Simultaneous acquisition of spatial harmonics (SMASH): fast imaging with radiofrequency coil arrays. *Magn. Reson. Med.* **38**, 591–603 (1997).

92. Griswold, M. A. *et al.* Generalized autocalibrating partially parallel acquisitions (GRAPPA). *Magn. Reson. Med.* **47**, 1202–1210 (2002).

93. Lustig, M., Donoho, D. & Pauly, J. M. Sparse MRI: The application of compressed sensing for rapid MR imaging. *Magn. Reson. Med.* **58**, 1182–1195 (2007).

94. Wang, S. *et al.* Accelerating magnetic resonance imaging via deep learning. *Proc. - Int. Symp. Biomed. Imaging* **2016-June**, 514–517 (2016).

95. Hammernik, K. *et al.* Learning a variational network for reconstruction of accelerated MRI data. *Magn. Reson. Med.* **79**, 3055–3071 (2018).

96. Yang, Y., Sun, J., Li, H. & Xu, Z. ADMM-Net: A Deep Learning Approach for Compressive Sensing MRI. (2017) doi:10.48550/arxiv.1705.06869.

97. Liu, F., Samsonov, A., Chen, L., Kijowski, R. & Feng, L. SANTIS: Sampling-Augmented Neural neTwork with Incoherent Structure for MR image reconstruction. *Magn. Reson. Med.* **82**, 1890–1904 (2019).

98. Schlemper, J., Caballero, J., Hajnal, J. V., Price, A. N. & Rueckert, D. A Deep Cascade of Convolutional Neural Networks for Dynamic MR Image Reconstruction. *IEEE Trans. Med. Imaging* **37**, 491–503 (2018).

99. Knoll, F. *et al.* Deep-Learning Methods for Parallel Magnetic Resonance Imaging Reconstruction: A Survey of the Current Approaches, Trends, and Issues. *IEEE Signal Process. Mag.* **37**, 128–140 (2020).

100. Wang, S. *et al.* DeepcomplexMRI: Exploiting deep residual network for fast parallel MR imaging with complex convolution. *Magn. Reson. Imaging* **68**, 136–147 (2020).

101. Eun, D. in *et al.* Deep-learning-based image quality enhancement of compressed sensing magnetic resonance imaging of vessel wall: comparison of self-supervised and unsupervised approaches. *Sci. Reports 2020 101* **10**, 1–17 (2020).

102. Zhou, Z. *et al.* Neural network enhanced 3D turbo spin echo for MR intracranial vessel wall imaging. *Magn. Reson. Imaging* **78**, 7–17 (2021).

103. Quan, T. M., Nguyen-Duc, T. & Jeong, W. K. Compressed Sensing MRI Reconstruction Using a Generative Adversarial Network With a Cyclic Loss. *IEEE Trans. Med. Imaging* **37**, 1488–1497 (2018).

104. Ronneberger, O., Fischer, P. & Brox, T. U-Net: Convolutional Networks for Biomedical Image Segmentation. *Lect. Notes Comput. Sci. (including Subser. Lect. Notes Artif. Intell. Lect. Notes Bioinformatics)* **9351**, 234–241 (2015).

105. Liu, P., Zhang, H., Lian, W. & Zuo, W. Multi-Level Wavelet Convolutional Neural Networks. *IEEE Access* **7**, 74973–74985 (2019).

106. Lin, G., Milan, A., Shen, C. & Reid, I. RefineNet: Multi-path Refinement Networks for High-Resolution Semantic Segmentation. *2017 IEEE Conf. Comput. Vis. Pattern Recognit.* **2017-January**, 5168–5177 (2017).

107. He, K., Zhang, X., Ren, S. & Sun, J. Delving deep into rectifiers: Surpassing human-level performance on imagenet classification. in *Proceedings of the IEEE International Conference on Computer Vision* vol. 2015 Inter 1026–1034 (2015).

108. Kingma, D. P. & Ba, J. L. Adam: A Method for Stochastic Optimization. *3rd Int. Conf. Learn. Represent. ICLR 2015 - Conf. Track Proc.* (2014) doi:10.48550/arxiv.1412.6980.

109. Abadi, M. *et al.* TensorFlow: Large-Scale Machine Learning on Heterogeneous Distributed Systems. (2016) doi:10.48550/arxiv.1603.04467.

110. Javed, Z., Shahzad, H. & Omer, H. Modified POCS Based Reconstruction for Compressed Sensing in MRI. *Proc. - 2015 13th Int. Conf. Front. Inf. Technol. FIT 2015* 291–296 (2016) doi:10.1109/FIT.2015.58.

111. Hu, Z. *et al.* Motion-compensated 3D turbo spin-echo for more robust MR intracranial vessel wall imaging. *Magn. Reson. Med.* **86**, 637–647 (2021).

112. Uecker, M. *et al.* ESPIRiT--an eigenvalue approach to autocalibrating parallel MRI: where SENSE meets GRAPPA. *Magn. Reson. Med.* **71**, 990–1001 (2014).

113. François, C. J. & Carr, J. C. MRI of the Thoracic Aorta. *Magn. Reson. Imaging Clin. N. Am.* **15**, 639–651 (2007).

114. Stanger, O. H., Pepper, J. R. & Svensson, L. G. Surgical management of aortic pathology: Current fundamentals for the clinical management of aortic disease. *Surg. Manag. Aortic Pathol. Curr. Fundam. Clin. Manag. Aortic Dis.* 1–1223 (2019) doi:10.1007/978-3-7091-4874-7.

115. Mendel, T., Popow, J., Hier, D. B. & Czlonkowska, A. Advanced atherosclerosis of the aortic arch is uncommon in ischemic stroke: an autopsy study. *Neurol. Res.*

24, 491–494 (2002).

116. Loebe, M. *et al.* Acute and chronic thoracic aortic disease: surgical considerations. *HSR Proc. Intensive Care Cardiovasc. Anesth.* **4**, 243 (2012).
117. Dudzinski, D. M. & Isselbacher, E. M. Diagnosis and Management of Thoracic Aortic Disease. *Curr. Cardiol. Rep.* **17**, (2015).
118. Katz, E. S. *et al.* Visualization and identification of the left common carotid and left subclavian arteries: a transesophageal echocardiographic approach. *J. Am. Soc. Echocardiogr.* **9**, 58–61 (1996).
119. Hiratzka, L. F. *et al.* 2010 ACCF/AHA/AATS/ACR/ASA/SCA/SCAI/SIR/STS/SVM Guidelines for the Diagnosis and Management of Patients With Thoracic Aortic Disease. *Circulation* **121**, (2010).
120. Baliyan, V., Verdini, D. & Meyersohn, N. M. Noninvasive aortic imaging. *Cardiovasc. Diagn. Ther.* **8**, S3–S18 (2018).
121. Zhou, C. *et al.* Characterization of atherosclerotic disease in thoracic aorta: A 3D, multicontrast vessel wall imaging study. *Eur. J. Radiol.* **85**, 2030–2035 (2016).
122. Kallianos, K. G. & Burris, N. S. Imaging Thoracic Aortic Aneurysm. *Radiol. Clin. North Am.* **58**, 721 (2020).
123. Roes, S. D. *et al.* Aortic vessel wall magnetic resonance imaging at 3.0 Tesla: a reproducibility study of respiratory navigator gated free-breathing 3D black blood magnetic resonance imaging. *Magn. Reson. Med.* **61**, 35–44 (2009).
124. Mihai, G., Chung, Y. C., Merchant, A., Simonetti, O. P. & Rajagopalan, S. T1-weighted-SPACE dark blood whole body magnetic resonance angiography (DB-WBMRA): initial experience. *J. Magn. Reson. Imaging* **31**, 502–509 (2010).

125. Wehrum, T., Dragonu, I., Strecker, C., Hennig, J. & Harloff, A. Multi-contrast and three-dimensional assessment of the aortic wall using 3T MRI. *Eur. J. Radiol.* **91**, 148–154 (2017).

126. Tobey, D. J. *et al.* In Vivo Assessment of Ascending and Arch Aortic Compliance. *Ann. Vasc. Surg.* **57**, 22–28 (2019).

127. Lalande, A. *et al.* Compliance and pulse wave velocity assessed by MRI detect early aortic impairment in young patients with mutation of the smooth muscle myosin heavy chain. *J. Magn. Reson. Imaging* **28**, 1180–1187 (2008).

128. Shaw, J. L. *et al.* Free-breathing, non-ECG, continuous myocardial T 1 mapping with cardiovascular magnetic resonance multitasking. *Magn. Reson. Med.* **81**, 2450–2463 (2019).

129. Kolda, T. G. & Bader, B. W. Tensor decompositions and applications. *SIAM Review* vol. 51 455–500 (2009).

130. Christodoulou, A. G. *et al.* Fast dynamic electron paramagnetic resonance (EPR) oxygen imaging using low-rank tensors. *J. Magn. Reson.* **270**, 176–182 (2016).

131. He, J. *et al.* Accelerated High-Dimensional MR Imaging With Sparse Sampling Using Low-Rank Tensors. *IEEE Trans. Med. Imaging* **35**, 2119–2129 (2016).

132. Trzasko, J. D. & Manduca, A. A Unified Tensor Regression Framework for Calibrationless Dynamic , Multi-Channel MRI Reconstruction. *Ismrm* **21**, 4371 (2013).

133. Bustin, A. *et al.* High-dimensionality undersampled patch-based reconstruction (HD-PROST) for accelerated multi-contrast MRI. *Magn. Reson. Med.* **81**, 3705–3719 (2019).

134. Yaman, B., Weingärtner, S., Kargas, N., Sidiropoulos, N. D. & Akçakaya, M. Low-Rank Tensor Models for Improved Multi-Dimensional MRI: Application to Dynamic Cardiac T1 Mapping. *IEEE Trans. Comput. imaging* **6**, 194 (2019).

135. Wang, N. *et al.* Quantitative 3D dynamic contrast-enhanced (DCE) MR imaging of carotid vessel wall by fast T1 mapping using Multitasking. *Magn. Reson. Med.* **81**, 2302–2314 (2019).

136. Ma, S. *et al.* Three-dimensional simultaneous brain T1, T2, and ADC mapping with MR Multitasking. *Magn. Reson. Med.* **84**, 72–88 (2020).

137. Liu, C. Y., Bley, T. A., Wieben, O., Brittain, J. H. & Reeder, S. B. Flow-independent T(2)-prepared inversion recovery black-blood MR imaging. *J. Magn. Reson. Imaging* **31**, 248–254 (2010).

138. Xie, J. *et al.* 3D flow-independent peripheral vessel wall imaging using T(2)-prepared phase-sensitive inversion-recovery steady-state free precession. *J. Magn. Reson. Imaging* **32**, 399–408 (2010).

139. Amano, Y., Takahama, K. & Kumita, S. Non-contrast-enhanced MR angiography of the thoracic aorta using cardiac and navigator-gated magnetization-prepared three-dimensional steady-state free precession. *J. Magn. Reson. Imaging* **27**, 504–509 (2008).

140. Koktzoglou, I. Gray blood magnetic resonance for carotid wall imaging and visualization of deep-seated and superficial vascular calcifications. *Magn. Reson. Med.* **70**, 75–85 (2013).

141. Miura, T. *et al.* Plaque Vulnerability in Internal Carotid Arteries with Positive Remodeling. *Cerebrovasc. Dis. Extra* **1**, 54 (2011).

142. Harloff, A. *et al.* 3D MRI provides improved visualization and detection of aortic arch plaques compared to transesophageal echocardiography. *J. Magn. Reson. Imaging* **36**, 604–611 (2012).

143. Fan, Z. *et al.* Multi-contrast atherosclerosis characterization (MATCH) of carotid plaque with a single 5-min scan: technical development and clinical feasibility. *J. Cardiovasc. Magn. Reson.* **16**, (2014).

144. Redheuil, A. *et al.* Proximal aortic distensibility is an independent predictor of all-cause mortality and incident CV events: the MESA study. *J. Am. Coll. Cardiol.* **64**, 2619–2629 (2014).

145. Chen, Y. *et al.* Efficient and accurate MRI super-resolution using a generative adversarial network and 3D multi-level densely connected network. in *Lecture Notes in Computer Science (including subseries Lecture Notes in Artificial Intelligence and Lecture Notes in Bioinformatics)* vol. 11070 LNCS 91–99 (Springer Verlag, 2018).

146. Mc Namara, K., Alzubaidi, H. & Jackson, J. K. Cardiovascular disease as a leading cause of death: how are pharmacists getting involved? *Integr. Pharm. Res. Pract.* **8**, 1–11 (2019).

147. Menchón-Lara, R. M., Simmross-Wattenberg, F., Casaseca-de-la-Higuera, P., Martín-Fernández, M. & Alberola-López, C. Reconstruction techniques for cardiac cine MRI. *Insights Imaging* **10**, 1–16 (2019).

148. Sakuma, H., Takeda, K. & Higgins, C. B. Fast magnetic resonance imaging of the heart. *Eur. J. Radiol.* **29**, 101–113 (1999).

149. Milotta, G. *et al.* Simultaneous 3D whole-heart bright-blood and black blood

imaging for cardiovascular anatomy and wall assessment with interleaved T 2 prep-IR. *Magn. Reson. Med.* **82**, 312–325 (2019).

150. Alizadehasl, A. & Fase, M. D. F. *Practical Cardiology, E-Book: Principles and Approaches*. (2021).

151. Kellman, P., Hernando, D. & Arai, A. E. Myocardial Fat Imaging. *Curr. Cardiovasc. Imaging Rep.* **3**, 83–91 (2010).

152. Eggers, H., Brendel, B., Duijndam, A. & Herigault, G. Dual-echo Dixon imaging with flexible choice of echo times. *Magn. Reson. Med.* **65**, 96–107 (2011).

153. Pfeiffer, M. P. & Biederman, R. W. W. Cardiac MRI: A General Overview with Emphasis on Current Use and Indications. *Med. Clin. North Am.* **99**, 849–861 (2015).

154. Feng, L. *et al.* 5D whole-heart sparse MRI. *Magn. Reson. Med.* **79**, 826–838 (2018).

155. Hu, Z. *et al.* Magnetic resonance multitasking for multidimensional assessment of cardiovascular system: Development and feasibility study on the thoracic aorta. *Magn. Reson. Med.* **84**, 2376–2388 (2020).

156. Takahashi, K. *et al.* Relation Between Left Atrial Wall Thickness in Patients with Atrial Fibrillation and Intracardiac Electrogram Characteristics and ATP-Provoked Dormant Pulmonary Vein Conduction. *J. Cardiovasc. Electrophysiol.* **26**, 597–605 (2015).

157. Bishop, M. *et al.* Three-dimensional atrial wall thickness maps to inform catheter ablation procedures for atrial fibrillation. *Europace* **18**, 376–383 (2016).

158. Ho, S. Y. & Nihoyannopoulos, P. Anatomy, echocardiography, and normal right

ventricular dimensions. *Heart* **92**, i2 (2006).

159. Kosaraju, A., Goyal, A., Grigorova, Y. & Makaryus, A. N. Left Ventricular Ejection Fraction. *StatPearls* (2021).

160. Shah, S., Chryssos, E. D. & Parker, H. Magnetic Resonance Imaging: A Wealth of Cardiovascular Information. *Ochsner J.* **9**, 266 (2009).

161. Xu, J. *et al.* Towards a five-minute comprehensive cardiac MR examination using highly accelerated parallel imaging with a 32-element coil array: feasibility and initial comparative evaluation. *J. Magn. Reson. Imaging* **38**, 180–188 (2013).

162. Han, F. *et al.* Self-gated 4D multiphase, steady-state imaging with contrast enhancement (MUSIC) using rotating cartesian K-space (ROCK): Validation in children with congenital heart disease. *Magn. Reson. Med.* **78**, 472–483 (2017).

163. Ginami, G. *et al.* Non-contrast enhanced simultaneous 3D whole-heart bright-blood pulmonary veins visualization and black-blood quantification of atrial wall thickness. *Magn. Reson. Med.* **81**, 1066–1079 (2019).

164. Ginami, G. *et al.* Simultaneous bright- and black-blood whole-heart MRI for noncontrast enhanced coronary lumen and thrombus visualization. *Magn. Reson. Med.* **79**, 1460–1472 (2018).

165. Foley, T. A. *et al.* Measuring left ventricular ejection fraction-techniques and potential pitfalls. *Eur. Cardiol.* **8**, 108–114 (2012).

166. Dixon, W. T. Simple proton spectroscopic imaging. *Radiology* **153**, 189–194 (1984).

167. Ma, J. Dixon techniques for water and fat imaging. *J. Magn. Reson. Imaging* **28**, 543–558 (2008).

168. Henningsson, M. *et al.* Quantification of epicardial fat using 3D cine Dixon MRI. *BMC Med. Imaging* **20**, 1–9 (2020).

169. Coombs, B. D., Szumowski, J. & Coshow, W. Two-point Dixon technique for water-fat signal decomposition with B0 inhomogeneity correction. *Magn. Reson. Med.* **38**, 884–889 (1997).

170. Wang, Y., Li, D., Haacke, E. M. & Brown, J. J. A three-point Dixon method for water and fat separation using 2D and 3D gradient-echo techniques. *J. Magn. Reson. Imaging* **8**, 703–710 (1998).

171. Shiroishi, M. S. *et al.* Principles of T2 *-weighted dynamic susceptibility contrast MRI technique in brain tumor imaging. *J. Magn. Reson. Imaging* **41**, 296–313 (2015).

172. Quarles, C. C., Bell, L. C. & Stokes, A. M. Imaging vascular and hemodynamic features of the brain using dynamic susceptibility contrast and dynamic contrast enhanced MRI. *Neuroimage* **187**, 32–55 (2019).

173. Boxerman, J. L., Schmainda, K. M. & Weisskoff, R. M. Relative Cerebral Blood Volume Maps Corrected for Contrast Agent Extravasation Significantly Correlate with Glioma Tumor Grade, Whereas Uncorrected Maps Do Not. *AJNR Am. J. Neuroradiol.* **27**, 859 (2006).

174. Bjornerud, A., Sorensen, A. G., Mouridsen, K. & Emblem, K. E. T1- and T2*-dominant extravasation correction in DSC-MRI: part I--theoretical considerations and implications for assessment of tumor hemodynamic properties. *J. Cereb. Blood Flow Metab.* **31**, 2041–2053 (2011).

175. Kim, E. J. *et al.* Simultaneous acquisition of perfusion and permeability from

corrected relaxation rates with dynamic susceptibility contrast dual gradient echo. *Magn. Reson. Imaging* **22**, 307–314 (2004).

176. Newbould, R. D. *et al.* Perfusion mapping with multiecho multishot parallel imaging EPI. *Magn. Reson. Med.* **58**, 70–81 (2007).

177. Zaitsev, M. *et al.* Dual-contrast echo planar imaging with keyhole: application to dynamic contrast-enhanced perfusion studies. *Phys. Med. Biol.* **50**, 4491–4505 (2005).

178. Paulson, E. S., Prah, D. E. & Schmainda, K. M. Spiral Perfusion Imaging With Consecutive Echoes (SPICE^{TM}) for the Simultaneous Mapping of DSC- and DCE-MRI Parameters in Brain Tumor Patients: Theory and Initial Feasibility. *Tomogr. (Ann Arbor, Mich.)* **2**, 295–307 (2016).

179. Schmiedeskamp, H. *et al.* Simultaneous perfusion and permeability measurements using combined spin- and gradient-echo MRI. *J. Cereb. Blood Flow Metab.* **33**, 732–743 (2013).

180. Wu, J., Saindane, A. M., Zhong, X. & Qiu, D. Simultaneous perfusion and permeability assessments using multiband multi-echo EPI (M2-EPI) in brain tumors. *Magn. Reson. Med.* **81**, 1755–1768 (2019).

181. Stokes, A. M., Semmineh, N. & Quarles, C. C. Validation of a T1 and T2* leakage correction method based on multiecho dynamic susceptibility contrast MRI using MION as a reference standard. *Magn. Reson. Med.* **76**, 613–625 (2016).

182. Knutsson, L., Ståhlberg, F. & Wirestam, R. Aspects on the accuracy of cerebral perfusion parameters obtained by dynamic susceptibility contrast MRI: a simulation study. *Magn. Reson. Imaging* **22**, 789–798 (2004).

183. Calcagno, C., Mani, V., Ramachandran, S. & Fayad, Z. A. Dynamic contrast enhanced (DCE) magnetic resonance imaging (MRI) of atherosclerotic plaque angiogenesis. *Angiogenesis* **13**, 87–99 (2010).

184. Wang, N. *et al.* Six-dimensional quantitative DCE MR Multitasking of the entire abdomen: Method and application to pancreatic ductal adenocarcinoma. *Magn. Reson. Med.* **84**, 928–948 (2020).

185. Ma, S. *et al.* Three-dimensional whole-brain simultaneous T1, T2, and T1ρ quantification using MR Multitasking: Method and initial clinical experience in tissue characterization of multiple sclerosis. *Magn. Reson. Med.* **85**, 1938–1952 (2021).

186. Pintaske, J. *et al.* Relaxivity of Gadopentetate Dimeglumine (Magnevist), Gadobutrol (Gadovist), and Gadobenate Dimeglumine (MultiHance) in human blood plasma at 0.2, 1.5, and 3 Tesla. *Invest. Radiol.* **41**, 213–221 (2006).

187. Tofts, P. S. *et al.* Estimating Kinetic Parameters From Dynamic Contrast-Enhanced T 1-Weighted MRI of a Diffusable Tracer: Standardized Quantities and Symbols. *J. Magn. Reson. Imaging* **10**, 223–232 (1999).

188. Kjølby, B. F., Østergaard, L. & Kiselev, V. G. Theoretical model of intravascular paramagnetic tracers effect on tissue relaxation. *Magn. Reson. Med.* **56**, 187–197 (2006).

189. Wu, O. *et al.* Tracer arrival timing-insensitive technique for estimating flow in MR perfusion-weighted imaging using singular value decomposition with a block-circulant deconvolution matrix. *Magn. Reson. Med.* **50**, 164–174 (2003).

190. Straka, M., Albers, G. W. & Bammer, R. Real-time diffusion-perfusion mismatch

analysis in acute stroke. *J. Magn. Reson. Imaging* **32**, 1024–1037 (2010).

191. Bosca, R. J. & Jackson, E. F. Creating an anthropomorphic digital MR phantom--an extensible tool for comparing and evaluating quantitative imaging algorithms. *Phys. Med. Biol.* **61**, 974–982 (2016).
192. Cocosco, C. A. *et al.* BrainWeb: Online Interface to a 3D MRI Simulated Brain Database. *Neuroimage* **5**, 425 (1997).
193. Collins, D. L. *et al.* Design and construction of a realistic digital brain phantom. *IEEE Trans. Med. Imaging* **17**, 463–468 (1998).
194. Jaspers, K. *et al.* Reliability of pharmacokinetic parameters: small vs. medium-sized contrast agents. *Magn. Reson. Med.* **62**, 779–787 (2009).
195. Simpson, N. E. & Evelhoch, J. L. Deuterium NMR tissue perfusion measurements using the tracer uptake approach: II. Comparison with microspheres in tumors. *Magn. Reson. Med.* **42**, 240–247 (1999).
196. Zhang, N. *et al.* Correlation of Volume Transfer Coefficient Ktrans with Histopathologic Grades of Gliomas. *J. Magn. Reson. Imaging* **36**, 355 (2012).
197. Bjørnerud, A. & Emblem, K. E. A fully automated method for quantitative cerebral hemodynamic analysis using DSC-MRI. *J. Cereb. Blood Flow Metab.* **30**, 1066–1078 (2010).
198. Wansapura, J. P., Holland, S. K., Dunn, R. S. & Ball, W. S. NMR relaxation times in the human brain at 3.0 Tesla. *J. Magn. Reson. Imaging* **9**, 531–538 (1999).
199. Peters, A. M. *et al.* T2* measurements in human brain at 1.5, 3 and 7 T. *Magn. Reson. Imaging* **25**, 748–753 (2007).
200. Welker, K. *et al.* ASFNR recommendations for clinical performance of MR

dynamic susceptibility contrast perfusion imaging of the brain. *AJNR. Am. J. Neuroradiol.* **36**, E41–E51 (2015).

201. Heye, A. K., Culling, R. D., Valdés Hernández, M. D. C., Thrippleton, M. J. & Wardlaw, J. M. Assessment of blood-brain barrier disruption using dynamic contrast-enhanced MRI. A systematic review. *NeuroImage. Clin.* **6**, 262–274 (2014).
202. Li, K. L. *et al.* An improved coverage and spatial resolution--using dual injection dynamic contrast-enhanced (ICE-DICE) MRI: a novel dynamic contrast-enhanced technique for cerebral tumors. *Magn. Reson. Med.* **68**, 452–462 (2012).
203. Chen, J. J., Smith, M. R. & Frayne, R. The impact of partial-volume effects in dynamic susceptibility contrast magnetic resonance perfusion imaging. *J. Magn. Reson. Imaging* **22**, 390–399 (2005).
204. Landis, C. S. *et al.* Determination of the MRI Contrast Agent Concentration Time Course In Vivo Following Bolus Injection: Effect of Equilibrium Transcytolemmal Water Exchange. *Magn Reson Med* **44**, 563–574 (2000).
205. Sung, K., Daniel, B. L. & Hargreaves, B. A. Transmit B1+ field inhomogeneity and T1 estimation errors in breast DCE-MRI at 3 tesla. *J. Magn. Reson. Imaging* **38**, 454–459 (2013).
206. Sung, K., Saranathan, M., Daniel, B. L. & Hargreaves, B. A. Simultaneous T(1) and B(1) (+) mapping using reference region variable flip angle imaging. *Magn. Reson. Med.* **70**, 954–961 (2013).
207. Quarles, C. C., Gore, J. C., Xu, L. & Yankeelov, T. E. Comparison of dual-echo DSC-MRI- and DCE-MRI-derived contrast agent kinetic parameters. *Magn.*

Reson. Imaging **30**, 944–953 (2012).

208. Uematsu, H. & Maeda, M. Double-echo perfusion-weighted MR imaging: basic concepts and application in brain tumors for the assessment of tumor blood volume and vascular permeability. *Eur. Radiol.* **16**, 180–186 (2006).

209. Speck, O., Chang, L., Menaka Desilva, N. & Ernst, T. Perfusion MRI of the Human Brain With Dynamic Susceptibility Contrast: Gradient-Echo Versus Spin-Echo Techniques. *J. Magn. Reson. Imaging* **12**, 381–387 (2000).